



Stockholm University
Department of Astronomy

LICENTIATE THESIS

Gravitational lensing and radio interferometry as a probe of the small-scale structure of dark matter

Author:
Saghar Asadi

*Department of Astronomy,
Oscar Klein Centre,
Stockholm University,
AlbaNova,
106 91 Stockholm,
Sweden*

Supervisor:
Erik Zackrisson

Co-Supervisors:
Emily Freeland
Garrelt Mellema

Winter 2015–16

List of acronyms

ALMA Atacama Large Millimeter/sub-millimeter Array

BBN Big Bang Nucleosynthesis

BL BaseLine, the projected distance between each antenna pair in an interferometry network

CASA Common Astronomy Software Applications ¹

CDM Cold Dark Matter

CMB Cosmic Microwave Background

DM Dark Matter

dSph dwarf spheroidal galaxy

EVN European VLBI Network

GL Gravitational lensing

gNFW generalized NFW

HDM Hot Dark Matter

IMBH Intermediate-Mass Black Hole

MACHO Massive Compact Halo Object

MW Milky Way

NFW Navarro-Frenk-White, the Universal density profiles of simulated CDM halos, first introduced by Navarro, Frenk, & White (1996)

SDSS Sloan Digital Sky Survey

¹The software can be downloaded from <http://casa.nrao.edu/>

PSF Point Spread Function

SMG Sub–Millimeter Galaxy

THINGS The HI Nearby Galaxy Survey

TBTF Too–Big–To–Fail

UCMH UltraCompact MiniHalo

VLBI Very Long Baseline Interferometry

VPoS Vas Plane Of Satellites

WDM Warm Dark Matter

WIMP Weakly–Interacting Massive Particle

WMAP Wilkinson Microwave Anisotropy Probe

2dFGRS 2–degree–Field Galaxy Redshift Survey

Abstract

Gravitational lensing has been widely used in astronomy for about a century. The fact that gravity treats dark and luminous mass the same way gives GL a unique advantage over many other observational methods, to provide an independent test for the presence of dark structures of various size and mass. Strong lensing by a foreground object can produce multiple images, known as *macroimage*, of a background light source. Measurements of strong lens systems provide information about the mass distribution of the lens as well as the structure of emission from the source. On the other hand, the concordance model of cosmology has yet to describe the observed Universe at all scales simultaneously. One way to probe the small-scale structures of dark matter is to study a particular type of lens system where the foreground galaxy produces multiple images of the background light source, and the substructure within the foreground dark matter halo that surrounds the galaxy presents itself as surface brightness perturbations in one of the macroimages.

Detecting small-scale surface brightness perturbations requires high-resolution imaging of lensed extended sources. Radio interferometry is a technique that connects an array of radio antennae to essentially work as a single dish with the diameter as large as the maximum distance within the array. Arrays such as VLBI networks or ALMA, or combinations of these, make it possible to probe radio quasars and sub-mm galaxies with sub-milliarcsecond angular resolutions.

In this thesis, we simulate observations of multiply-lensed sources (radio quasars and dusty star-forming galaxies) at $z \simeq 2$ with different (present and near-future) radio interferometers. These simulations are then used to explore the extent to which various forms of halo substructures can be constrained. In **Paper I**, we derive the minimum mass that subhalos with different internal density profiles need to have in order to produce detectable lensing effects on multiply-imaged quasars using three different radio arrays. Using the derived minimum detectable mass of different forms of subhalos, we estimate constraints that observations of a number of such lens systems can place on the contribution of each form of substructure in the mass of the parent halo. **Paper II** focuses on simulations of SMGs using ALMA and the prospects for detecting standard CDM subhalos. In this paper, we show that standard CDM subhalos in the sub-galactic mass range are detectable using high-frequency observations with ALMA. In addition to probing the mass of the substructure, such observations are able to discern the difference between the standard CDM subhalos and other dark compact objects. This can place constraints on the contribution of CDM subhalos to the mass of their host halo – a quantity directly comparable to cosmological simulations.

List of papers and my contribution

Included in this thesis

- I Zackrisson, E., **Asadi, S.**, Wiik, K., Jönsson, J., Scott, P., Datta, K.K., Friedrich, M.M., Jensen, H., Johansson, J., Rydberg, C-E., Sandberg, A. (2013) “Hunting for dark halo substructure using submilliarcsecond-scale observations of macrolensed radio jets” Monthly Notices of the Royal Astronomical Society 431, 2172-2183 (**Paper II**)
I ran all simulations and generated all figures in this paper and contributed to the text.
- II **Asadi, S.**, Zackrisson, E., Freeland, E., “Probing cold dark matter subhalos with simulated ALMA observations of macrolensed submm galaxies” submitted (**Paper II**)
All the simulations and modelings in the paper are done by me. I also wrote the text.

Other papers

- III Zackrisson, E., Calissendorff, P., **Asadi, S.**, Nyholm, A. (2015) “Extragalactic SETI: The Tully-Fisher Relation as a Probe of Dysonian Astroengineering in Disk Galaxies” The Astrophysical Journal 810, 23
- IV Zackrisson, E., González, J., Eriksson, S., **Asadi, S.**, Safraneck-Shrader, C., Trenti, M., Inoue, A. K. (2015) “Primordial star clusters at extreme magnification” Monthly Notices of the Royal Astronomical Society 449, 3057-3063
- V Rydberg, C.-E., Zackrisson, E., Zitrin, A., Guaita, L., Melinder, J., **Asadi, S.**, González, J., Östlin, G., Ström, T (2015) “A Search for Population III Galaxies in CLASH. I. Singly-imaged Candidates at High Redshift” The Astrophysical Journal 804, 13
- VI Tilanus, R. P. J., and 167 colleagues (2014) “Future mmVLBI Research with ALMA: A European vision” ArXiv e-prints arXiv:1406.4650

Contents

1	Dark matter	1
1.1	Why do we need dark matter?	1
1.1.1	CMB temperature fluctuations	2
1.1.2	Gravitational lensing	2
1.1.3	Masses of galaxy clusters	2
1.1.4	Galactic rotation curves	3
1.2	What do we know about dark matter?	3
2	The standard model of cosmology – strengths and challenges	7
2.1	Model parameters	7
2.2	Challenges of the model, or what is bugging us!	8
2.2.1	Abundance matching, or the missing–satellite problem	9
2.2.2	Central slope, or the core–cusp problem	9
2.2.3	Normalization, or the too–big–to–fail problem	12
2.2.4	Spatial distribution, or the plane of satellites problem	13
3	Gravitational Lensing	15
3.1	Mathematical Description	16
3.2	Strong Lensing	19
3.2.1	Astrometric Perturbation	20
3.2.2	Time Delay	21
3.2.3	Flux Ratio Anomalies	21
4	Radio interferometry	23
4.1	Radio telescopes	23
4.2	Observational limitations	24
4.3	Two-element interferometer	25
4.4	Aperture synthesis	26
5	Summary	31

Dark matter

Dark matter, the second dominant component of our Universe, is thought to be made of non-baryonic, cold (i.e. non-relativistic), weakly interacting massive particles (WIMPs) – for a review of dark matter candidates see e.g. Bergström (2013); Del Popolo (2014). Some of these characteristics are inferred from cosmological evidence. For instance, observations of small-scale cosmic structure indicate that dark matter must be non-relativistic. The measured abundance of light elements in the Universe, along with Big Bang Nucleosynthesis (BBN) result in dark matter being non-baryonic (see e.g. Gelmini (2015) , for a more detailed discussion). Even though the problem of the “missing mass” in the Universe has been approached from the particle physics point of view in addition to the cosmological one, it is still considered as one of the biggest challenges of both!

I start this chapter by describing independent cosmological evidences for the presence of dark matter (in order of decreasing physical scale which does not necessarily correspond to historical order) and what each of them tells us about the nature and characteristics of dark matter. The chapter is finished by a review of the current state of dark matter followed by the detection methods currently used to approach the issue.

1.1 Why do we need dark matter?

The amount of baryons in the Universe can be measured with various independent methods, all of which result in a fraction less than 5% of the total content of the Universe. From the abundance of light elements in BBN, to anisotropies in the angular power spectrum of the cosmic microwave background, to the X-ray emission from galaxy clusters leading to an estimation of their baryon fractions, and the discrepancies between the dynamical and luminous mass of galaxies, the Universe seems to be full of discrepancies that are resolved by adding the missing mass in a non-baryonic form. Although, it is worth mentioning that these observations can be interpreted differently, leading to alternative theories of gravity that will not be covered in this thesis (but see e.g. Clifton 2006; Clifton et al. 2012; Bloomfield 2013).

1.1.1 CMB temperature fluctuations

Structures in the Universe are believed to have grown from small fluctuations in the primordial density field after the era of recombination. Density fluctuations are of the same order as temperature fluctuations, therefore measuring temperature fluctuations of the CMB reveals the order of magnitude of density fluctuations in the early Universe. However, taking only the baryonic matter into account, these fluctuations are too small to give rise to any structure formation in our expanding Universe. While the required amount of matter in the Universe, in units of the critical cosmological density, is $\Omega_m \equiv \rho/\rho_{\text{crit}} \sim 0.3$ the estimated upper limit for the baryonic matter density parameter Ω_b is ~ 0.025 (Planck Collaboration et al. 2015) which supports the non-baryonic nature of dark matter. Moreover, if dark matter is non-baryonic, its density fluctuations can start growing already at the radiation-dominated era while the growth of baryonic matter is damped by radiation. After the decoupling of baryons and photons, baryons collapse into the local potential minima mainly generated by the dark matter perturbations and form cosmic structures. The importance of the CMB is that it may serve as a probe to the state of the Universe at the time of the last scattering, as well as the age and conditions of the Universe ever since.

1.1.2 Gravitational lensing

The mathematical framework of gravitational lensing has been a commonly accepted framework in astronomy for a long time. However, lensing evidence for dark matter arose only after the general relativistic corrections to the Newtonian formalism of gravitational lensing. Gravitational lensing, as an accurate and reliable gravitational mass measurement of the lens, confirmed the discrepancy between the gravitational and luminous mass both on galactic and galaxy cluster scales. Gravitational lensing is now a common technique in astrophysics, and also widely used in my project. This makes it worth a chapter of its own: §3.

1.1.3 Masses of galaxy clusters

The first astronomer to notice the presence of “dark matter” was Knut Lundmark, the Swedish astronomer who was working on the relation between globular clusters and elliptical galaxies. He reports a higher gravitational mass than the luminous mass for a sample of galaxies and derives their “mass-to-light ratio” from the analysis of rotation curves (Lundmark 1930). Three years later, Zwicky noticed the order-of-magnitude difference between the dynamical mass of the Coma cluster and the mass in luminosities of individual galaxies (Zwicky 1933). The discrepancy was not recognized as an issue until after its persistence in various observations (Rubin & Ford 1970; Einasto et al. 1974; Ostriker, Peebles, & Yahil 1974). X-ray observations of hot gas in galaxy clusters confirmed that the hot gas reservoir cannot explain the missing mass. The X-ray data, additionally, provided new measurements of the velocity dispersions of galaxies in clusters, confirming the previous dynamical mass estimates. The previously unknown population of dark (or high mass-to-light ratio) matter was now accepted to dominate the mass budget of the Universe. The mean density of the matter was shown to be ~ 0.2 of

the critical density of the Universe and different models for dark matter started appearing in the literature. Firstly, the missing matter was thought to be in faint stars or hot gas but both failed to explain the situation. The first non-baryonic candidate for dark matter particles was the neutrino. However, simulations based on this model (Doroshkevich, Shandarin, & Saar 1978) indicated that neutrino-dominated dark matter cannot give rise to small scale structure in the distribution of galaxies due to the cut-off of the power spectrum of these rapidly-moving particles. This also suggested that suitable candidates for dark matter particles not only need to be dissipationless, but are also required to be much more massive than neutrinos. Therefore, the first numerical cosmological simulations based on cold dark matter CDM were performed by Melott et al. (1983) and these were able to represent the small structures of the Universe much more accurately.

1.1.4 Galactic rotation curves

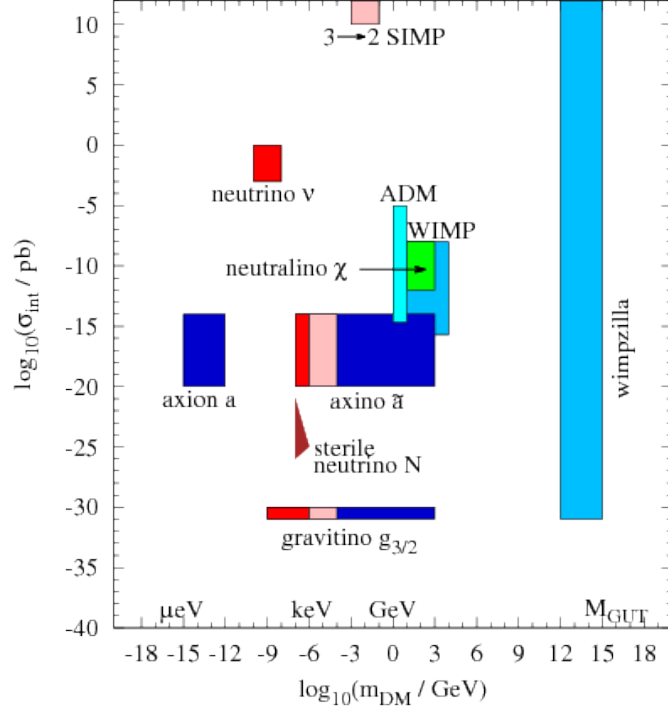
The first galaxy that showed an increasing mass profile to very large radii was M31 (Rubin & Ford 1970). By the next decade, both optical and radio data had confirmed the flat rotational curves of disk galaxies at large radii. It was the deep and high resolution HI observations that proved the flat rotation curves of a large number of galaxies beyond the optical disk, providing important evidence for the presence of massive halos around galaxies (see e.g. Bosma 1981; Begeman 1989).

1.2 What do we know about dark matter?

The commonly-accepted class of DM particles are Weakly Interacting Massive Particles (WIMPs). The main characteristics of WIMPs are listed below:

- **Massive** – While the upper limit on the mass of dark matter candidates is placed by undetection of MACHOs (Massive Astrophysical Compact Halo Objects), the lower limit is far less constrained. This limit varies depending on the properties of proposed particles. Some of the interesting DM particle candidate are shown in Figure 1.1, where the WIMP region is shown with a mass range up to ~ 1000 GeV.
- **Dissipationless and collisionless** – The existence of dark matter halos around galaxies is evidence for dark matter to be dissipationless. Being dissipationless means that dark matter cannot cool by emitting photons like baryons do. Therefore, while dark matter comes together and forms extended halos, baryonic matter falls into the gravitational well of these halos and cools down by emitting photons and then forms stars and galaxies at the halo center. Dark matter is also assumed to be collisionless, meaning that it does not interact with other dark matter particles, except via gravity. An upper limit on the cross section of dark matter comes from the famous case of the Bullet cluster (Clowe et al. 2006). The collisionless property of dark matter can alleviate two of the small-scale challenges to the CDM model that I discuss in the next chapter; the cusp-core problem 2.2.2, and the too-big-to-fail problem 2.2.3.

Figure 1.1: The mass m_{DM} vs. strength of interaction with ordinary mass σ_{int} plot showing various candidates of DM particles. The color of each region indicates the type of the corresponding DM particle; HDM in red, WDM in pink and CDM in blue (Figure from Baer et al. 2015). As an astronomer, one may prefer to read the horizontal axis in M_{\odot} rather than GeV/c^2 , so the conversion factor of $1 \text{ GeV} \simeq 8.96 \times 10^{-58} M_{\odot}$ may be helpful.



- **Cold** – the terms “cold”, “warm”, and “hot” dark matter refer to the mass of the dark matter particles which is the deciding factor in their velocity at the freeze-out epoch. This is the time when the temperature of the Universe decreased to $\sim 10^9 \text{ K}$. At this temperature, hot DM particles that are light are relativistic. Therefore small density perturbations do not survive, i.e. the early structures that form in the Universe are superclusters. Smaller structures such as galaxy cluster, galaxies and dwarf galaxies form via fragmentation, but this does not match our observations. However, if dark matter particles are as described by cold or warm DM, structure formation follows a bottom-up hierarchy where small scale structures (down to dwarf galaxies in case of WDM and even smaller fluctuations in case of CDM) survive. These small structures then merge/fall into the potential wells of larger growing structures. Cosmological simulations give a clear image of the subhalo abundance depending on the mass of DM particles (see Figure 1.2 for the difference in the power spectra for a range of DM particle masses). The generic prediction is for the abundance of subhalos to increase (α to decrease) with the DM particle mass.

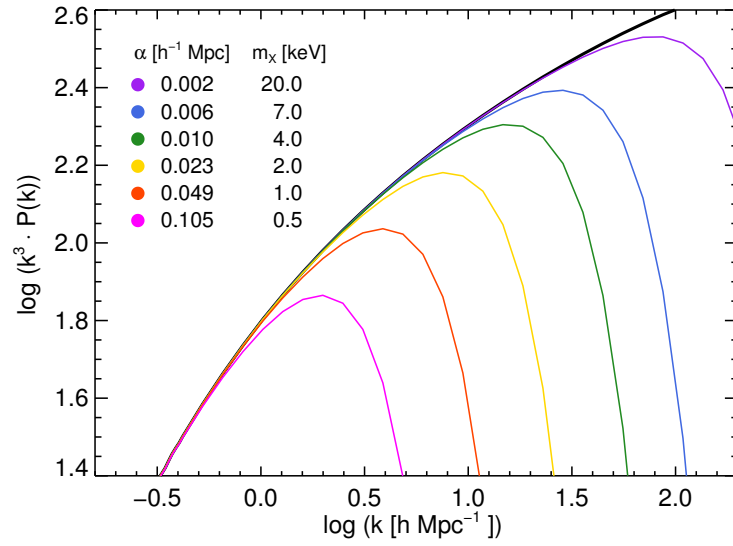


Figure 1.2: Linear power spectra of DM models with different particle masses. The thick black line corresponds to CDM and the colored lines show WDM models of various particle mass. The damping scale α is also shown for each model with the corresponding color. (Figure from Kennedy et al. 2014)

2

The standard model of cosmology – strengths and challenges

Dark matter seems to be dominating the matter content of our Universe. Our best model for dark matter particles are WIMPs whose interaction with themselves or baryons are limited to gravity. WIMPs do not cool by emitting photons as baryons do (see section 1.2). Therefore, cosmic structure formation at large scales is thought to be dominated by the behavior of dark matter. Baryonic effects, are only thought to dominate the observable Universe at scales of galaxies and below where the energy content of hydrodynamical effects such as supernovae and black hole jets are sufficient to alter their environment. The most common way to perform cosmological N-body simulations has been to simulate a pure dark matter Universe without including the complex physics of the baryonic matter. Even though this approach provides a consistent picture of our Universe on large scales, it faces systematic inconsistencies when describing scales of galaxies and below. The physics of baryonic processes such as active galactic nuclei, supernovae, and galactic and stellar wind feedback are currently active fields of research in astrophysics and there is no consensus on their implementation within cosmological simulations.

In this chapter, I first briefly introduce the current state of the standard model of cosmology, the model parameters, assumptions and initial conditions in §2.1. Then, I detail the aspects of Λ CDM model that has proven fundamentally challenging against the latest observational data (§2.2).

2.1 Model parameters

The standard model of cosmology is usually assumed to be a flat adiabatic Universe with Gaussian initial perturbations. The dynamics of these perturbations, governed by Einstein's general relativity, are dominated at large scales by an invariant dark energy (the cosmological constant). The parameter sets used to present the model can vary depending on the means of measurements and the priors. The cosmic microwave background radiation is one of the major means

Table 2.1: Table reproduced from the values presented in Planck Collaboration et al. (2015)

Parameter	Planck 68% limit value
H_0	67.8 ± 0.9
Ω_m	0.308 ± 0.012
$\Omega_b h^2$	0.0223 ± 0.0002
Δ_R^2	$2.441^{+0.088}_{-0.092} \times 10^{-9}$
n_s	0.968 ± 0.006
τ	0.066 ± 0.016

to constrain many cosmological model parameters. Assuming the flatness and curvature of the Universe that have been independently confirmed to be consistent with the data, the base model parameters in Table 2.1 are consistently constrained by studying the CMB using 9 years of WMAP (Bennett et al. 2013) and two all-sky surveys of the Planck satellite (Planck Collaboration et al. 2015). These parameters include the Hubble constant H_0 , the matter density parameter Ω_m (presented usually as the physical density $\Omega_m h^2$ where h is the Hubble parameter), the baryon density parameter Ω_b , the curvature fluctuation amplitude Δ_R^2 , the scalar spectral index of density fluctuations n_s , and the reionization optical depth τ_{re} . Planck Collaboration et al. (2015) reports the six cosmological parameter values in Table 2.1 for the base Λ CDM model. Many more familiar parameters are derived from the base model including the age of the Universe, the density parameters of different materials in the Universe (dark matter, neutrinos, radiation), the cosmic reionization redshift, and the sum of three neutrino masses. Various astrophysical observations probe one or more parameters to build and complete our picture of the Universe.

The combination of redshift and apparent magnitude of type Ia supernovae probes the expansion rate of the Universe (Riess et al. 1998; Perlmutter et al. 1999), whereas surveys such as the Two-degree-Field Galaxy Redshift Survey (2dFGRS) (Percival et al. 2002) and the Sloan Digital Sky Survey (SDSS) (Gil-Marín et al. 2015) probe the galaxy power spectrum, i.e. putting constraints on parameters such as the amplitude of dark matter density fluctuations σ_8 , their linear growth rate f , and the sum of the masses of neutrinos m_ν . Measurements of the angular power spectrum of temperature variations in the CMB provides us with the nature of initial perturbations (Bennett et al. 2013; Planck Collaboration et al. 2015). The consistency of all complementary probes and measurements point at the Λ CDM cosmological model as the best description of our present data. However, some astrophysical observations of galaxy and sub-galactic phenomena point to systematic discrepancies which need to be resolved.

2.2 Challenges of the model, or what is bugging us!

One thing that most triumphs of the Λ CDM share is the scale they are applied to. CDM model simulations match observational data at scales relevant to the CMB, the cosmic web and galaxy clusters (however, see e.g. Guo et al. 2011 who point out large-scale discrepancies in the Λ CDM model and arguing for detailed consideration of baryonic effects as the general solution to the challenges of our cosmological model at all scales). At galaxy and sub-galactic scales both model predictions and observational data are followed by large uncertainties and do not seem to give consistent results. There are different methods which astronomers use to attack the small-

scale challenges of the CDM model regarding dark matter subhalos; Dynamics in the Galaxy – disk, globular clusters, streams, satellite counts, abundance matching, $M_* - V_{\max}$ relation, and strong gravitational effects on background objects. Baryonic astrophysical processes, star formation, enrichment, feedback, and environmental effects can potentially change the status of these challenges significantly. However, currently different baryonic physics codes predict different evolutionary details for galaxies given the same initial conditions. These discrepancies indicate that we yet have to learn more about the details of baryonic processes and the ways they alter dark matter in galaxies. While structure formation at large scales is dominated by dark matter, this is not the case for small scales and this is why the CDM model fails to reproduce the observable Universe at scales $\leq 10^{12} M_{\odot}$.

2.2.1 Abundance matching, or the missing–satellite problem

The first test for small–scale CDM–based simulations is comparing the low–mass end of the predicted dark matter mass function with the faint–end of galaxy luminosity function. Connecting the dark halo mass function and dwarf galaxy luminosity function needs a linking assumption which lies at the heart of abundance–matching techniques; *galactic luminosity is a monotonic function of halo mass*. For the first time, Klypin et al. (1999); Moore et al. (1999) show that the CDM predictions already fail this test. Of course, this is an area where observations suffer from different kinds of biases. Therefore, the first potential solution to the mismatch is that the source of discrepancy is practical rather than physical. However, despite corrections based on detection thresholds and incompleteness and regardless of further detections of ultrafaint dSphs of the MW, the mismatch persists to more than an order of magnitude for the MW (See e.g. Pawlowski, McGaugh, & Jerjen 2015). Different local and universal solutions have been proposed for resolving the discrepancy. The most attractive solution is that baryonic processes and feedback effects quench star formation inside dark matter halos of the mass range $M_h \leq 10^{10} M_{\odot}$. This is a much more complicated solution to investigate and several mechanisms have been suggested to suppress star formation in low–mass CDM subhalos. However, consensus has not been reached on whether these mechanisms will cause sufficient loss of baryons in dark matter halos to be responsible for the absence of observed dwarf galaxies (See e.g. Brooks et al. (2013); Sawala et al. (2014); Del Popolo et al. (2014); Sawala et al. (2015) claiming to have found baryonic solutions to the problem, but also for opposite arguments see Bullock et al. 2010; Klypin et al. 2015).

2.2.2 Central slope, or the core–cusp problem

One of the long–standing issues of CDM halos is their density profiles (Dubinski & Carlberg 1991; Walker & Peñarrubia 2011). For over a decade, the main consensus was that the “universal” profile describing simulated dark matter halos was a two–parameter density profile, suggested by (Navarro, Frenk, & White 1996) – hereafter NFW, where the central logarithmic density slope changes as $\rho \propto 1/r$. The logarithmic slope of this profile becomes less steep with increasing r and can be described as $\rho(r) \propto r^{-3}$ around the virial radius. However, dynamical measurements of stellar and gas content in the central kpc of dwarf galaxies favor a constant–

density core for these regions (Oh et al. 2011). While further high-resolution measurements from low-surface brightness dwarf galaxies and dark matter-dominated galactic rotation curves support the cored profiles, the higher resolution CDM simulations are more consistent with a three-parameter density profile rather than the traditional NFW profile. The extra parameter describing dark halo density profiles is the shape index, α , which gives the density profile more flexibility in shape. Even with the extra parameter, these DM profiles still fail to describe observed halos which contain baryonic matter (see Figure 2.1).

On the other hand, the high-mass end of the halo mass function and luminous part of galaxy luminosity function do not indicate any discrepancies regarding the central DM slope. The reason is that there are several independent methods to derive the luminous and dark matter content of massive galaxies in their central kpcs. Resolved stellar and gas dynamical measurements probe the baryonic component, and the X-ray temperature maps combined with weak and strong gravitational lensing measurements can trace the mass in these galaxies. Therefore, it is easier to decide whether the dark matter or the stellar mass dominates the central kpc of the galaxy. However, subtracting the dynamical mass contribution from stars and deriving the dark matter-only density profile needs precise modeling of stellar populations and the mass function in the galaxy.

Halo density profiles

The central slope of the density profiles of dark matter halos can be measured both from observational data and fits to halos in N-body simulations. In this regard, the single-parameter (cored) singular isothermal sphere (ellipsoid) profile provides an acceptable lens model for the mean dark matter halo of galaxies. On the other hand, the universal density profiles of field halos in CDM simulations can be reasonably well described by the NFW profile as below

$$\rho(r) = \frac{\rho_s}{(r/r_s)(1 + r/r_s)^2} \quad (2.1)$$

where r_s is the characteristic scale radius of the halo, i.e. the radius at which $\rho \propto 1/r^2$ (isothermal), and ρ_s is the density at $r = r_s$. An extra parameter called the concentration parameter c relating the scale density of the halo to its virial radius and is defined as $c \equiv r_s/r_{\text{vir}}$. The virial radius r_{vir} , in turn is commonly defined as the r_{200} , the radius beyond which the density of the halo drops below 200 times the critical density of the Universe at the redshift at which the halo is formed. The concentration parameter therefore, contains information about the formation and evolution of the halo and depends on the time of the collapse of the halo as well as its virial mass. Given the hierarchical formation of halos, the low-mass halos were formed at higher redshifts where the mean density of the Universe was higher and so was the inner density of collapsed halos. This results in a weak $c - M_{\text{vir}}$ correlation such that the concentration parameter decreases with increasing M_{vir} . Additionally, low-mass subhalos gradually lose mass in tidal interaction with the parent halo which leads to a further increase of their c_{vir} over time (Bullock et al. 2001; Macciò, Dutton, & van den Bosch 2008).

Relaxing the central logarithmic slope $\gamma = \frac{d \ln(\rho/\rho_s)}{d \ln(r/r_s)}$ in the basic two-parameter form of NFW profile makes better fit to individual halos in CDM simulations (Stadel et al. 2009; Navarro et

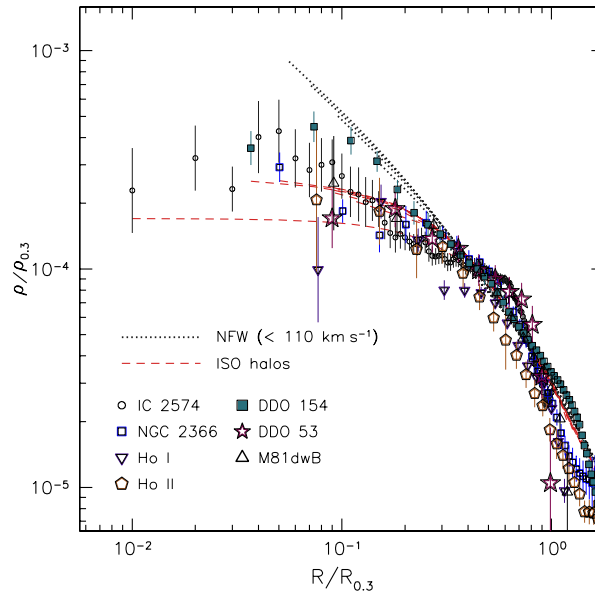


Figure 2.1: Comparison between dark matter density profiles inferred from observations of low surface brightness galaxies and theoretical density profiles. Data points show dark matter density profiles of a sample of *THINGS* dwarf galaxies derived from their neutral hydrogen rotation curves. The NFW density profiles ($\alpha \sim -1$) favored by CDM-based cosmological simulations are plotted with black dotted lines, and pseudo-isothermal halo models ($\alpha \sim 0$) with dashed red lines. While the NFW density profiles continue rising toward the center of the halo, profiles inferred from galaxies tend to form a core with a constant central density. (Figure from Oh et al. 2011)

al. 2010). In this three-parameter form, the inner cusp slope becomes progressively shallower towards the center, eventually reaching inner slope of $\gamma \geq -1$. The generalized NFW profile (gNFW) is formulated as:

$$\rho(r) = \frac{\rho_s}{(r/r_s)^\gamma (1 + r/r_s)^{3-\gamma}} \quad (2.2)$$

where $\gamma = 1$ gives the traditional NFW profile and $\gamma = 2$ is equivalent to a singular isothermal sphere (SIS). Another option for a three-parameter profile is the Einasto profile, inspired by the two-dimensional Sersic surface brightness profile of elliptical galaxies (Einasto 1965). There are various studies suggesting that simulated CDM halos are better described by a three-parameter model such as the Einasto profile than the standard NFW (e.g. Navarro et al. 2004; Gao et al. 2008; Di Cintio et al. 2014; Dutton & Macciò 2014). The extra parameter describing dark halo density profiles, α_{Ein} , gives the density profile more flexibility in shape, i.e. $\gamma(r) = -\frac{d \ln \rho}{d \ln r}$. The three-dimensional Einasto profile takes the form:

$$\ln \left(\frac{\rho(r)}{\rho_s} \right) = -b \left[\left(\frac{r}{r_s} \right)^{\frac{1}{n}} - 1 \right] \quad (2.3)$$

where the Einasto index $\alpha_{\text{Ein}} = \frac{1}{n}$, and therefore the logarithmic slope becomes $\gamma = -\frac{b}{n} \left(\frac{r}{r_s} \right)^{\frac{1}{n}}$. The best-fit density profiles to simulated dark matter halos of a variety of masses in the Aquarius project show inner slopes shallower than the original NFW (Navarro et al. 2010). These halos are not self-similar, i.e. Einasto index changes with halo mass. Navarro et al. (2004) find the Einasto index for halos in the mass range between dwarves and clusters to be 0.12–0.22, with an average value of 0.17. According to Hayashi & White (2008); Gao et al. (2008), α_{Ein} tends to increase with mass and redshift in halos of the Millennium simulation. From the gravitational lensing point of view, Einasto profiles are more demanding to work with as one cannot derive an analytical surface mass density as a function of α_{Ein} . Hence the lens equation needs to be solved numerically for each case.

2.2.3 Normalization, or the too-big-to-fail problem

A more recent issue with the predictions of the cold dark matter model was brought up only a few years ago, pointing out another discrepancy in the structural properties of DM subhalos of MW-like simulated halos and dSph satellite galaxies of the MW. While one would naively expect that the most luminous dwarf galaxies correspond to the most massive subhalos, high-resolution cosmological simulations persistently produce massive subhalos ($M_{\text{sub}} \geq 10^{10} M_\odot$) which are too concentrated in their central kpc to host any of the satellite galaxies around the Milky Way or Andromeda (Boylan-Kolchin, Bullock, & Kaplinghat (2011, 2012)). The combination of measured effective (half-light) radius R_e and velocity dispersion σ of a dSph with simple dynamical arguments can constrain the total mass of the dwarf within R_e . The upper mass limits derived for the eight most massive satellites of the MW (excluding the Magellanic clouds) are systematically smaller than those of the 10 most massive subhalos in high-resolution cosmological simulations, within the same radii. Therefore, the most massive subhalos cannot

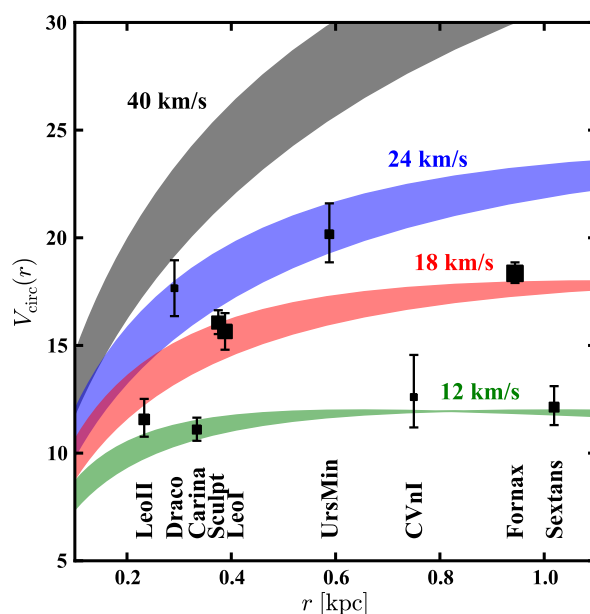


Figure 2.2: An Illustration of the TBTF problem. Shaded colored regions in this plot show the rotation curve corresponding to NFW subhalos with V_{\max} between 12 km/s and 40 km/s, and the data points (labeled) correspond to nine brightest dSphs of the MW (the thickness of each data is representative of the luminosity of the satellite galaxy). While MW-sized halos in Aquarius simulations have on average 10 satellites with $V_{\max} \geq 30$ km/s, all luminous MW satellites show $V_{\max} < 24$, and only Draco (the least luminous dSph in the presented sample) shows consistency with a CDM subhalo of $V_{\max} \approx 40$ km/s (Figure from Boylan-Kolchin, Bullock, & Kaplinghat 2012).

host the most luminous dSphs of the MW. Consequently, unless the MW halo is a very peculiar system, the most massive subhalos of the galaxy remain dark while the most luminous dSphs reside in intermediate-mass dark matter halos (see Figure 2.2).

One suggested explanation for this mismatch is that the halo of the MW is less massive than previously estimated and therefore, the local massive dSphs should be compared to simulated subhalos of a less-massive halo (Boylan-Kolchin, Bullock, & Kaplinghat 2012; Vera-Ciro et al. 2013). However, a similar discrepancy has been observed within the local group (Kirby et al. 2014; Garrison-Kimmel et al. 2014; Tollerud, Boylan-Kolchin, & Bullock 2014), and even field galaxies (Papastergis et al. 2015) as well, which argues for a more global issue, in need of a more generic solution.

2.2.4 Spatial distribution, or the plane of satellites problem

The issue with the spatial distribution of satellite galaxies of the MW was first argued to be challenging for Λ CDM by Kroupa, Theis, & Boily (2005). Even though the spatial distribution of the (then) 11 satellite dwarves of the MW was not a new discovery, the fact that this alignment proposes a challenge to the standard model of cosmology was new and in line with the rest of the small-scale issues proposed for this model. Upon the discovery of faint and ultra faint

satellites of our galaxy in the SDSS survey, the presence of the satellite plane around the MW was confirmed (Metz, Kroupa, & Jerjen 2009; Kroupa et al. 2010). The bonus argument made by Metz, Kroupa, & Jerjen (2009) uses not only the spatial distribution of dwarf satellites, but also their proper motions which is indicative of the majority of their sample orbiting within the vast plane of satellites (VPoS). A later work by Pawlowski, Kroupa, & Jerjen (2013) also confirms these results based on proper motion measurements. The first question coming to mind in such a situation is whether this is limited to the local group or this is the case outside the local group as well. This question is addressed by various works ever since, both in the context of the (satellite and field) dwarf galaxies in our local group (see e.g. Ibata et al. 2013; Pawlowski, Kroupa, & Jerjen 2013; Bellazzini et al. 2013; Pawlowski & McGaugh 2014) and around more distant galaxies (see e.g. Tully et al. 2015; Müller, Jerjen, & Binggeli 2015). Even though the narrow dwarf galaxy plane of the MW is a widely-accepted feature in the data, the ubiquity of such planes in the rest of the Universe is under debate and needs further observational data with velocity measurements of satellite pairs in order to confirm (or reject) them co-orbiting the host galaxy (for opposite views on the matter see e.g. Phillips et al. 2015; Cautun et al. 2015).

3

Gravitational Lensing

The deflection of light is a predictable phenomenon in the framework of Newtonian mechanics, serving as one of the major tests of general relativity by the famous 1919 solar eclipse experiment (Eddington 1919). In the Newtonian description, light photons are treated as test particles being influenced by gravity of a massive object. Therefore, a test particle passing with velocity v near a point-like massive object, M , with an impact parameter ξ , is deflected by an angle α . Considering a very small deflection angle (the most likely case in cosmology), α is given by

$$\alpha \simeq \frac{4GM}{v^2 \xi}. \quad (3.1)$$

In the case of a light beam, where $v = c$, passing very close to the surface of the Sun, the deflection angle turns out to be ~ 0.85 arcseconds. This value coincides with what was obtained by Einstein prior to the final formulation of GR (Einstein 1911). However, the pre-relativistic predicted deflection angle is half the predicted angle by general relativity in its fully developed form. The factor added by general relativity represents the local spatial curvature produced by the mass and was proven to be consistent with observational results in 1919 for the first time. Several groups measured the angular shift of stars projected close to the solar limb during a total eclipse (Eddington 1919). This served as the second evidence in support of GR, after the perihelion precession of Mercury. Based on the calculation using the generalization of this phenomenon for two distant stars, it was generally accepted that the separated images of a star due to the gravity of another star would be impossible to detect with the technology of the day. A few years later, Fritz Zwicky suggested that the effect of an extragalactic “nebula”, i.e. a galaxy, rather than a foreground star is big enough and should be observable (Zwicky 1937). Even though his calculation was too optimistic due to overestimating the masses of galaxies at that time, the idea of utilizing this phenomenon as a “natural telescope” remained a curiosity until 1979 when for the first time two identical quasars (0957 + 561 A & B) were revealed in an observation (Walsh, Carswell, & Weymann 1979). The similarity of the spectra of the two quasars with the same redshifts, $z \sim 1.41$, and 6 arcseconds angular separation were mostly accepted to be convincing evidence for the fact that the two objects are physically associated. Furthermore, finding a galaxy at a lower redshift close to the two images lent more support to

the idea that this was a case of gravitational lensing. Many cases of gravitational lensing have been found and investigated ever since.

3.1 Mathematical Description

Here I start with the geometrical framework for gravitational lensing assuming a point-like lens (the same calculation for an extended lens requires integrating over the projected lens area). Another simplifying factor is the “thin lens approximation”, implying that the impact parameter of the lens is considerably small compared to the distances in the system, thus the extension of the lens along the line of sight is ignored.

The relation between the unlensed source position, β , and the position of the image(s), θ , is called the *lens equation*. This equation can be derived geometrically from the setup displayed in Figure 3.1 and shown below:

$$\beta = \theta - \frac{D_{ds}}{D_s} \hat{\alpha}(\xi). \quad (3.2)$$

where the image position is $\theta = \frac{\xi}{D_d}$. Hence, by substituting α with the expression found in equation 3.1, we have

$$\beta = \theta - \frac{D_{ds}}{D_s D_d} \frac{4GM}{c^2 \theta}. \quad (3.3)$$

Alternatively, using the distance from the source to the optical axis, in the source plane, $\eta = D_s \beta$, the lens equation becomes

$$\eta = \frac{D_s}{D_d} \xi - D_{ds} \hat{\alpha}(\xi) \quad (3.4)$$

Given a certain mass distribution and a fixed ξ , the lens equation can have more than one solution for θ ; each of which corresponds to a macroimage. Although obtaining the source position η from a given image position ξ using the lens equation is straightforward, finding a general analytical solution for the position of the image(s) of a source at a given position is not. The mapping of ξ to η is non-linear. There are, however, analytical models to solve this equation for simple matter distributions on the lens plane such as point-mass, axially symmetric, and elliptical lenses.

The deflection angle due to the surface mass density of the lens gives rise to a deflection potential ψ of the form $\alpha = \nabla\psi$. Accordingly, another way of presenting the lens equation is in the form of

$$\mathbf{y} = \nabla \left(\frac{1}{2} \mathbf{x}^2 - \psi(\mathbf{x}) \right) \quad (3.5)$$

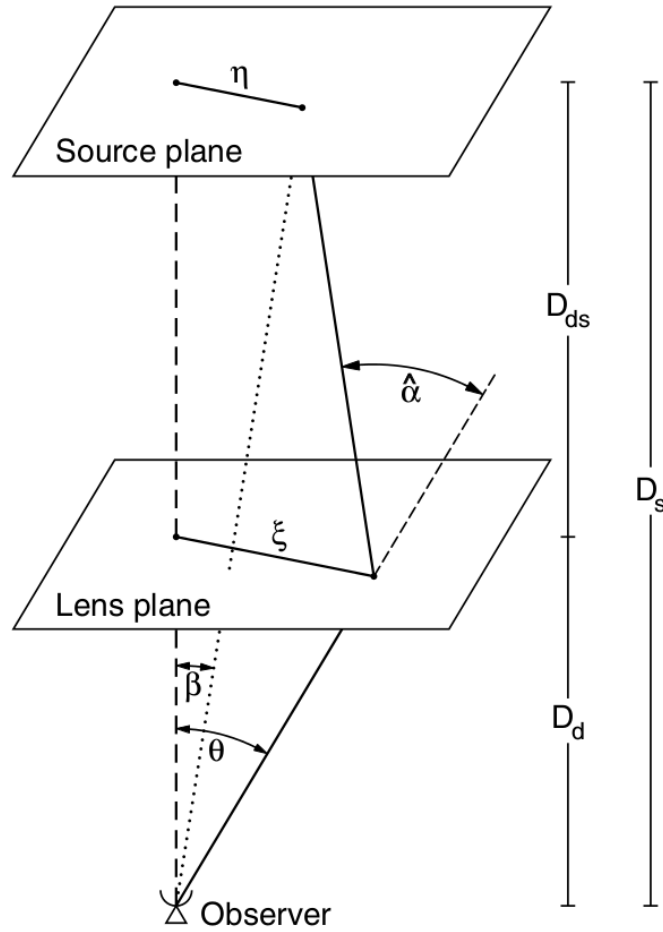


Figure 3.1: The general setting of a gravitational lens system. The relation between angular distances and luminosity distances is described by the lens equation. In this schematic figure, η is the position vector of the source with respect to the optical axis of the system, and ξ is the position vector of the outer surface of the [spherically symmetric] deflector. (Figure from Meylan et al. 2006)

where $\mathbf{x} \equiv \frac{\xi}{\xi_0}$ and $\mathbf{y} \equiv \frac{\eta}{\eta_0}$ are dimensionless vectors, when ξ_0 and η_0 are length scales in the lens plane and the source plane, respectively. This form of expressing the lens equation leads to the formulation of Fermat's principle in gravitational lensing theory

$$\nabla\phi(\mathbf{x}, \mathbf{y}) = 0 \quad (3.6)$$

where ϕ is a scalar function as below

$$\phi(\mathbf{x}, \mathbf{y}) = \frac{1}{2}(\mathbf{x} - \mathbf{y})^2 - \psi(\mathbf{x}) \quad (3.7)$$

Fermat's principle states that the light ray always chooses the path which takes the least *time* to pass through. Therefore, it can be used to relate the time delay between two separate images of a single source to the considered cosmology and mass distribution of the lens.

Light deflection is a propagation phenomenon, influencing only the shape of the light bundle from the source, and not the surface brightness. Therefore, for a monochromatic source, we have the received flux from the source as

$$S = I_\nu d\omega \quad (3.8)$$

where $d\omega$ is the differential solid angle, and I_ν is the monochromatic surface brightness. Since I_ν is not affected by gravitational deflection, the flux changes are merely mirrored in solid angle variation of the image. Hence, the *magnification* due to gravitational lensing is defined as the solid angle ratio of the observed image to that of the non-lensed source

$$|\mu| \equiv \frac{d\omega}{d\omega_0} \quad (3.9)$$

On the other hand, the solid angle is related to the angular position of the image (source), via the dimensionless quantities \mathbf{x} (\mathbf{y}). Therefore, the magnification due to a circularly symmetric lens is given by

$$|\mu| = \frac{\theta d\theta}{\beta d\beta}. \quad (3.10)$$

In case of extended sources, we need to solve the lens equation for all points within the source and derive the observed surface brightness distribution in the lens plane $I(\boldsymbol{\theta})$ from the true surface brightness distribution in the source plane $I^s(\boldsymbol{\beta}(\boldsymbol{\theta}))$. The lens mapping can be locally linearized and the image distortion written as a Jacobian matrix of

$$\mathcal{A}(\boldsymbol{\theta}) = \frac{\partial \boldsymbol{\beta}}{\partial \boldsymbol{\theta}} \quad (3.11)$$

The magnification tensor, – locally – mapping the source plane to the image plane for an extended source is then

$$M(\boldsymbol{\theta}) = \mathcal{A}^{-1} \quad (3.12)$$

whose determinant corresponds to the magnification factor introduced in equation 3.9, and could be derived from the relative [integrated] fluxes of the images and the source.

$$\mu = \det(M) = \frac{1}{\det(\mathcal{A})} \quad (3.13)$$

One of the most interesting and extreme cases of gravitational lensing is the Einstein ring. The lensing setup which gives rise to a complete Einstein ring consists of a point-like source, with a spherically symmetric lens, both of which are collinear with the observer, i.e. the lens is centered at the line of sight between the observer and the source. Therefore, the observer sees a ring-shaped image with an angular radius of θ_E which is called the angular Einstein radius. This radius, θ_E is obtained by substituting $\beta = 0$ in equation 3.3 as:

$$\theta_E = \sqrt{\frac{4GM}{c^2} \frac{D_{ds}}{D_d D_s}}. \quad (3.14)$$

Where M represents the lens mass and D_d , D_s , and D_{ds} are the angular-diameter distances as in Figure 3.1. Moreover, as it is immediately concluded from equation 3.10, magnification μ diverges for the *critical points* where $\beta = 0$. The “infinite” theoretical magnification points can be mapped into the source plane which gives a set of *caustic curves*. This corresponds to the points where $\det(\mathcal{A}) = 0$, and therefore equation 3.13 faces division by zero. In reality, however, the finite size of the source keeps the magnification from diverging. The number and relative positions of images of a single source change according to the position of the source with respect to such caustics in the source plane.

3.2 Strong Lensing

One observable result of gravitational lensing is magnified (or de-magnified) images of point sources, the other distortions in the images of extended objects. The extent of the lensing effect varies depending on the alignment of the source, the lens and the observer. The closer the center of the lens to the line of sight between the observer and the source, the more significant the image distortion. Therefore, gravitational lensing cases are categorized, according to the level of their magnifications, into two major regimes; *strong* and *weak* lensing. Strong lensing causes dramatic effects such as high magnifications, multiple images, luminous arcs and in some cases even complete Einstein rings. Although strong lensing is a rare effect, it is possible to be detected and studied individually for each case. Weak lensing, on the other hand, occurs

when the center of the lens is further away from the observer's line of sight, i.e. $\theta > \theta_E$. Thus the images are weakly magnified or have small distortions. In contrast to strong lensing, weak lensing happens to be very common. Every line of sight is affected by weak lensing at some level hence this effect is detectable through statistical investigations of numerous objects.

As pointed out in the previous section, the lens equation (equation 3.3) can have multiple solutions. Moreover, when the “thin lens approximation” is valid, the surface mass density of the lens, i.e. the projected mass of the lens on the lens plane, determines the severity of the gravitational lensing case. Accordingly, one can introduce the constant *critical surface mass density* Σ_{crit} such that for every θ in the lens equation 3.3, we have $\beta = 0$.

$$\Sigma_{\text{crit}} = \frac{c^2}{4\pi G} \frac{D_{os}}{D_{ol}D_{ls}}. \quad (3.15)$$

In cases where $\Sigma > \Sigma_{\text{crit}}$, multiple images from the background source are produced. Exceeding the critical surface mass density may happen only for a part of a specific foreground galaxy or galaxy cluster, the solid angle of which is then called the *strong lensing cross section*.

On the other hand, the magnification of the image due to the presence of the lens which was defined by equation 3.9, can also be expressed with the following relation

$$\mu = \frac{1}{(1 - \kappa)^2 - |\vec{\gamma}|^2} \quad (3.16)$$

which is obtained by substituting the determinant of the Jacobian matrix for the lens equation. In this form, there are two quantities upon which the magnification is dependent, *convergence* κ and *shear* vector $\vec{\gamma}$. Convergence, which describes the local isotropic magnification of the source, is a scalar quantity and is defined as the surface mass density of the lens in the unit of the critical surface density as below

$$\kappa \equiv \frac{\Sigma}{\Sigma_{\text{crit}}} \quad (3.17)$$

Shear is the measurement of the distortion of the source image and is quantified along each position component on the lens plane, thus a vector. The magnification for point sources is a tensor, only dependent on κ and $\vec{\gamma}$, however, for an extended source it is more complicated, depending on the internal surface brightness distribution of the source.

3.2.1 Astrometric Perturbation

The proximity of the projected image of a foreground massive object to a background source has effects on various angular scales. One effect is a change in the apparent position of the source. This is called the *astrometric effect* and is usually accompanied by magnification or distortion effect. Astrometric effects are, therefore, detectable mostly in dynamic cases, such as microlensing cases where the observer can actually follow the temporal differences in the

relative positions in the system. One of these cases stems from the presence of substructures in the main lens such that the deflector consists of a parent halo with a distribution of subhalos inside.

When it comes to the astrometric perturbation due to the substructure inside a halo, the macroimage gets shifted, under the influence of the subhalo, from its original position. This effect is mostly sensitive to intermediate and high mass substructures (Moustakas et al. 2009) and is clearly visible in the results of our modeling in the present work.

3.2.2 Time Delay

Each macroimage follows a different path to reach the observer, i.e. is subject to a different time delay. This time delay consists of two independent components; the geometrical and the gravitational component. The geometrical term comes from the difference in the light path length for each image. The gravitational component, also known as the *Shapiro* effect, is a relativistic effect of retardation in strong gravitational fields. However, different time delays of various images cannot be observed if the source is not intrinsically variable, since this effect is manifested in the phase difference of the light curves of various images. When it comes to subhalo hunting, the perturbation to the time delays between macroimages predicted by a smooth lens model serves as an evidence for the presence of substructures within the main lens. As Moustakas et al. (2009) argue, such an effect is only sensitive to subhalos at the high-mass end of the mass function. Time delay is the only dimensional quantity among the observables of a gravitational lens system, i.e. changes with the length scale of the lens setup. Given two lensing setups which differ in angular-diameter distances, the only variable which breaks the degeneracy of the observables is the time delays of various images.

3.2.3 Flux Ratio Anomalies

Gravitational lensing is a propagation phenomenon, thus it – in principle – conserves the number of photons. On the other hand, the gravitational deflection influences the cross section of the light bundle differentially. Consequently, in order to conserve the flux, the area of the image(s) of the source changes. This leads to different magnifications for different macroimages, as explained in equation 3.9. However, mere determination of the flux of a single image does not provide any information if the intrinsic flux of the source is unknown. The observable quantities, are rather the flux ratio and positions of two separate macroimages of a single source.

4

Radio interferometry

In this chapter, I briefly explain the main principles based upon which radio interferometers work. I also try to put radio interferometry into the context of radio astronomy as well as observational astronomy, in general.

4.1 Radio telescopes

A radio telescope is usually made of two main parts:

- Reflector: The special shape of this reflector, i.e. a parabola, is advantageous compared to concave mirrors – mostly – used in reflecting optical telescopes as the parabolic shape keeps all reflected radiation in phase and as I will repeatedly mention in this chapter, coherence is of great importance in radio astronomy. Keeping the same principle in mind, current radio instruments use aperture arrays keeping the electromagnetic wave coherent at the receiver by exerting appropriate delays to the signal. Parabolic antennas are sensitive to a very small area of the sky, i.e. they have high “directivity”, so an individual antenna is capable of seeing everything in a single pixel.
- Receiver: Of the main types of receivers used in radio astronomy, i.e. *heterodyne* and *bolometric* receivers, the ones relevant for interferometry are heterodyne receivers. Heterodyne receivers are the most common type of receivers at sub-mm wavelengths (and higher) and they are crucial to use if the signal modulation (both amplitude and phase of the signal) is needed for observations (the case in radio interferometers).

In order to digitally record the electromagnetic wavefront reaching the receiver, the signal needs to be sampled with a frequency at least twice the frequency of the wave (Nyquist theorem). This is an electronically challenging task, and particularly impossible for frequencies in the order of 100 GHz and higher. Therefore, the arriving signal is first mixed with the signal from a stable local oscillator (LO) with a well-known frequency slightly lower than that of the original signal. The mixed signal then has two frequencies $f_{\text{sky}} + f_{\text{LO}}$ and $f_{\text{sky}} - f_{\text{LO}}$. Therefore, we can sample the low frequency signal with as fine resolution as desired, ignoring the higher

frequency. The signal is then demixed by exerting a phase difference and is recorded in two frequency windows below and above the LO frequency, namely the *lower sideband* and the *upper sideband*, by the receiver.

4.2 Observational limitations

Observational limitations of the recorded data may come from the source or, more commonly, from our instruments and can be classified into limitation in

- resolution
- sensitivity
- dynamic range

As will be discussed further into the chapter, radio interferometry has brought significant improvements in the former two, although mostly at the cost of the latter.

The convolution theorem

What a radio telescope records is not the direct image of the source at different points at the same time. Rather, a single radio telescope records signals from the primary beam into a single “pixel”. Radio interferometry is based on *the convolution theorem*. According to this theorem, it can be shown that convolving two functions in Fourier space (i.e. Fourier transform of their convolution) is equivalent to multiplying the Fourier transform of the two in the ordinary space.

$$\mathcal{F}(f * g) = \mathcal{F}(f) \times \mathcal{F}(g) \quad (4.1)$$

Where convolution of one function $f(t)$ with another function $g(t)$ means shifting the function g consecutively from $t = -\infty$ to $t = +\infty$, while at each step the multiplication of the two functions (i.e. $f(t)g(t + \tau)$) is added to the convolved function $f * g$:

$$(f * g)(\tau) = \int_{-\infty}^{+\infty} f(t)g(t + \tau)dt \quad (4.2)$$

No device can achieve infinite resolution due to its diffraction limit which results in spreading the light from a point source, a.k.a. the point spread function (PSF) of the instrument. Anything observed with that instrument will be seen as the convolution of the true source structure with the PSF. Angular resolution of an instrument (i.e. FWHM of its PSF) scales with the size of the aperture and wavelength as $\Delta\theta \propto \lambda/D$. Therefore, the PSF itself scales with the square of the Fourier transform of the aperture which, according to the convolution theorem, equals the Fourier transform of the autocorrelation of the aperture. Therefore, in order to increase the resolving power of an instrument, one needs to either increase the aperture size or decrease the observing wavelength. Interferometry effectively allows for an increase in the aperture size. While the latter solution might not be possible to arbitrary large extent due to different physical emission mechanisms, the former is one of the reasons for using the interferometry technique.

4.3 Two-element interferometer

When we talk about interferometry, clarification is needed to distinguish between the common picture of Young's optical double-slit interferometer and the concepts and techniques used in radio interferometers. In the optical case, the fringe pattern made on the detector plane is a distribution of points with various intensities $I(x) = |E_1(x) + E_2(x)|^2$, and visibility is a real quantity between 0 and 1 defined as below:

$$V = \frac{I_{\max} - I_{\min}}{I_{\max} + I_{\min}} \quad (4.3)$$

Visibility in the case of radio interferometry, however, is a complex quantity describing the time correlation of the two signals reaching the two elements of the interferometer and can be expressed as below:

$$V(\tau) = \langle E_1(t)E_2^*(t + \tau) \rangle \quad (4.4)$$

with τ being the geometrical time delay between the two signals due to the different paths the wave needs to reach each antenna.

$$\tau = \frac{\vec{B} \cdot \vec{S}}{c} \quad (4.5)$$

Where \vec{B} is the three-dimensional distance vector between the two elements, a.k.a. *baseline*, \vec{S} is the source vector and c is the speed of light.

Practically, the time delay τ of one signal with respect to the other is added to the signal electronically to correct for this effect before sending the two signals to the correlator. Applying the geometrical time delay τ is equivalent to projecting the baseline connecting the two telescopes on the plane perpendicular to the direction of the source. Therefore, what matters in all math hereafter is the *projected* baseline between the two antennas, rather than the actual baseline.

The correlated signal is a complex visibility describing the response of the interferometer to the two signals, both amplitude and phase, received from a point source which is a fringe pattern (on the sky) perpendicular to the projected baseline (BL_{proj}) as seen from that point on the sky. What happens in radio interferometry is that we sample the visibility values on this plane depending on the position of the source, BL_{proj} , and duration of observations. The interferometer's response to an extended source is simply the superposition of the response patterns of various point sources making up the extended source. In other words, the measured visibility is the integral of source structure multiplied by the response. Therefore,

$$V_{\text{observed}} = \int V_{\text{response}}^{\text{point source}} I(x, y) dx dy. \quad (4.6)$$

Where x and y are celestial coordinates and $I(x, y)$ is the intensity distribution of the extended source.

The van Cittert–Zernike theorem and the interferometer equation

As long as the source we are observing is far enough that the wavefronts from the source can be approximated as plane waves (i.e. Fraunhofer approximation applies), the complex visibility of the source only depends on the relative position of the two antennae, and the wavelength of the observations. The visibility function, then, is a measure of the spatial coherence of the wavefront of the source encoding the source structure in it.

$$V^{AB} = \langle E_A \times E_B^* \rangle = \mathcal{F}\left(\frac{\vec{R}_A - \vec{R}_B}{\lambda}\right) \quad (4.7)$$

The left hand side is, by definition, the complex visibility of the source, $\vec{R}_A - \vec{R}_B$ is the observing baseline, and \mathcal{F} is the Fourier transform of the source structure $I(x, y)$. Therefore, rewriting the interferometer equation, one finds:

$$V(x, y, z) = \int_{x,y} I(x, y) e^{-\frac{2\pi i}{\lambda}(ux+vy+wz)} \frac{dxdy}{z} \quad (4.8)$$

where $z = \sqrt{1 - x^2 - y^2}$. The wz term is made zero by adding a time–delay shift to the signal and if x and y are small enough, the relation above is reduced to a Fourier transform between $I(x, y)$ and $V(u, v)$. This interferometry equation transforms the intensities on the source plane to visibilities on the (u, v) plane and their values depend on the coordinates of the observing baseline, projected on the source plane, as well as the structure of the source and the observing frequency.

4.4 Aperture synthesis

Back to the definition of visibility in radio interferometry, one can directly conclude that a multi–element interferometer is only a combination of several two–element interferometers, sampling the (u, v) space in pairs, based on their projected baseline and the observing frequency, measuring the visibility at those sample points only.

Snapshot observations

Fourier transform is blind to the absolute baseline position, but as baseline is a vector, it does carry information about the direction. This implies that in a multi–element interferometer, a [arbitrary] frame of reference is needed for combining the antenna pairs and calculating the transformation from the ordinary plane to the (u, v) plane. The (u, v) coverage in a snapshot is equal to the autocorrelation of the array configuration as seen by the source – except for the central point which corresponds to the measurement with the hypothetical $BL = 0$, impossible to implement in practice.

Since Fourier transform is a *Hermitian* transformation, a single baseline corresponds to sampling not one, but two points on the visibility plane; one at (u, v) , and the other at $(-u, -v)$. Moreover, if $I(x, y)$ is a real number, $V(u, v) = V^*(-u, -v)$. This means that each baseline

gives two separate visibility measurements, meaning that adding even one more antenna to the array has a significant effect on better sampling the (u, v) plane; one via increasing the number of baselines ($N_{BL} = \frac{N_{ant}(N_{ant}-1)}{2}$), and the other, via double-sampling each baseline as mentioned above. Therefore, a mono-frequency snapshot made by an interferometer with N_{ant} antennae makes $2N_{BL}$ discrete visibility measurements where longer baselines in the (u, v) plane correspond to smaller scales on the image plane and vice-versa. Besides, as seen in equation 4.8, the conversion between the (x, y) plane and (u, v) plane is scaled by the observing frequency. Therefore, a wider observing bandwidth results in a wider radial coverage of the (u, v) plane. As (u, v) coordinates are measured in wavelength one way of filling the Fourier space is to observe at multiple wavelengths simultaneously – given that the source looks the same in all these wavelengths. The other way to increase the discrete sampling of (u, v) space, closer to a continuous sampling (in the tangential direction), is longer exposure time. In this mode, the Earth rotation leads to a continuous change in projected baselines of the array as seen by the source and hence more (u, v) coverage.

Two extreme regions of the (u, v) plane are usually the most challenging to fill. Long baselines (corresponding to small scales on the image plane) are difficult to achieve for obvious practical reasons while the longest baseline in the array sets the angular resolution of the reconstructed image and obviously the impossibility of infinite baselines make infinite resolution also impossible! On the other hand, short spacings on the (u, v) plane can also be challenging to achieve because of the minimum spacing forced by antenna sizes. This leads to a fundamental feature of any (u, v) sampling known as “zero-spacing hole”. The lack of visibility measurements on this scale corresponds to missing any smooth large-scale structure of the source. In cases where an unrecovered diffuse component does exist in the original source, the integrated flux of the source measured using the interferometer would be smaller than the integrated flux of the target measured by a single-dish telescope. This is a tell-tale signature of the presence of a large unrecovered structure in the source and is known as “the missing flux” problem. The problem arises due to the poor (or lack of) sampling the short spacings on the (u, v) plane. Therefore, the intensity profile of an internally Gaussian source lacks data points in the center thus visibility interpolation tends to flatten out the peak. In many cases, sampling the short spacings with a more compact array or a single-dish telescope helps constrain the light profile of the source.

Aperture synthesis and image reconstruction

Aperture synthesis is the technique of reconstructing an image from incomplete sampling of the Fourier space. The technique is based on modeling the visibility plane based on the existing samplings. Therefore, the more complete the (u, v) coverage the closer the model image to the real one seen by the array. However, there will always be holes in the sampled (u, v) plane limiting the fidelity and quality (i.e. dynamic range = $\frac{\text{peak}}{\text{RMS}}$ of the reconstructed image.)

Fourier transform of the (u, v) coverage gives the so-called “dirty beam” (equivalent to the point spread function PSF) while the Fourier transform of the measured visibilities on the (u, v) plane results in the “dirty image” of the source, which is, as expected, the actual source structure convolved with the dirty beam. Now that we have images of both the beam and the source, we

can deconvolve the beam from the image. Remember that deconvolution is non-linear and non-unique! (See §4.4 to read about the CLEAN algorithm.)

In aperture synthesis, modeling is applied while working in the image plane. The process is such that the dirty beam and dirty image are calculated based on the (u, v) coverage and direct visibility measurements, respectively. For this purpose, the (u, v) plane is required to be gridded.¹ At this step, Nyquist sampling of the (u, v) plane introduces a limitation in the image space, i.e. grid size/cell size needs to be chosen such that the final PSF includes at least 3 pixels in the image plane. The next step in image reconstruction is deconvolving the beam from the dirty image. The actual interpolation happens here! Deconvolution is not a unique process and hence requires not only gridding the (u, v) plane but also making assumptions about the deconvolving beam. One assumption that needs to be made is how to weight the measured visibilities. This question, in turn, has two parts: How are the measured visibilities in one (u, v) pixel weighted? and what is the relative weight of various pixels on the (u, v) plane? Different choices at this step result in different angular resolution and dynamic range limitations in the model image.

Natural weighting as it sounds is simply weighting visibilities inversely proportional to the variance of their distribution. Therefore, short-spacings in the (u, v) plane, with closer samplings, are weighted more than longer baselines which results in higher dynamic range in the modeled image at the cost of angular resolution. In other words, the dirty beam has larger FWHM but less prominent side lobes (compared to the rms noise). Therefore, it is best for imaging faint and smooth sources.

Uniform weighting is the same as natural weighting with an additional factor inversely proportional to the number of visibilities in each pixel. Therefore, it boosts the contribution from long-spacings by giving the same weight to visibilities at all (u, v) distances, even though those at long distances are sampled more coarsely. This property makes this approach more suitable for sources with rich and complicated structure. Although, the source needs to be bright enough for this approach to work best. This is because this weighting scheme results in a narrow(er than naturally-weighted) PSF with smaller side lobes and therefore, better angular resolution. However, the RMS of the residuals of this model tends to be large(r than that of natural by at least an order of ~ 2), i.e. poorer sensitivity.

Briggs weighting is a tunable combination of both approaches above. The tunability of Briggs' recipe is applied through the *robust* parameter. This parameter changes in the range of -2 to +2 from uniform to natural weighting. Usually, *robust*=0.5 gives a good compromise between the two extreme approaches. Although it still depends on the preferences based on the scientific target.

¹In fact, this is the issue one faces when using *Fast* Fourier transform (FFT), while *direct* Fourier transform does not require gridding the (u, v) plane. One would expect the resulting image to be nearly the same as the model obtained by natural weighting. However, direct FT is so much slower that it is not worth practicing as long as the visibilities are sampled wisely!

(u, v) tapering is useful when the observed source is extended and most of the information lies in short baselines. Therefore, in order to improve the sensitivity to emission at larger spatial scales, we can overweight the measurements made using these baselines even further and decrease the weight of measurements where we have a lower signal, i.e. long baselines. This can be done via Gaussian circular tapers in the (u, v) plane. If the source has a very extended structure, which is remained unrecovered due to the short-spacing hole in the (u, v) coverage, even with natural weighting, then (u, v) tapering is the last resort to recover that diffuse emission.

As a matter of fact, one might want to get rid of an extended emission they are not interested in, and focus more on the small-scale clumpy structure of their source. In which case, one only needs to apply an inverse Gaussian taper to the (u, v) plane.

The method used in **Paper II** is based on combining different weightings of the same measurement set to put emphasis on features with different angular scales.

CLEAN algorithm and deconvolving the dirty beam

While interferometry data are incomplete due to lack of information on some spatial frequencies, we can interpolate the (u, v) plane by applying our prior information about the source structure as the criteria required to proceed with deconvolution. Clearly, the more our prior information about the source, the more reliable the model image is.

The problem of deconvolving the dirty beam from the dirty image has non-unique solutions. An intuitive way to show this is to assume a source with non-zero visibilities everywhere but where we are making our measurements, i.e. our (u, v) coverage. This class of sources remain invisible to the interferometer, as long as the (u, v) coverage is the same. Now, one can add *any* combination of these “invisible” sources to our reconstructed image without the measurement set changing. Improving the (u, v) coverage will decrease the number of these combinations and therefore, increase the image fidelity and yet *high* fidelity is not the same as *infinite* fidelity. Therefore, the reconstructed image always remains a model of our real data.

CLEAN (Högbom 1974) is the oldest, fastest and best deconvolution algorithm practiced today for image reconstruction in radio interferometry. This algorithm starts at the maximum flux point in the image, subtracts the PSF at that point and adds a 2-D Gaussian component (with the same FWHM of the PSF and scaled flux) to the CLEAN image instead. The algorithm then repeats these three steps for the peak in the residual map until either of the criteria below is met:

- Noise limit: If the peak in the residual map has a smaller value than $\alpha\sigma_{\text{RMS}}$ (α is an arbitrary coefficient set by the scientific purpose of the image.)
- Dynamic range limit: If the peak in the residual map has a smaller value than $\frac{1}{\alpha} \times f_{\text{max}}$ of the dirty beam
- Maximum number of CLEAN cycles, which is an experimental (arbitrary) criterion.

Finally, what the algorithm produces are three matrices below:

CLEAN model: A set of point sources subtracted from the dirty image where flux peaks are located.

CLEAN beam: The corresponding Gaussian to the dirty beam. In other words, the PSF model. If the dirty beam is elliptical, then the CLEAN beam is also a similarly-elliptical Gaussian.

CLEAN image: It is simply the CLEAN model convolved with the CLEAN beam and is the final product of the image reconstruction procedure.

While different deconvolution algorithms apply different criteria to the source structure, the CLEAN algorithm's basic assumption is that the source is made of discrete Dirac delta functions, i.e. point sources. Therefore, it tends to convert smooth and diffused components into clumpy ones. While one does not lose real emission by not CLEANing it, it is possible to get artificial features by CLEANing noise!

The current commonly-used implementation of CLEAN is the Cotton-Schwab CLEAN which consists of two same-level, linked cycles. Start with a **Minor cycle** as below:

1. Locate the peak intensity in the dirty image.
2.
 - (a) Subtract a dirty beam centering at the point of the peak, from the dirty image.
 - (b) Compute the residual image = image used in step (1) – product of (2.a).
 - (c) Scale down the flux density in residual image to **g** times the image peak, where **g** is the arbitrary CLEAN gain value.
3.
 - (a) Add a point-like component to the CLEAN model, at the position of the peak.
 - (b) Set the flux density of the point in CLEAN model to the peak of the PSF.
 - (c) Convolve the newly-added point of the CLEAN model with the CLEAN beam and add it to the CLEAN image
4. Use the product of step (2.b) in step (1).

A **Major cycle**, then, follows the minor cycle as below:

1. Compute model visibilities corresponding to the CLEAN model made in the minor cycle.
2. Compute the residual visibilities = observed visibilities – model visibilities made in step(1).
3. FFT the residual visibilities and feed it to the next minor cycle

While the CLEANing process seems complete within the minor cycle, the major cycle is needed because the algorithm (minor cycle only) cannot subtract anything from marginal parts of the image where we have no information about possible sources in those regions whose side lobes (only!) affect our dirty image.

Summary

With the fast improvement of observational facilities the required angular resolution and sensitivity for the discovery of compound lens systems is becoming available. Given all the uncertainties concerning the existence, abundance, mass function, and inner mass distribution of dark matter substructure, it is important to estimate the alignment probabilities of lens substructures combined with the detection limits. It is important to keep in mind that with a detailed picture of model expectations at hand even null detections provide constraints on the background model.

In **Paper I** we use simulations of strongly lensed quasar jets as expected by three different VLBI configurations and receivers to probe dark matter substructure. The dark matter substructure in this paper is assumed to consist of intermediate-mass black holes (i.e. point-like) and ultracompact minihalos ($\rho \propto r^{-2.5}$) within the main lens at $z \simeq 0.5$. We demonstrate that small-scale morphological distortions in one of the macroimages – that is not replicated in others in a large number of macrolensed jet systems with the expected (submilliarcsecond) resolution of the array is used to set constraints on detection limits of such substructures and their abundance. We argue that intermediate-mass black holes with $M_{\text{IMBH}} \sim 10^3\text{--}10^6 M_{\odot}$ are detectable and therefore, non-detections of such distortions rule out their contribution in the surface mass fraction down to $f_{\text{IMBH}} \gtrsim 0.01$ in the dark matter halo of the main lens at the position of the macroimage. The same investigation for ultracompact minihalos (that have a central density slope slightly steeper than the isothermal profile $\rho \sim r^{-2.5}$) places a constraint of $f_{\text{UCMH}} \gtrsim 0.1$ on their contribution to the dark matter budget of the main lens. While we show that standard CDM halos (with NFW density profile) with $M_{\text{FNW}} \simeq 10^8 M_{\odot}$ also produce detectable distortions due to the far shallower central density profile ($\rho \propto r^{-1}$), their effective lensing cross section is too small for the probability of successful alignments to be of any interest ($P_{\text{milli}} \sim 10^{-4}$).

The extremely low probability of proper alignment for standard CDM subhalos presented in **Paper I**, brings us to **Paper II** in which we adopt a similar approach to investigate small-scale perturbations using simulations of multiply-lensed sub-mm galaxies (SMGs). These sources provide 10-100 times more coverage of the lens plane. This paper investigates simulations of compound lens systems where the lensed source is a dusty star-forming galaxy at $z = 2$ where ALMA band 7, 8, and 9 (with frequency coverage between 275 – 720 GHz) probes the dust continuum emission of the source with submilliarcsecond angular resolution. We aim for lens

perturbers of $M_{\text{sub}} = 10^5 - 10^{10} M_{\odot}$ in a Milky Way-sized halo. This is the relevant mass range for both the “missing satellite problem” 2.2.1 and the “core-cusp problem” 2.2.2. The analysis in this paper uses different weighting schemes for simulated complex visibilities and instrumental noise effects are taken into account. We use not only the local (small-scale) lens effects of substructures but also the astrometric shift of the main lens solution to place constraints on the presence, mass and central density slope of the lens perturber (substructure). In this paper, we demonstrate that SIS perturbers down to $M_{\text{vir}} \approx 3 \times 10^7 M_{\odot}$ will be detectable with 2hr observations with the full ALMA array. Moreover, we argue that while these observations could, in principle, be used to tell the difference between the observational signature of a compact SIS and a lens subhalo with NFW (or Einasto) profile, the shape parameter (α_{Ein} for Einasto or γ in general NFW) remains highly degenerate with the subhalo mass. In the end of **Paper II** we draw attention to different mass definitions used in lens modelings (M_{einstein} , the projected mass within the Einstein radius of the lens) and cosmological simulations (M_{tidal} , the 3D tidally-truncated mass of a subhalo that is being dissolved in the parent halo) to argue that the conversion between the two strongly depends on the assumptions made in the process of deprojection.

Bibliography

- Baer H., Choi K.-Y., Kim J. E., Roszkowski L., 2015, PhR, 555, 1
- Begeman K. G., 1989, A&A, 223, 47
- Bellazzini M., Oosterloo T., Fraternali F., Beccari G., 2013, A&A, 559, L11
- Bennett C. L., et al., 2013, ApJS, 208, 20
- Bergström L., 2013, PhST, 158, 014014
- Bloomfield J. K., 2013, PhDT,
- Bosma A., 1981, AJ, 86, 1825
- Boylan-Kolchin M., Bullock J. S., Kaplinghat M., 2012, MNRAS, 422, 1203
- Boylan-Kolchin M., Bullock J. S., Kaplinghat M., 2011, MNRAS, 415, L40
- Brooks A. M., Kuhlen M., Zolotov A., Hooper D., 2013, ApJ, 765, 22
- Bullock J. S., Kolatt T. S., Sigad Y., Somerville R. S., Kravtsov A. V., Klypin A. A., Primack J. R., Dekel A., 2001, MNRAS, 321, 559
- Bullock J. S., Stewart K. R., Kaplinghat M., Tollerud E. J., Wolf J., 2010, ApJ, 717, 1043
- Cautun M., Wang W., Frenk C. S., Sawala T., 2015, MNRAS, 449, 2576
- Clifton T., 2006, PhDT
- Clifton T., Ferreira P. G., Padilla A., Skordis C., 2012, PhR, 513, 1
- Clowe D., Bradač M., Gonzalez A. H., Markevitch M., Randall S. W., Jones C., Zaritsky D., 2006, ApJ, 648, L109
- Del Popolo A., Lima J. A. S., Fabris J. C., Rodrigues D. C., 2014, JCAP, 4, 021
- Del Popolo A., 2014, IJMPD, 23, 1430005

- Di Cintio A., Brook C. B., Dutton A. A., Macciò A. V., Stinson G. S., Knebe A., 2014, MNRAS, 441, 2986
- Doroshkevich A. G., Shandarin S. F., Saar E., 1978, MNRAS, 184, 643
- Dubinski J., Carlberg R. G., 1991, ApJ, 378, 496
- Dutton A. A., Macciò A. V., 2014, MNRAS, 441, 3359
- Eddington A. S., 1919, Natur, 104, 372
- Einasto J., 1965, TrAlm, 5, 87
- Einasto J., Saar E., Kaasik A., Chernin A. D., 1974, Natur, 252, 111
- Einstein A., 1911, AnP, 340, 898
- Sales L. V., Gurovich S., 2012, MNRAS, 425, 2817
- Gao L., Navarro J. F., Cole S., Frenk C. S., White S. D. M., Springel V., Jenkins A., Neto A. F., 2008, MNRAS, 387, 536
- Garrison-Kimmel S., Boylan-Kolchin M., Bullock J. S., Kirby E. N., 2014, MNRAS, 444, 222
- Gelmini G. B., 2015, arXiv, arXiv:1502.01320
- Gil-Marín H., et al., 2015, MNRAS, 452, 1914
- Guo Q., et al., 2011, MNRAS, 413, 101
- Högbom J. A., 1974, A&AS, 15, 417
- Hayashi E., White S. D. M., 2008, MNRAS, 388, 2
- Ibata R. A., et al., 2013, Natur, 493, 62
- Kennedy R., Frenk C., Cole S., Benson A., 2014, MNRAS, 442, 2487
- Kirby E. N., Bullock J. S., Boylan-Kolchin M., Kaplinghat M., Cohen J. G., 2014, MNRAS, 439, 1015
- Klypin A., Karachentsev I., Makarov D., Nasonova O., 2015, MNRAS, 454, 1798
- Klypin A., Kravtsov A. V., Valenzuela O., Prada F., 1999, ApJ, 522, 82
- Kroupa P., et al., 2010, A&A, 523, A32
- Kroupa P., Theis C., Boily C. M., 2005, A&A, 431, 517
- Lundmark K., 1930, Lund Medd., 125, 110
- Müller O., Jerjen H., Binggeli B., 2015, A&A, 583, A79

- Macciò A. V., Dutton A. A., van den Bosch F. C., 2008, MNRAS, 391, 1940
- Melott A. L., Einasto J., Saar E., Suisalu I., Klypin A. A., Shandarin S. F., 1983, PhRvL, 51, 935
- Metz M., Kroupa P., Jerjen H., 2009, MNRAS, 394, 2223
- Meylan G., Jetzer P., North P., Schneider P., Kochanek C. S., Wambsganss J., 2006, glsw.conf,
- Moore B., Ghigna S., Governato F., Lake G., Quinn T., Stadel J., Tozzi P., 1999, ApJ, 524, L19
- Moustakas L. A., et al., 2009, astro, 2010, 214
- Navarro J. F., et al., 2004, MNRAS, 349, 1039
- Navarro J. F., Frenk C. S., White S. D. M., 1996, ApJ, 462, 563
- Navarro J. F., et al., 2010, MNRAS, 402, 21
- Oh S.-H., de Blok W. J. G., Brinks E., Walter F., Kennicutt R. C., Jr., 2011, AJ, 141, 193
- Ostriker J. P., Peebles P. J. E., Yahil A., 1974, ApJ, 193, L1
- Papastergis E., Giovanelli R., Haynes M. P., Shankar F., 2015, A&A, 574, A113
- Pawlowski M. S., Kroupa P., Jerjen H., 2013, MNRAS, 435, 1928
- Pawlowski M. S., McGaugh S. S., 2014, MNRAS, 440, 908
- Pawlowski M. S., McGaugh S. S., Jerjen H., 2015, MNRAS, 453, 1047
- Percival W. J., et al., 2002, MNRAS, 337, 1068
- Perlmutter S., et al., 1999, ApJ, 517, 565
- Phillips J. I., Cooper M. C., Bullock J. S., Boylan-Kolchin M., 2015, MNRAS, 453, 3839
- Planck Collaboration, et al., 2015, arXiv, arXiv:1502.01589
- Riess A. G., et al., 1998, AJ, 116, 1009
- Rubin V. C., Ford W. K., Jr., 1970, IAUS, 38, 61
- Rubin V. C., Thonnard N., Ford W. K., Jr., 1978, ApJ, 225, L107
- Sawala T., et al., 2015, arXiv, arXiv:1511.01098
- Sawala T., et al., 2014, arXiv, arXiv:1412.2748
- Stadel J., Potter D., Moore B., Diemand J., Madau P., Zemp M., Kuhlen M., Quilis V., 2009, MNRAS, 398, L21

- Tollerud E. J., Boylan-Kolchin M., Bullock J. S., 2014, MNRAS, 440, 3511
- Tully R. B., Libeskind N. I., Karachentsev I. D., Karachentseva V. E., Rizzi L., Shaya E. J., 2015, ApJ, 802, L25
- Vera-Ciro C. A., Helmi A., Starkenburg E., Breddels M. A., 2013, MNRAS, 428, 1696
- Walker M. G., Peñarrubia J., 2011, ApJ, 742, 20
- Walsh D., Carswell R. F., Weymann R. J., 1979, Natur, 279, 381
- Zwicky F., 1937, ApJ, 86, 217
- Zwicky F., 1933, AcHPh, 6, 110

Paper I

Hunting for dark halo substructure using submilliarcsecond-scale observations of macrolensed radio jets

Erik Zackrisson,¹★ Saghar Asadi,¹ Kaj Wiik,² Jakob Jönsson,³ Pat Scott,⁴
Kanan K. Datta,¹ Martina M. Friedrich,¹ Hannes Jensen,¹ Joel Johansson,³
Claes-Erik Rydberg¹ and Andreas Sandberg¹

¹Department of Astronomy, Stockholm University, Oscar Klein Center, AlbaNova, SE-106 91 Stockholm, Sweden

²Tuorla Observatory, Department of Physics and Astronomy, University of Turku, Väisäläntie 20, FI-215 00 Piikkiö, Finland

³Department of Physics, Stockholm University, Oscar Klein Center, AlbaNova, SE-106 91 Stockholm, Sweden

⁴Department of Physics, McGill University, 3600 Rue University, Montréal, QC H3A 2T8, Canada

Accepted 2013 February 18. Received 2013 January 14; in original form 2012 August 23

ABSTRACT

Dark halo substructure may reveal itself through secondary, small-scale gravitational lensing effects on light sources that are macrolensed by a foreground galaxy. Here, we explore the prospects of using Very Long Baseline Interferometry (VLBI) observations of multiply-imaged quasar jets to search for submilliarcsecond-scale image distortions produced by various forms of dark substructures in the 10^3 – $10^8 M_\odot$ mass range. We present lensing simulations relevant for the angular resolutions attainable with the existing European VLBI Network, the global VLBI array and an upcoming observing mode in which the Atacama Large Millimeter Array (ALMA) is connected to the global VLBI array. While observations of this type would not be sensitive to standard cold dark matter subhaloes, they can be used to detect the more compact forms of halo substructure predicted in alternative structure formation scenarios. By mapping approximately five strongly lensed systems, it should be possible to detect or robustly rule out primordial black holes in the 10^3 – $10^6 M_\odot$ mass range if they constitute $\gtrsim 1$ per cent of the dark matter in these lenses. Ultracompact minihaloes are harder to detect using this technique, but 10^6 – $10^8 M_\odot$ ultracompact minihaloes could in principle be detected if they constitute $\gtrsim 10$ per cent of the dark matter.

Key words: gravitational lensing: strong – galaxies: jets – quasars: general – dark matter.

1 INTRODUCTION

A generic prediction of the standard cold dark matter (CDM) scenario is that a substantial fraction of the total mass of galaxy-sized dark matter haloes (~ 10 per cent; Gao et al. 2011; Maciejewski et al. 2011) should be in the form of bound substructures (a.k.a. subhaloes or subclumps) left over from the process of hierarchical assembly. The fact that the number of substructures seen in CDM simulations greatly outnumbers the satellite galaxies detected in the vicinity of the Milky Way and Andromeda constitutes the so-called ‘missing satellite problem’ (Klypin et al. 1999; Moore et al. 1999). While it has been argued that astrophysical processes that quench star formation in low-mass haloes may explain this discrepancy (e.g. Macciò et al. 2010; Font et al. 2011), this implies that a vast population of extremely faint or completely dark substructures should be awaiting discovery in the haloes of galaxies. Provided

that CDM is in the form of Weakly Interacting Massive Particles (WIMPs), these subhaloes are in principle detectable by the *Fermi* Gamma-ray Space Telescope because of their annihilation fluxes. However, *Fermi* has so far failed to detect any unambiguous signal from such objects (e.g. Belikov, Buckley & Hooper 2012; Hooper & Linden 2012; Zechlin et al. 2012, but see Bringmann et al. 2012b and Su & Finkbeiner 2012 for a different view).

Gravitational lensing may provide an independent test for the presence of dark halo substructures (for a review, see Zackrisson & Riehm 2010). A foreground galaxy that happens to be aligned with a background light source can produce multiple images of the background object, with a typical image separation of ~ 1 arcsec (an effect known as strong lensing or macrolensing). While simple, smooth models of galaxy lenses are usually able to reproduce the positions of these macroimages, their observed flux ratios are more difficult to explain. Such flux-ratio violations have been interpreted as evidence of substantial small-scale structure within the main lens (e.g. Mao & Schneider 1998; Chiba 2002; Keeton, Gaudi & Petters 2003; Kochanek & Dalal 2004). A notable problem with this picture

★ E-mail: ez@astro.su.se

is that current CDM simulations predict too little substructure to explain many of these flux-ratio violations (e.g. Macciò & Miranda 2006; Xu et al. 2009; Chen, Koushiappas & Zentner 2011 – but see Metcalf & Amara 2012), possibly pointing to a considerable contribution from low-mass haloes elsewhere along the line of sight (Xu et al. 2010, 2012) or some additional form of substructure (dark or luminous) within the lens.

A slightly different lensing approach exploits the small-scale distortions that halo substructure is expected to introduce in the morphologies of extended macroimages. Substructures of mass $\gtrsim 10^8 M_\odot$ can perturb gravitational arcs and Einstein rings on scales resolvable with the *Hubble Space Telescope* (Vegetti & Koopmans 2009a,b) and detections of $\sim 10^8$ – $10^{10} M_\odot$ objects have already been made in this way (Vegetti, Czoske & Koopmans 2010a; Vegetti et al. 2010b, 2012). In line with the flux-ratio anomaly results, these observations seem to suggest a subhalo mass fraction that is significantly higher than predicted by standard CDM, and possibly also a flatter subhalo mass function slope (Vegetti et al. 2010b, 2012).

By mapping extended macrolensed sources with milliarcsecond or submilliarcsecond resolution using Very Long Baseline Interferometry (VLBI) techniques at radio wavelengths, substructures at even lower masses can in principle be detected. Such objects may introduce kinks and bends in multiply-imaged quasar jets (Wambsganss & Paczynski 1992; Metcalf & Madau 2001) and one detection of a $\sim 10^5$ – $10^7 M_\odot$ object has already been claimed using this technique (Metcalf 2002). In this situation, the lensing effects produced by halo substructures can be separated from intrinsic morphological features in jets, since the latter would be reproduced in all macroimages whereas dark matter clumps in the halo of the lens would affect each macroimage differently. Similar methods for exploiting the lensing effects produced by halo substructures on scales of ~ 100 mas down to ~ 0.01 mas have also been explored by Yonehara, Umemura & Susa (2003), Inoue & Chiba (2003, 2005a,b), Hisano, Inoue & Takahashi (2006), Ohashi, Chiba & Inoue (2009), Riehm et al. (2009) and Hezaveh et al. (2012). However, effects of this type tend to be sensitive to the density profiles of substructures, and may be undetectable for all but the very densest, most extreme forms of substructure (Zackrisson et al. 2008).

Here, we use lensing simulations to explore the prospects of using macrolensed quasar jets observed at submilliarcsecond resolution, in searches for standard CDM subhaloes, ultracompact minihaloes (UCMHs) and primordial black holes within the main lens. These different forms of substructure are described, along with previous constraints on such objects, in Section 2. The details of our simulations and assumptions are covered in Section 3. In Section 4, we present our results and in Section 5 we discuss some lingering issues with the adopted technique. Section 6 summarizes our findings.

2 DIFFERENT FORMS OF HALO SUBSTRUCTURE

2.1 Standard CDM subhaloes

At $z = 0$, the CDM scenario predicts the existence of dark matter haloes with masses ranging from $\sim 10^{15} M_\odot$ down to the cut-off in the density fluctuation spectrum, which is set by the detailed properties of the CDM particles. For many types of WIMPs, this cut-off lies somewhere in the range $\sim 10^{-11}$ to $10^{-3} M_\odot$ (Bringmann 2009). Alternative models involving superweakly interacting particles (super-WIMPs), MeV mass dark matter or a long-range interaction between dark matter particles may place the cut-off as high as $\sim 10^3$ – $10^{10} M_\odot$ (Hisano, Inoue & Takahashi 2006; Hooper

et al. 2007; van den Aarssen, Bringmann & Pfrommer 2012), although the upper end of this range may be in conflict with the apparent masses of the lightest dwarf galaxies ($\sim 10^6 M_\odot$; Geha et al. 2009).

As these low-mass haloes merge to form more massive ones, some temporarily survive in the form of subhaloes within the larger haloes. N -body simulations indicate that the subhaloes within a galaxy-sized CDM halo should follow a mass function of the type:

$$\frac{dN}{dM_{\text{sub}}} \propto M_{\text{sub}}^{-\alpha}, \quad (1)$$

with $\alpha \approx 1.9$ (Springel et al. 2008; Gao et al. 2011). The relative contribution from subhaloes with mass $M \gtrsim 10^5 M_\odot$ to the dark matter surface mass density at the typical location of macroimages in a galaxy-mass lens is $f_{\text{sub}} \approx 0.002$ (Xu et al. 2010), albeit with a large scatter (Chen et al. 2011).

The density profiles of isolated field haloes in CDM simulations can be reasonably well described by Navarro, Frenk & White (Navarro, Frenk & White 1996; hereafter NFW) profiles:

$$\rho(R) = \frac{\rho_i}{(R/R_S)(1 + R/R_S)^2}, \quad (2)$$

where R_S is the characteristic scale radius of the halo. The slope of the inner density cusp ($\beta = d \ln \rho / d \ln r$) in this profile is $\beta = -1$, and this makes it difficult for NFW haloes in the dwarf-galaxy mass range to produce millilensing effects of the type we are considering in this paper. Typically, cusp slopes obeying $\beta \lesssim -1.5$ would be required (Zackrisson et al. 2008). Later work has shown that models with inner cusp slopes that become progressively shallower towards the centre provide even better fits to isolated haloes in CDM simulations, eventually reaching inner slopes of $\beta \geq -1$ (e.g. Navarro et al. 2010). In the context of detecting millilensing effects from low-mass haloes, this just makes matters worse, since the central density is reduced.

Once a halo falls into the potential well of a larger halo and becomes a subhalo, it is stripped of material – primarily from its outskirts – due to interactions with its host halo and with other subhaloes. This alters the density profile of the subhalo compared to an isolated halo of the same mass (e.g. Hayashi et al. 2003; Kazantzidis et al. 2004), but these modifications tend to diminish rather than enhance the ability of a CDM subhalo to produce detectable millilensing effects (Zackrisson et al. 2008).

To demonstrate that standard CDM subhaloes do not provide a significant ‘background’ of millilensing events in the observational situation that we consider, we have therefore adopted NFW profiles for these objects, since this results in an overoptimistic estimate on the millilensing effects that standard CDM subhaloes are likely to produce. Even then, the chances of detecting millilensing effects from these objects turn out to be negligible in the observational situations we are considering.

To derive the R_S values of our NFW subhalo profiles, we adopt the mass-dependent concentration parameters $c = R_{\text{vir}}/R_S$ from either Bullock et al. (2001) or Macciò, Dutton & van den Bosch (2008), where R_{vir} is the virial radius of the halo. Since both of these recipes predict higher concentration parameters for low-mass haloes, and since more centrally concentrated profiles (i.e. profiles with higher c) are more efficient in producing millilensing effects, we calculate the subhalo concentration parameters based on their current masses rather than the masses they had prior to becoming subhaloes. Since nearly all subhaloes have lost considerable amounts of material (e.g. Vale & Ostriker 2006), this also results in overly optimistic millilensing properties.

2.2 Intermediate-mass black holes

Intermediate-mass black holes (IMBHs; here assumed to have masses $\sim 10^3\text{--}10^6 M_\odot$) may either form primordially (typically when the Universe is $\ll 1$ s old), or due to the collapse of baryonic objects later on. The primordial variety could in principle comprise a substantial fraction of the dark matter, although a host of observational constraints makes this seem unlikely (for a recent compilation, see Carr et al. 2010).

The strongest upper limits on the cosmological density of primordial black holes in the $10^3\text{--}10^5 M_\odot$ mass range come from the effect that accretion on to these objects would have on the cosmic microwave background radiation (Ricotti, Ostriker & Mack 2008). Primordial black holes with masses $\sim 10^3\text{--}10^4 M_\odot$ are also strongly constrained by the effects of gravity waves on pulsar timing measurements (Carr et al. 2010; Saito & Yokoyama 2010), and at $M \gtrsim 10^4 M_\odot$ by dynamical constraints (Carr & Sakellariadou 1999). Using a technique first proposed by Kassiola, Kovner & Blandford (1991), Wilkinson et al. (2001) moreover used the absence of millilensing effects in non-macrolensed radio sources to place upper limits on IMBHs at $M \gtrsim 10^5 M_\odot$. It has, however, been argued that some of these constraints may be sidestepped under certain circumstances, and that both the size evolution of early-type galaxies (Totani 2010) and entropy considerations (Frampton et al. 2010) favour scenarios in which essentially all of the dark matter is in the form of $\sim 10^5 M_\odot$ primordial black holes.

IMBHs that were not produced primordially may instead either form as the end products of very massive Population III stars (e.g. Madau & Rees 2001), through the direct collapse of gas in small haloes at high redshift (e.g. Begelman, Volonteri & Rees 2006) or the collapse of dense star clusters (e.g. Devecchi & Volonteri 2009; Davies, Miller & Bellovary 2011). Such IMBHs may now be hiding in globular clusters (e.g. Vesperini et al. 2010), in satellite galaxies (van Wassenhove et al. 2010), or be freely floating in the haloes of galaxies (e.g. Micic, Holley-Bockelmann & Sigurdsson 2011). There is indeed some evidence for IMBHs in globular clusters (e.g. Noyola et al. 2010), and IMBHs may also explain some of the ultraluminous X-ray sources detected in other galaxies (e.g. Feng & Soria 2011; Webb et al. 2012). However, since only a small fraction of the cosmic baryons can be locked up in these non-primordial IMBHs, their relative contributions to the halo masses of galaxies are typically expected to be small ($f_{\text{IMBH}} \lesssim 10^{-5}$; e.g. Islam, Taylor & Silk 2004; Kawaguchi et al. 2008).

When simulating the potential millilensing effects of IMBHs, we treat the surface mass density fraction f_{IMBH} in IMBHs at the position of the macroimages as a free parameter, and for simplicity assume all IMBHs to have the same mass. In the case where the number density profile of IMBHs has the same shape as the density profile of the dark halo, f_{IMBH} also corresponds to the halo mass fraction in IMBHs. This is expected to be the case for primordial black holes, even if they constitute no more than a small fraction of the dark matter, since such objects behave just like CDM particles in N -body simulations. In the case of IMBHs formed through baryonic processes, the number density profile of IMBHs may well deviate significantly from the overall dark matter profile, and an f_{IMBH} estimate obtained from strong lensing observations cannot directly be interpreted as halo mass fraction without further constraints on the baryon distribution within the lens.

In principle, primordial black holes may over time accrete substantial amounts of dark matter and develop dark matter haloes of their own (Mack, Ostriker & Ricotti 2007), similar to the UCMHs discussed in Section 2.3. IMBHs forming through the collapse of

Pop III stars in minihaloes may also be surrounded by their own, highly contracted dark matter haloes (Sandick et al. 2011). Such compound objects are expected to have lensing properties intermediate between IMBHs and UCMHs, but are not treated in detail in our simulations.

2.3 Ultracompact minihaloes

Primordial density perturbations with $\Delta\rho/\rho \equiv \delta \lesssim 0.3$ are too small to form primordial black holes as they enter the horizon. Those with $\delta \gtrsim 10^{-3}$ may nonetheless still be large enough to seed the formation of UCMHs (Berezinsky, Dokuchaev & Eroshenko 2003, 2006, 2007, 2008; Ricotti & Gould 2009; Berezinsky et al. 2010a; Bringmann, Scott & Akrami 2012a). Such perturbations might be produced during phase transitions, around topological defects, or in the primordial spectrum of perturbations from inflation. The dark matter contained in these perturbations would collapse into UCMHs shortly after matter-radiation equality, via radial infall from a universally cold, smooth cosmological background. This radial collapse would leave UCMHs with much steeper central density profiles than standard CDM haloes (Ricotti & Gould 2009).

If dark matter exists in the form of self-annihilating WIMPs, UCMHs would be gamma-ray emitters, and strong limits on their cosmological density have already been derived from the effect that this would have on *Fermi*-LAT source identifications, the diffuse gamma-ray background and cosmic reionization (Scott & Siversson 2009; Berezinsky et al. 2010a,b; Josan & Green 2010; Lacki & Beacom 2010; Yang et al. 2011a,b; Zhang 2011; Bringmann et al. 2012a; Shandera et al. 2012), similarly if dark matter decays rather than annihilates (Yang, Yang & Zong 2012). If dark matter does not annihilate or decay, UCMHs in the $\sim 10^{-2}\text{--}10^2 M_\odot$ range may still be detectable in the future by their astrometric lensing effects on Milky Way stars (Li, Erickcek & Law 2012).

Here, we explore to what extent submilliarcsecond observations of macrolensed jets would be able to constrain the properties of UCMHs. Because dark matter self-annihilation would reduce the central density of UCMHs (e.g. Scott & Siversson 2009), UCMHs made out of self-annihilating WIMPs would not be efficient millilenses. We therefore focus on UCMHs made out of non-annihilating dark matter (e.g. asymmetric dark matter, axions, sterile neutrinos).

Radial infall leads to a density profile $\rho \propto r^{-2.25}$, slightly steeper than the $\rho \propto r^{-2}$ profile of a singular isothermal sphere (often used to model lensing by the inner regions of large galaxies). The dark matter profile in a UCMH (see Ricotti & Gould 2009; Bringmann et al. 2012a, for a detailed discussion) is given by

$$\rho(r, z) = \frac{3 f_{\text{CDM}} M_{\text{UCMH}}(z)}{16\pi R_{\text{UCMH}}(z)^{\frac{3}{4}} r^{\frac{9}{4}}}, \quad (3)$$

where f_{CDM} is the cosmological fraction of matter in CDM, $M_{\text{UCMH}}(z)$ indicates the UCMH mass at redshift z and

$$\frac{R_{\text{UCMH}}(z)}{\text{pc}} = 0.019 \left(\frac{1000}{z+1} \right) \left(\frac{M_{\text{UCMH}}(z)}{M_\odot} \right)^{\frac{1}{3}} \quad (4)$$

is the UCMH radius, defined as the distance within which the density is at least twice that of the cosmological background. Following matter-radiation equality at z_{eq} , a UCMH born from an initial dark matter overdensity of mass M_i accretes both dark and baryonic matter as

$$M_{\text{UCMH}}(z) = \frac{z_{\text{eq}} + 1}{z + 1} M_i. \quad (5)$$

This accretion presumably cuts out when the cosmological background is no longer smooth, i.e. when the first substantial structure formation occurs and the smallest star-forming minihaloes appear. In this case, present-day UCMH masses and radii can be obtained by setting $z \sim 10$ in equations (3) and (4), so that

$$M_{\text{UCMH}}^0 \equiv M_{\text{UCMH}}(z \lesssim 10) = M_{\text{UCMH}}(z = 10), \quad (6)$$

$$R_{\text{UCMH}}^0 \equiv R_{\text{UCMH}}(z \lesssim 10) = R_{\text{UCMH}}(z = 10). \quad (7)$$

However, the finite temperature of the smooth cosmological background from which UCMHs accrete softens the density profile in the innermost region, due to conservation of angular momentum. This can be conservatively modelled as a cut-off at some inner radius r_{min} , inside which one assumes the density to be constant. Following previous work (Bringmann et al. 2012a), we adopt this strategy here, taking a flat density profile within

$$\frac{r_{\text{min}}}{R_{\text{UCMH}}^0} \approx 2.9 \times 10^{-7} \left(\frac{1000}{z_c + 1} \right)^{2.43} \left(\frac{M_{\text{UCMH}}^0}{M_{\odot}} \right)^{-0.06}. \quad (8)$$

Here z_c refers to the redshift of UCMH collapse (the point at which the growth of the matter overdensity becomes non-linear); we adopt $z_c = 1000$, also in line with earlier work (Ricotti & Gould 2009; Bringmann et al. 2012a).

3 LENSING SIMULATIONS

To simulate the effects of dark halo substructure on the morphologies of macrolensed jets, we use a numerical scheme similar to that developed by Metcalf & Madau (2001). An extended source is assumed to be multiply-imaged by a foreground galaxy, and the lens equation is used to determine the lens plane positions of the corresponding macroimages. A small region around each such macroimage is then populated with randomly distributed dark halo substructures and simulated in greater detail. The deflection angles (with contributions from both substructures and the macrolens) are computed for every pixel within this region and converted into a numerical surface brightness map of the macroimage. These maps are initially generated with a very fine pixel scale, but are then convolved with a Gaussian filter to match the finite resolution of the VLBI arrays we consider. Both the resolution and the intrinsic source dimensions are determined by the frequency at which we assume the jets to be observed, as described in Sections 3.1 and 3.2.

The macrolens is modelled as a singular isothermal sphere (as appropriate for early-type galaxies acting as strong lenses; e.g. Rusin, Kochanek & Keeton 2003) at $z_l = 0.5$, with line-of-sight velocity dispersion $\sigma_v = 240 \text{ km s}^{-1}$, giving a mass of $\sim 10^{13} M_{\odot}$ within the virial radius, and two macroimages with separation ≈ 2 arcsec. We furthermore adjust the alignment of the source and main lens to ensure a macrolens magnification that is not unrealistically high. The simulations presented in this paper are all based on a lens-source configuration that in the absence of substructure would give magnifications $\mu_1 \approx 10$ and $\mu_2 \approx 8$ for the two macroimages. All simulations are based on a Λ CDM cosmology with $H_0 = 70 \text{ km s}^{-1} \text{ Mpc}^{-1}$, $\Omega_M = 0.27$ and $\Omega_{\Lambda} = 0.73$.

When distributing halo substructures within the simulated region, we for simplicity assume that the surface mass density across the macroimage is completely dominated by dark matter. While this assumption may be violated in multiply-imaged systems where one of the macroimages happens to lie very close to the lensing galaxy, this nonetheless seems to be a fair approximation in the majority of cases (e.g. Begelman et al. 2011; Pooley et al. 2012). In the case

of IMBHs and UCMHs, we moreover assume that their number densities trace that of the dark matter. The surface number density of such substructures then simply depends on their relative contribution to dark matter $\Omega_{\text{sub}}/\Omega_{\text{CDM}}$ and their mass distribution. These dark matter fractions in IMBHs and UCMHs are referred to as f_{IMBH} and f_{UCMH} , respectively. Since detailed predictions for the mass distribution of IMBHs and UCMHs are highly model-dependent, we assume all such objects to have the same mass, which we then vary to explore what parts of the $(f_{\text{IMBH}}, M_{\text{IMBH}})$ or $(f_{\text{UCMH}}, M_{\text{UCMH}})$ parameter space that a given set of observations would be able to probe.

In the case of standard CDM subhaloes, we adopt the mass distributions inferred from either simulations or observations. As discussed in Section 2.1, current simulations suggest $f_{\text{NFW}} = 0.002$ at the typical positions of macroimages in galaxy-sized dark haloes, and the subhalo mass function given by equation (1). However, since the recent lensing detections of subhaloes by Vegetti et al. (2010b, 2012) hint at a flatter mass function and a mass fraction that is an order of magnitude higher, we also explore the consequences of setting $f_{\text{NFW}} = 0.03$ and changing the mass function slope of equation (1) to $\alpha = 1.1$.

3.1 VLBI observations

A number of macrolensed radio jets are already known and have been observed using VLBI techniques (e.g. Garrett et al. 1994; King et al. 1997; Ros et al. 2000; Rusin et al. 2002; Biggs et al. 2004; York et al. 2005), although typically not with arrays capable of resolving submilliarcsecond scales. Designing a survey aimed to search for small-scale distortions in targets like these does, however, also involve other considerations than just the resolution. The frequency at which one chooses to observe these jets not only limits the resolution at which the jets can be mapped using suitable VLBI arrays, but also affects the intrinsic source size (e.g. Tornaiainen et al. 2008). To identify the observational strategy that maximizes the scientific output in terms of detection prospects for dark halo substructure, we here consider observations at three different frequencies, each using a different VLBI array:

- (i) Observations at 8.4 GHz using the global array, including the European VLBI Network (EVN¹) and the Very Long Baseline Array (VLBA²), giving a resolution of ≈ 0.7 mas.
- (ii) Observations at 22 GHz using the EVN, giving a resolution of ≈ 0.3 mas.
- (iii) Observations at 86 GHz using the full Atacama Large Millimeter Array (ALMA³) (66 antennas) connected to the global 3 mm array,⁴ giving a resolution of ≈ 0.05 mas. This observing mode is not available at the current time, but is likely to come online in a few years.

These arrays also have different sensitivities, which constrains the numbers of potential targets and also the apparent lengths of the jets. However, since we are simulating the effects of generic sources rather than individual targets, this is not addressed in our current simulations.

¹ <http://www.evlbi.org/>

² <http://www.vlba.nrao.edu/>

³ <http://www.almaobservatory.org/>

⁴ <http://www.mpifr-bonn.mpg.de/div/vlbi/globalmm/>

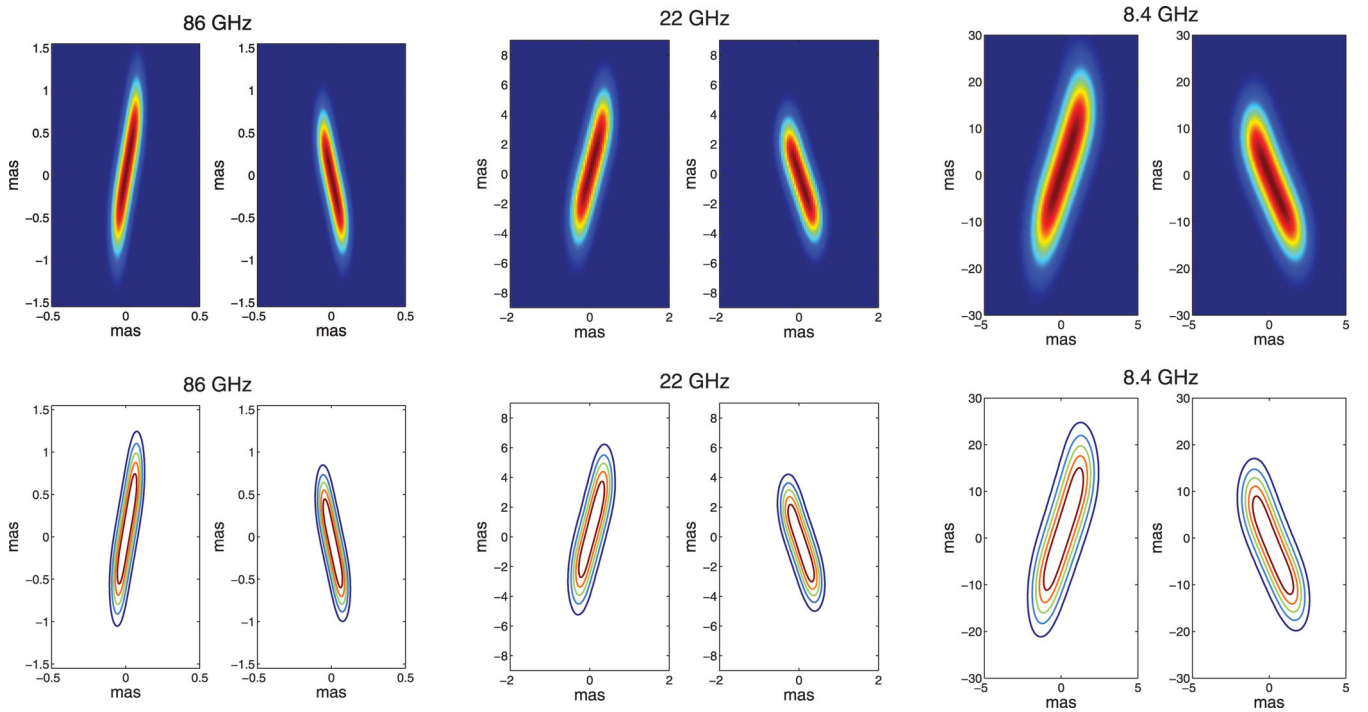


Figure 1. Simulated radio maps of strongly lensed quasar jets at 86, 22 and 8.4 GHz, respectively, from left to right (source sizes 2×0.5 pc, 10×2.5 pc and 40×10 pc), without any substructure lensing effects. The two subplots of each image show the two macroimages of the source. The bottom row contains the contour representations of the macroimages in the upper row, with the outermost contours corresponding to ≈ 10 per cent of the peak flux in these images. Please note the different scales of the images at the three frequencies.

3.2 Source size and morphology

We assume the source to be an intrinsically straight jet with a two-dimensional Gaussian surface brightness profile and length 40, 10 and 2 pc at 8.4, 22 and 86 GHz, respectively, and a width that is a quarter of the length. These sizes are in a reasonable agreement with source size estimates presented in Tornainen et al. (2008) and the jet lengths calculated from the monitoring of jets in active galactic nuclei with VLBA experiments (MOJAVE) sample (Lister et al. 2009).⁵

The source morphology and length-to-width ratio are mainly adopted for illustrative purposes. The limits presented in Section 4 are fairly insensitive to these assumptions, and depend mainly on the intrinsic jet area, as further discussed in Sections 5.2 and 5.3. At fixed angular resolution, a larger jet results in a stronger constraint whereas a smaller jet makes the constraints weaker. The results of Section 4 can therefore be rescaled to accommodate other jet sizes. In broad terms, our assumptions on the source sizes are similar to those used by Inoue & Chiba (2003).

4 RESULTS

In Fig. 1, we present our simulated images of strongly lensed quasar jets at 86, 22 and 8.4 GHz. Each image pair in the figure corresponds to the two macroimages of a single radio jet as produced by the main lens in the absence of any millilensing effects. While initially generated using a much smaller pixel scale, these images have been degraded using a Gaussian filter to match the resolution relevant for observations at these frequencies (0.05, 0.3 and 0.7 mas, respectively). The bottom row shows the corresponding isoflux contour

plots, where the outermost contours correspond to ≈ 10 per cent of the peak flux in these images. All subsequent figures depict how these contours are distorted by various kinds of halo substructure within the main lens. Around 30 simulated lensing maps of this type are generated for each combination of M_{IMBH} and f_{IMBH} (Section 4.1), or M_{UCMH} and f_{UCMH} (Section 4.2), with randomized substructure positions for each realization, in the derivation of the detection probabilities.

4.1 Detecting intermediate-mass black holes

In Fig. 2 we present examples of the simulated macroimages in the case where a fraction $f_{\text{IMBH}} = 0.02$ of the dark halo of the main lens is in the form of IMBHs with mass $M_{\text{IMBH}} = 10^3 - 10^6 M_{\odot}$. In this case, 86 GHz observations (ALMA + global array) are assumed, implying the smallest jet size (intrinsic length 2 pc) and the highest resolution (0.05 mas) considered in this paper. Since f_{IMBH} is kept fixed, the number of IMBHs per unit area drops by a factor of 10^3 in the lens plane when going from $M_{\text{IMBH}} = 10^3 M_{\odot}$ to $10^6 M_{\odot}$. However, because the more massive IMBHs also have larger Einstein radii, potentially detectable distortions are produced in all the cases plotted. Since the distortions in the two macroimages are uncorrelated, millilensing should also be straightforward to separate from intrinsic jet features (but see Section 5 for potential caveats).

The probability of seeing millilensing effects in at least one macroimage of a given two-image system depends on M_{IMBH} , the angular resolution and f_{IMBH} , but is deemed to be $P_{\text{milli}} \gtrsim 50$ per cent in all the simulations presented in Fig. 2.

When analysing a survey of N such macrolens systems, the probability $P_{\text{detection}}$ of detecting millilensing becomes $P_{\text{detection}} = 1 - (1 - P_{\text{milli}})^N$. By adopting $P_{\text{milli}} \gtrsim 50$ per cent, one should therefore be able to rule out $f_{\text{IMBH}} = 0.02$ for IMBHs in the mass range

⁵ <http://www.physics.purdue.edu/MOJAVE/>

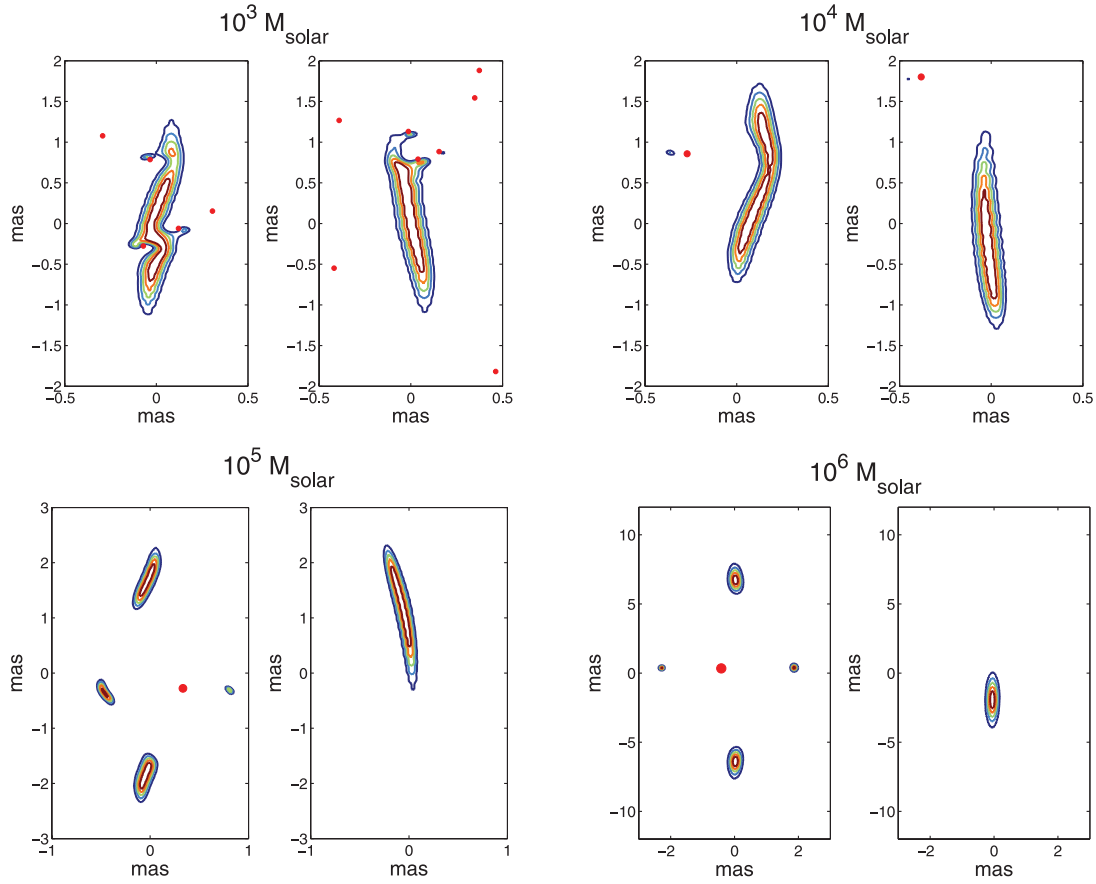


Figure 2. Examples of simulated radio maps of a macrolensed quasar jet at 86 GHz (source size 2×0.5 pc and resolution 0.05 mas), subject to millilensing distortions by IMBHs with $f_{\text{IMBH}} = 0.02$ in the halo of the main lens. Each image pair represents the two macroimages from Fig. 1, distorted by millilensing effects from IMBHs with either $M_{\text{IMBH}} = 10^3, 10^4, 10^5 M_\odot$ or $10^6 M_\odot$. The positions of the IMBHs are indicated by red dots. The slight macroimage distortions and displacements seen in right-hand panels for the 10^5 or $10^6 M_\odot$ cases are produced by IMBHs just outside the plotted region.

$M_{\text{IMBH}} = 10^3$ – $10^6 M_\odot$ at the $\gtrsim 95$ per cent level by surveying $N \approx 5$ systems. By further increasing the size of the survey, even lower f_{IMBH} can in principle be probed. To first order P_{milli} scales with f_{IMBH} , so that $P_{\text{milli}} \gtrsim 5$ per cent if $f_{\text{IMBH}} \sim 0.002$. Hence, to reach a detection probability of $P_{\text{detection}} \gtrsim 68$ per cent if $f_{\text{IMBH}} = 0.002$, one needs to observe $N \geq 22$ systems.

As demonstrated in Fig. 3, the larger source size assumed for the 22 GHz (EVN) observations (10 pc) allows IMBHs with dark matter fractions as low as $f_{\text{IMBH}} = 0.01$ to be detected with probability $P_{\text{milli}} \gtrsim 50$ per cent. The lower resolution (0.3 mas) provided by the EVN at the same time prohibits the detection of IMBHs with mass $M_{\text{IMBH}} \sim 10^3 M_\odot$. By surveying $N \approx 5$ systems, one should be able to rule out $f_{\text{IMBH}} = 0.01$ for $M_{\text{IMBH}} \sim 10^4$ – $10^6 M_\odot$ at 95 per cent confidence level. A detection probability of $P_{\text{detection}} \gtrsim 68$ per cent can also be reached at $f_{\text{IMBH}} = 0.001$ if one is able to observe $N \geq 22$ systems.

Similarly, the even larger jet (intrinsic length 40 pc) adopted for our simulated 8.4 GHz observations allows for stronger constraints on f_{IMBH} , but the lower resolution (0.7 mas) at the same time limits the IMBH mass range for which millilensing effects can be detected. Still, the macroimage distortions produced by 10^5 – $10^6 M_\odot$ IMBHs would be detectable with this resolution, and such effects would turn up with $P_{\text{milli}} \gtrsim 50$ per cent probability even if the IMBH halo mass fraction is as low as $f_{\text{IMBH}} = 0.005$. Fig. 4 includes an example

of such millilensing distortions produced by $10^5 M_\odot$ and $10^6 M_\odot$ IMBHs with $f_{\text{IMBH}} = 0.005$.

Table 1 summarizes the f_{IMBH} limits that observations of a single macrolensed jet (one image pair) at 86, 22 and 8.4 GHz would be able to probe (with ≥ 50 per cent detection probability). The constraints resulting from a survey of $N \approx 5$ systems would produce constraints that are a factor of a few better than the Wilkinson et al. (2001) millilensing constraints on $10^6 M_\odot$ primordial black holes.⁶ There are no competitive *lensing* constraints on IMBH at 10^3 – $10^5 M_\odot$, but there are still a host of other constraints that may be applicable, in particular those related to accretion on to these objects (see Carr et al. 2010, for a review).

⁶ Formally, the Wilkinson et al. (2001) constraints apply to millilenses located anywhere along the line of sight to the radio sources in their sample (mean redshift $z \approx 1.3$), whereas ours apply only to millilenses within the main lens. The difference may be relevant in scenarios in which the IMBHs do not follow the distribution of dark matter on large scales (e.g. if they are formed through baryonic processes in the vicinity of galaxies). Moreover, our approach could in principle produce somewhat stronger constraints if we were to consider millilenses along the entire line of sight.

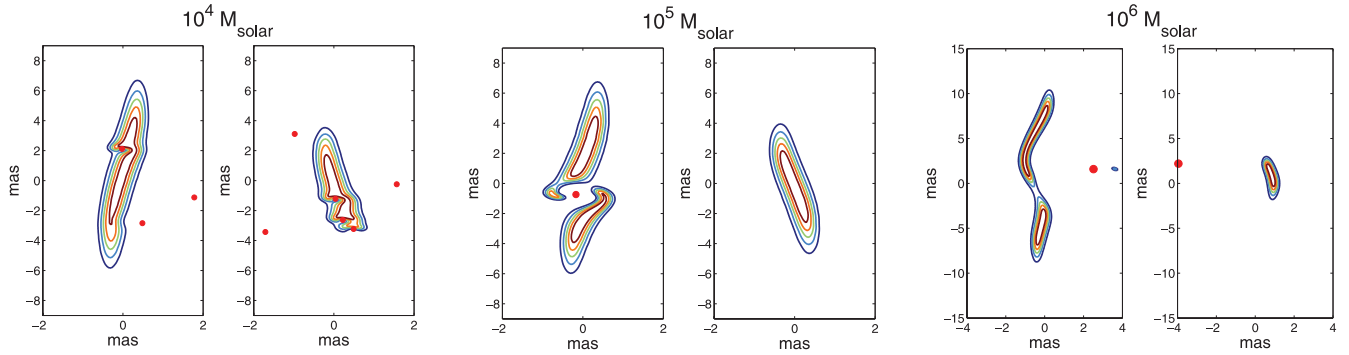


Figure 3. Examples of simulated radio maps of a macrolensed quasar jet at 22 GHz (source size 10×2.5 pc and resolution 0.3 mas), subject to millilensing distortions by IMBHs with $f_{\text{IMBH}} = 0.01$ in the halo of the main lens. Each image pair represents the two macroimages from Fig. 1, distorted by millilensing effects from IMBHs with either $M_{\text{IMBH}} = 10^4$, 10^5 or $10^6 M_{\odot}$. The positions of the IMBHs are indicated by red dots.

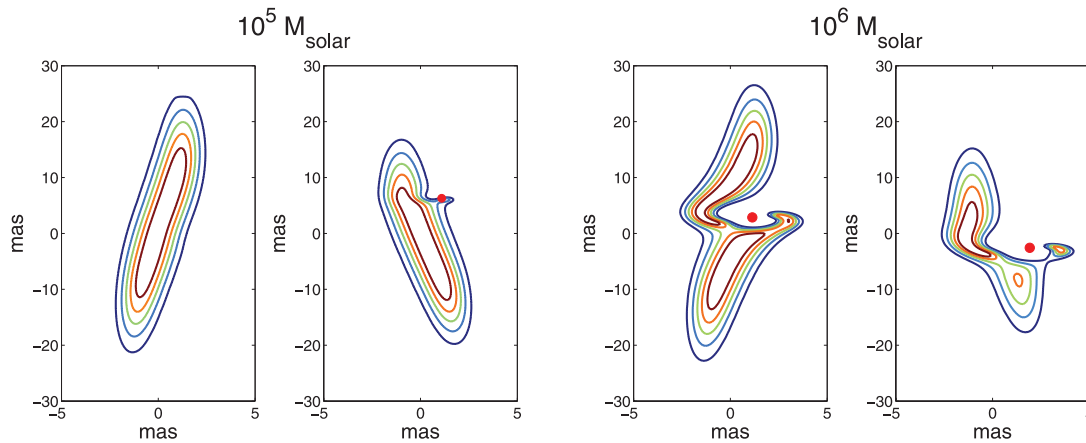


Figure 4. Examples of simulated radio maps of a macrolensed quasar jet at 8.4 GHz (source size 40×10 pc and resolution 0.7 mas), subject to millilensing distortions by IMBHs with $f_{\text{IMBH}} = 0.005$ in the halo of the main lens. Each image pair represents the two macroimages from Fig. 1, distorted by millilensing effects from IMBHs with either $M_{\text{IMBH}} = 10^5$ or $10^6 M_{\odot}$. The positions of the IMBHs are indicated by red dots.

Table 1. The lowest halo mass fraction in IMBHs, f_{IMBH} , that would produce detectable millilensing distortions with $P_{\text{milli}} \gtrsim 50$ per cent probability in a single macroimage pair.

Frequency (GHz)	Mass (M_{\odot})	Source size (pc)	min f_{IMBH}
86	10^3 – 10^6	2×0.5	2×10^{-2}
22	10^4 – 10^6	10×2.5	1×10^{-2}
8.4	10^5 – 10^6	40×10	5×10^{-3}

4.2 Detecting ultracompact minihaloes

When compared to IMBHs of the same mass, UCMHs have much smaller Einstein radii and are far more difficult to detect through millilensing effects. Our simulations show that while $M_{\text{UCMH}} \sim 10^6$ – $10^8 M_{\odot}$ UCMHs may in principle be detectable through small-scale macroimage distortions, the probability of observing this effect is exceedingly small unless the UCMH dark matter fraction f_{UCMH} is very high.

In Fig. 5, we show examples of the millilensing distortions that 10^6 and $10^8 M_{\odot}$ UCMHs would produce in the case of 86 GHz observations (ALMA + the global array). However, the probability of seeing effects of this type in a given macroimage pair is only $P_{\text{milli}} \approx 10$ per cent, even for a UCMH dark halo fraction as high as $f_{\text{UCMH}} = 0.2$. The detection prospects become somewhat better

at 22 and 8.4 GHz ($f_{\text{UCMH}} \gtrsim 0.05$ – 0.1 at $P_{\text{milli}} \approx 10$ per cent) due to the larger source adopted sizes at these frequencies, but only for 10^7 – $10^8 M_{\odot}$ objects (see Table 2).

By probing $N \approx 11$ (28) macroimage pairs, the detection probability can be pushed to $P_{\text{detection}} \approx 68$ per cent (95 per cent) at these f_{UCMH} limits. In order to probe UCMH dark halo fractions significantly below $f_{\text{UCMH}} \sim 0.1$, hundreds of images would therefore need to be observed. While there are no competitive lensing constraints at $\sim 10^6 M_{\odot}$, it is possible that the Wilkinson et al. (2001) observations of 300 $z \sim 1$ radio sources (not macrolensed) at ~ 1 mas resolution would be able to do better for $\sim 10^8 M_{\odot}$ UCMHs than the predicted limits we give in this paper.

4.3 Detecting standard CDM subhaloes

As expected, standard CDM subhaloes (assumed to have NFW density profiles) are not detectable using the observational scheme considered in this paper. In Fig. 6, we show examples of the $\sim 10^7$ and $\sim 10^8 M_{\odot}$ subhaloes close to the macroimages in our simulations at 22 GHz, assuming the Bullock et al. (2001) relation between mass and concentration parameter. In the standard case of $f_{\text{sub}} \approx 0.002$, only $M \lesssim 10^7 M_{\odot}$ subhaloes are sufficiently numerous to have a decent probability of showing up in the vicinity of the macroimages, and even though such objects may affect the overall magnification

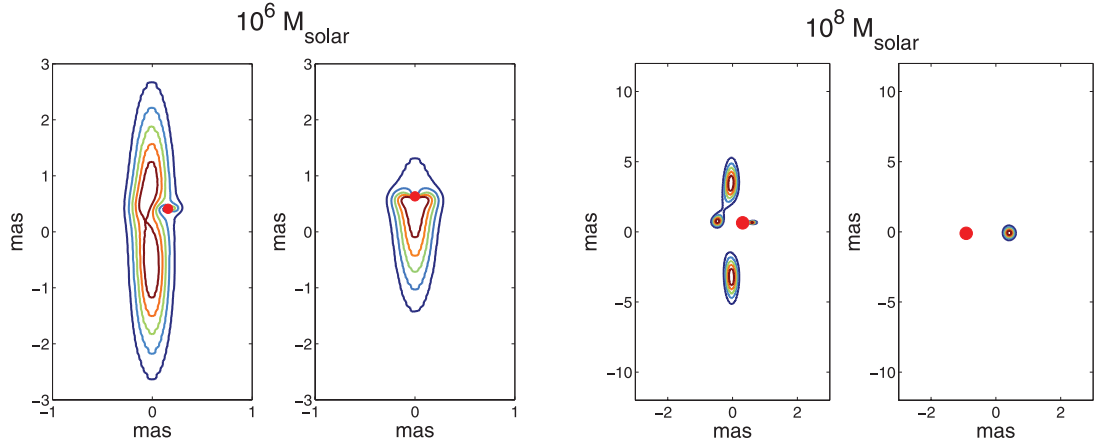


Figure 5. Examples of simulated radio maps of a macrolensed quasar jet at 86 GHz (source size 2×0.5 pc and resolution 0.05 mas), by UCMHs with $M_{\text{UCMH}} = 10^6$ and $10^8 M_{\odot}$ in the halo of the main lens. The probabilities of detecting such effects are, however, negligibly small unless the UCMH dark halo fraction is $f_{\text{UCMH}} \sim 0.2$.

Table 2. The lowest halo mass fraction in UCMHs, f_{UCMH} , that would produce detectable millilensing distortions with $P_{\text{milli}} \gtrsim 10$ per cent probability in a single macroimage pair.

Frequency (GHz)	Mass (M_{\odot})	Source size (pc)	min f_{UCMH}
86	10^6 – 10^8	2×0.5	2×10^{-1}
22	10^7 – 10^8	10×2.5	1×10^{-1}
8.4	10^8	40×10	5×10^{-2}

and the curvature of the jet (see left panel of Fig. 6), the associated small-scale distortion is too small to be resolved. NFW subhaloes at $\sim 10^8 M_{\odot}$ may in principle give rise to the detectable distortions (right panel of Fig. 6), but the probability of attaining the required alignment between macroimage and subhalo is negligibly small. We estimate that the probability of detecting small-scale distortions due to $10^8 M_{\odot}$ NFW subhaloes in a single macroimage pair is no more than $P_{\text{milli}} \approx 3 \times 10^{-4}$ in this case. At $10^9 M_{\odot}$, the probability is even lower ($P_{\text{milli}} \approx 4 \times 10^{-5}$).

Recent results by Vegetti et al. (2010b, 2012) hint at a higher surface mass density contribution ($f_{\text{sub}} \approx 0.03$) and a flatter subhalo

mass function ($\alpha = 1.1$ in equation (1)) than predicted by current CDM simulations, but even if we adopt these values, the probability for detection remains too low ($\approx 5 \times 10^{-4}$ for NFWs of mass 10^8 – $10^9 M_{\odot}$) to make this search strategy attractive.

The problem is one of source size – the macrolensed jets we consider cover an area in the lens plane that is several orders of magnitude too small to intersect such massive subhaloes. The intrinsic source size would need to have an area $\sim 10^3$ times greater than the largest jets we consider (40×10 pc at 8.4 GHz) to push the detection probabilities into the interesting range $P_{\text{milli}} \gtrsim 10$ per cent. This essentially requires a completely different kind of source, like the dusty sub-mm galaxies considered by Inoue & Chiba (2005a).

These results are admittedly sensitive to the concentration parameters adopted for the NFW subhaloes. In the examples above, we have used the $c(M_{\text{vir}})$ relation from Bullock et al. (2001), which for objects in the relevant mass range (10^7 – $10^8 M_{\odot}$) results in concentration parameters a factor of ≈ 2 higher than the ones predicted by the Macciò et al. (2008) relation. If we instead adopt the Macciò et al. (2008) $c(M_{\text{vir}})$ scaling, the detection threshold shifts upwards by an order of magnitude in mass, so that image distortions

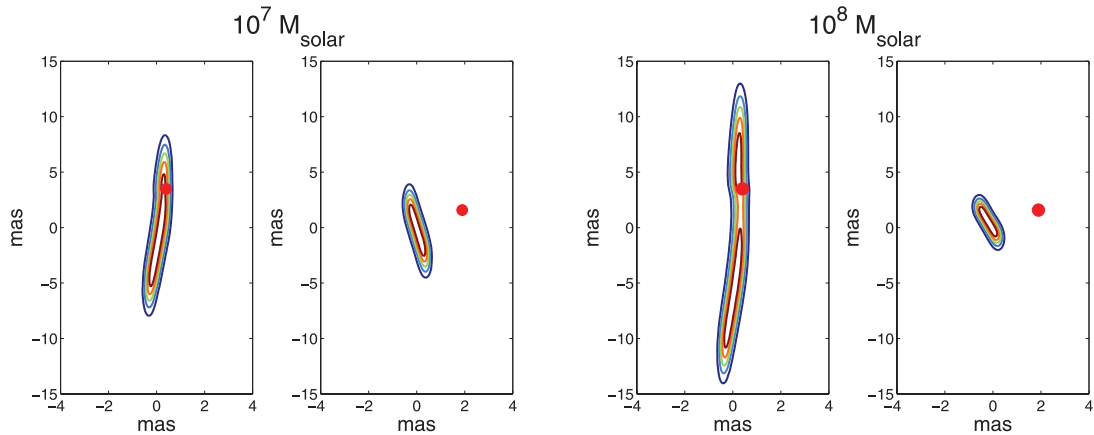


Figure 6. Examples of simulated radio maps of a macrolensed quasar jet at 22 GHz (source size 10×2.5 pc and resolution 0.3 mas), subject to millilensing distortions by NFW subhaloes with masses of either $\sim 10^7$ or $10^8 M_{\odot}$. The red dots mark the positions of the centres of these subhaloes. As the left pair of images shows, $\sim 10^7 M_{\odot}$ NFWs produce very mild distortions only, whereas NFW subhaloes of mass $\sim 10^8 M_{\odot}$ may produce more significant distortions if they are placed sufficiently close to a macroimage. The probability for such superpositions to occur is, however, very small.

predicted for 10^7 and $10^8 M_\odot$ NFW in the Bullock et al. case (Fig. 6) instead are produced at masses of $\sim 10^8$ and $\sim 10^9 M_\odot$.

5 DISCUSSION

5.1 Temporal effects

In previous sections, we have argued that millilensing-induced distortions of quasar jets may be distinguished from morphological features intrinsic to these sources, since the latter would be reproduced in all macroimages whereas millilensing should affect each image independently. However, this argument comes with a caveat. The time delay between the images in quasar-galaxy lenses can be up to a year (for a compilation of time delays, see Oguri 2007), which means that intrinsic, transient features in the jet may, at any given time, be visible in just one of the images and be mistaken for millilensing effects. This is, for instance, likely to be the case in superluminal radio jets, where blobs are seen to move ~ 1 mas yr^{-1} along the jet (e.g. Jorstad et al. 2001). For macrolensed jets that show signs of millilensing distortions, it may therefore become necessary to obtain data at two or more epochs. Since halo substructures give rise to millilensing magnification pattern that will appear stationary over decades (Metcalf & Madau 2001), any distortions that seem to move along the jet are bound to be intrinsic to the source. Small-scale features that are not duplicated in the other macroimages and appear with a fixed angular position (as, for instance, measured from the base of the jet) over the course of more than a year is on the other hand likely caused by millilensing.

5.2 Source size sensitivity

For a fixed substructure type and telescope beam size, the prospects of detecting millilensing effects depend on the adopted source dimensions. This is exemplified in Fig. 7, where the probability of substructures is seen to increase with source area – whereas only one IMBH is detectable in small-source case (left), two IMBHs are detectable for the larger source (right). The source sizes adopted in Section 3.2 are uncertain by a factor of a few, and it may be convenient to be able to generalize our results to match other source dimensions. For a given substructure type and mass, any detection limit $\min(f_{\text{sub},1})$ (as listed in Tables 1 and 2) derived for an intrinsically elliptical source with area A_1 can be rescaled to some other source area A_2 using:

$$\min f_{\text{sub},2} \approx \frac{A_1 + C_1 R_{\text{eff}}}{A_2 + C_2 R_{\text{eff}}} \min f_{\text{sub},1}. \quad (9)$$

Here, $\min f_{\text{sub},2}$ is the rescaled detection limit relevant for source area A_2 , whereas the C parameters represent the circumferences of the macroimages one wants to rescale from (C_1) and to (C_2). The impact parameter R_{eff} measures the projected distance from the subhalo centre within which detectable macroimage distortions will be produced. This impact parameter, which depends on both subhalo mass and type, is typically larger than the subhalo Einstein radius, since substantial deflection can occur even outside the latter. The R_{eff} values relevant for 10^3 – $10^6 M_\odot$ IMBHs and 10^6 – $10^8 M_\odot$ UCMHs are listed in Table 3 for the resolutions adopted at 8.4, 22 and 86 GHz. Since these R_{eff} values also depend on the magnification of the macroimage, R_{eff} values are presented for $\mu = 3, 10$ (our default value) and 30.

This rescaling scheme, which assumes that the source size and R_{eff} are independent, is admittedly an approximation and reliable only to within a factor of a few. Secondary images due to substructure

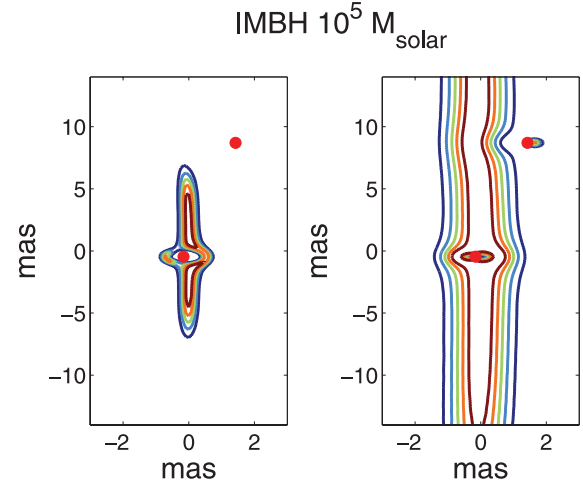


Figure 7. Illustration of how source size affects the probability for detecting dark halo substructure. The two frames depict a single macroimage (out of a two-image pair) with fixed macrolensing magnification ($\mu = 10$) but with different intrinsic source size: 10×2.5 pc (left) and 40×10 pc (right). The smaller version (left) corresponds to the source size adopted for our 22 GHz simulations (see Section 3.2). The red dots mark the positions of two $10^5 M_\odot$ IMBHs (identical positions in both frames). In the small-source case (left), only one of these IMBHs produce detectable millilensing effects, whereas both can be detected in the large-source case (right) due to better macroimage coverage of the lens plane. A resolution of 0.3 mas has been adopted in both cases (as considered suitable for 22 GHz observations).

lensing may, for instance, be easier to detect for a compact rather than an extended source due to flux-ratio issues. An effect of the latter type is evident in Table 3, where both 10^6 IMBHs and 10^8 UCMH are seen to have larger R_{eff} at 86 GHz (smallest source) than at 8.4 GHz (largest source).

5.3 The surface brightness profile

In previous sections, we have assumed the source to be an intrinsically straight jet with a surface brightness distribution described by a two-dimensional Gaussian. While the intrinsic source morphology and surface brightness profile are less important than the overall source area when assessing lensing probabilities, there are certain situations where they do matter. Since gravitational lensing conserves surface brightness, halo substructure can only produce detectable image distortions if it happens to affect a region of the macroimage where there is a non-negligible surface brightness gradient. In the extreme case of a source with constant surface brightness, halo substructure will not produce *any* detectable features unless its lensing effects extend beyond the macroimage boundary. This is exemplified in Fig. 8, where $10^5 M_\odot$ and $10^6 M_\odot$ IMBHs (red dots) are superposed on macroimages of (from left to right, for each IMBH mass) an elliptical source with constant surface brightness, an elliptical source with Gaussian surface brightness profile and a patchy jet with Gaussian ‘blobs’ of increasing size when moving from the lower-right to upper-left corner.

In this example, a $10^5 M_\odot$ IMBH becomes undetectable in the case of a constant surface brightness source, but can be spotted as a mild distortion against the Gaussian source. An IMBH of this mass redistributes surface brightness within an area that is much smaller than that of the source. Hence, if the source surface brightness is constant, no detectable effects are produced. Even though placed in exactly the same position, the lensing produced by a $10^6 M_\odot$ IMBH

Table 3. Impact parameter R_{eff} within which a subhalo of a given type will produce detectable macroimage distortions.

Type	Resolution (mas)	Mass (M_{\odot})	μ	R_{eff} (pc)
IMBH	0.05 (86 GHz)	10^3	3	1
		10^4		3
		10^5		7
		10^6		20
		10^3	10	2
		10^4		6
		10^5		20
		10^6		50
		10^3	30	2
		10^4		10
		10^5		40
		10^6		80
	0.3 (22 GHz)	10^4	3	2
		10^5		5
		10^6		20
		10^4	10	2
		10^5		7
		10^6		30
		10^4	30	2
		10^5		8
		10^6		40
	0.7 (8.4 GHz)	10^5	3	3
		10^6		10
		10^5	10	4
		10^6		20
		10^5	30	8
		10^6		40
UCMH	0.05 (86 GHz)	10^6	3	2
		10^7		6
		10^8		20
		10^6	10	3
		10^7		20
		10^8		60
		10^6	30	10
		10^7		30
		10^8		100
	0.3 (22 GHz)	10^7	3	2
		10^8		10
		10^7	10	4
		10^8		30
		10^7	30	5
		10^8		60
	0.7 (8.4 GHz)	10^8	3	10
		10^8	10	20
		10^8	30	60

on the other hand extends sufficiently far out to distort the rim of the macroimage and can therefore be detected regardless of the source profile. In fact, the only f_{IMBH} entry in Table 1 that would change in any dramatic way when going from a Gaussian to a constant surface brightness source corresponds to the $10^5 M_{\odot}$ case depicted in Fig. 8 (i.e. source size and resolution corresponding to 8.4 GHz). In this case, constant surface brightness source would effectively prevent any useful f_{IMBH} constraints, whereas the changes are modest in all other cases. Since UCMH lenses produce more long-range effects than IMBHs, the f_{UCMH} estimates in Table 2 are even less affected by the source surface brightness profile.

Fig. 8 also provides an example of a more patchy jet morphology. This jet has the same source area as the other source cases,

and consequently extends further in the vertical direction due to the empty regions between the ‘blobs’. Both $10^5 M_{\odot}$ and $10^6 M_{\odot}$ IMBHs are in principle detectable against the source in this example, although the distortion produced in the former case becomes very modest since the IMBH happens to be projected on the outskirts of one of the blobs. In general, having a complicated jet morphology does not significantly compromise the detectability of millilensing effects. Instead, a morphology of this type could even boost the detection prospects in cases where the substructure R_{eff} (see Section 5.2) is larger than empty regions in the macroimage (as in the $10^6 M_{\odot}$ IMBH case in Fig. 8), since the effective source area becomes larger in this situation.

5.4 The nature of the substructures

The detection of milliarcsecond or submilliarcsecond-scale image distortions would prove the existence of substructures within the macrolens, and also allows constraints on their surface number densities (as a function of substructure mass and type) to be set. However, the exact nature of a single millilens may still be very difficult to determine, since a low-mass, high-density substructure can produce a distortion very similar to that of a high-mass, low-density object. While Inoue & Chiba (2005b) have demonstrated that the distortions induced in extended images (like the ones we model here) contain some information about the density profiles of the lenses, the finite resolution and sensitivity of actual observations could still allow for considerable degeneracies in cases where neither the masses nor the density profiles of the millilenses are known. IMBHs and UCMHs can, for instance, produce very similar lensing distortions in our simulations (although at different masses – a UCMH typically needs to be a factor of $\sim 10^3$ more massive than an IMBH to reproduce a given feature). While it is possible that a combined consideration of small-scale distortions (e.g. the bending of a macrolensed jets), astrometric perturbations (the positional shift of a macroimage produced by the presence of substructures) and macroimage flux ratios could provide some constraints, this is beyond the scope of the present paper.

6 SUMMARY

Using simulations of strongly lensed quasar jets, we argue that very dense forms of halo substructure (IMBHs and UCMHs) within the main lens may reveal itself through small-scale morphological distortions in the macroimages. Such distortions can be distinguished from intrinsic source features by obtaining data at multiple epochs. By mapping a handful of macrolensed jet systems at submilliarcsecond resolution, we argue that $\sim 10^3$ – $10^6 M_{\odot}$ IMBHs can be detected or ruled out if they contribute a surface mass fraction of $f_{\text{IMBH}} \gtrsim 0.01$ (depending on the VLBI array and frequency used) to the dark matter of the main lens at the macroimage positions. UCMHs in the $\sim 10^6$ – $10^8 M_{\odot}$ mass range may similarly produce detectable small-scale effects if such objects comprise $f_{\text{UCMH}} \gtrsim 0.1$ of the dark matter. While standard CDM subhaloes at masses of $\gtrsim 10^8 M_{\odot}$ can, in principle, also produce milliarcsecond-scale distortions, provided that such objects are projected sufficiently close to the macroimages, the probability of this is too small ($P_{\text{milli}} \sim 10^{-4}$) for sources of the type we consider.

ACKNOWLEDGEMENTS

EZ acknowledges funding from the Swedish Research Council and the Swedish National Space Board. PS is supported by the Lorne

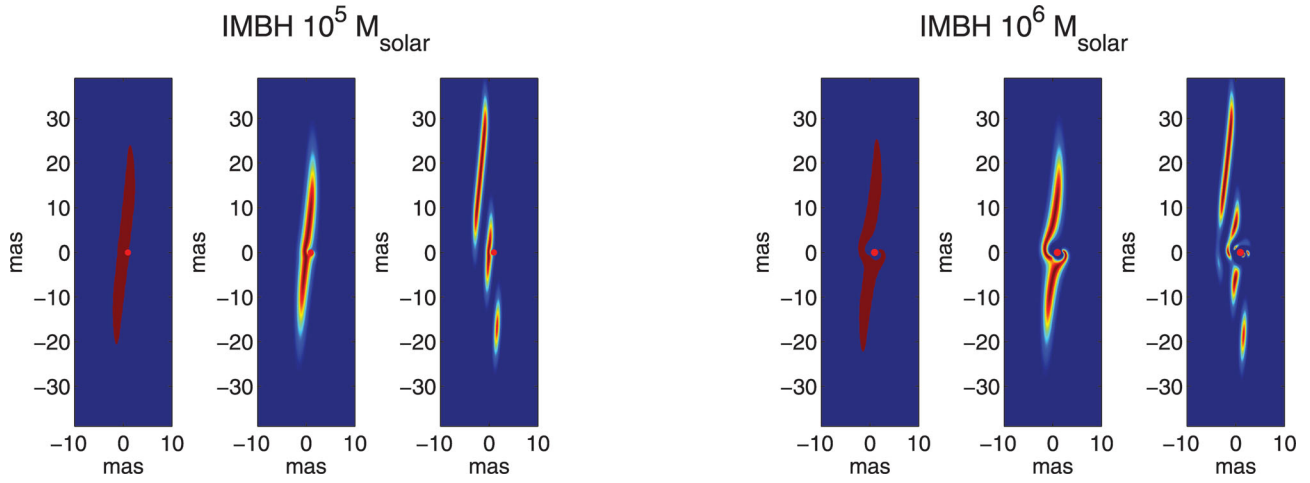


Figure 8. Examples of how source morphology and surface brightness distribution affect the detectability of millilensing from IMBHs of mass $10^5 M_\odot$ and $10^6 M_\odot$ against a simulated radio map of a strongly lensed quasar jets at 8.4 GHz. For each IMBH mass, the leftmost frame contains a source with constant surface brightness, the middle one the Gaussian profile used throughout the rest of the paper, and the rightmost frame a source consisting of a sequence of Gaussian ‘blobs’ of different sizes. Contour representations are not used in this plot, since this becomes confusing in the case of a flat surface brightness profile. In general, complicated source morphologies (rightmost frames) do not significantly compromise the detectability of millilensing effects, but sources with shallow (or even constant) surface brightness profiles may render certain forms of substructure lenses undetectable (as seen in the case where $10^5 M_\odot$ IMBH are superposed on a constant surface brightness source).

Trottier Chair in Astrophysics, and institute for Particle Physics Theory Fellowship and a Banting Fellowship, administered by the Natural Science and Engineering Research Council of Canada.

REFERENCES

- Bate N. F., Floyd D. J. E., Webster R. L., Wyithe J. S. B., 2011, *ApJ*, 731, 71
- Begelman M. C., Volonteri M., Rees M. J., 2006, *MNRAS*, 370, 289
- Belikov A. V., Buckley M. R., Hooper D., 2012, *Phys. Rev. D*, 86, 043504
- Berezinsky V., Dokuchaev V., Eroshenko Y., 2003, *Phys. Rev. D*, 68, 103003
- Berezinsky V., Dokuchaev V., Eroshenko Y., 2006, *Phys. Rev. D*, 73, 063504
- Berezinsky V., Dokuchaev V., Eroshenko Y., 2007, *J. Cosmol. Astropart. Phys.*, 0707, 011
- Berezinsky V., Dokuchaev V., Eroshenko Y., 2008, *Phys. Rev. D*, 77, 083519
- Berezinsky V., Dokuchaev V., Eroshenko Y., Kachelriess M., Solberg M. A., 2010a, *Phys. Rev. D*, 81, 103529
- Berezinsky V., Dokuchaev V., Eroshenko Y., Kachelriess M., Solberg M. A., 2010b, *Phys. Rev. D*, 81, 103530
- Biggs A. D., Browne I. W. A., Jackson N. J., York T., Norbury M. A., McKean J. P., Phillips P. M., 2004, *MNRAS*, 350, 949
- Bringmann T., 2009, *New J. Phys.*, 11, 105027
- Bringmann T., Scott P., Akrami Y., 2012a, *Phys. Rev. D*, 85, 15027
- Bringmann T., Huang X., Ibarra A., Vogl S., Weniger C., 2012b, *J. Cosmol. Astropart. Phys.*, 07, 054
- Bullock J. S., Kolatt T. S., Sigal y., Somerville R. S., Kravtsov A. V., Klypin A. A., Primack J. R., Dekel A., 2001, *MNRAS*, 321, 559
- Carr B. J., Sakellariadou M., 1999, *ApJ*, 516, 195
- Carr B. J., Kohri K., Sendouda Y., Yokoyama J., 2010, *Phys. Rev. D*, 81, 104019
- Chen J., Koushiappas S. M., Zentner A. R., 2011, *ApJ*, 741, 117
- Chiba M., 2002, *ApJ*, 565, 17
- Davies M. B., Miller M. C., Bellovary J. M., 2011, *ApJ*, 740, L42
- Devecchi B., Volonteri M., 2009, *ApJ*, 694, 302
- Feng H., Soria R., 2011, *New Astron. Rev.*, 55, 166
- Font A. S. et al., 2011, *MNRAS*, 417, 1260
- Frampton P. H., Kawasaki M., Takahashi F., Yanagida T. T., 2010, *J. Cosmol. Astropart. Phys.*, 04, 023
- Gao L., Frenk C. S., Boylan-Kolchin M., Jenkins A., Springel V., White S. D. M., 2011, *MNRAS*, 410, 2309
- Garrett M. A., Calder R. J., Porcas R. W., King L. J., Walsh D., Wilkinson P. N., 1994, *MNRAS*, 270, 457
- Geha M., Willman B., Simon J. D., Strigari L. E., Kirby E. N., Law D. R., Strader J., 2009, *ApJ*, 692, 1464
- Hayashi E., Navarro J. F., Taylor J. E., Stadel J., Quinn T., 2003, *ApJ*, 584, 541
- Hezaveh Y., Dalal N., Holder G., Kuhlen M., Marrone D., Murray N., Vieira J., 2012, preprint (arXiv:1210.4562)
- Hisano J., Inoue K. T., Takahashi T., 2006, *Phys. Lett. B*, 643, 141
- Hooper D., Linden T., 2012, *Phys. Rev. D*, 86, 083532
- Hooper D., Kaplinghat M., Strigari L. E., Zurek K. M., 2007, *Phys. Rev. D*, 76, 103515
- Inoue K. T., Chiba M., 2003, *ApJ*, 591, L83
- Inoue K. T., Chiba M., 2005a, *ApJ*, 633, 23
- Inoue K. T., Chiba M., 2005b, *ApJ*, 634, 77
- Islam R. R., Taylor J. E., Silk J., 2004, *MNRAS*, 354, 427
- Jorstad S. G., Marscher A. P., Mattox J. R., Aller M. F., Aller H. D., Wehrle A. E., Bloom S. D., 2001, *ApJ*, 556, 738
- Josan A. S., Green A. M., 2010, *Phys. Rev. D*, 82, 083527
- Kassiola A., Kovner I., Blandford R. D., 1991, *ApJ*, 381, 6
- Kawaguchi T., Kawasaki M., Takayama T., Yamaguchi M., Yokoyama J., 2008, *MNRAS*, 388, 1426
- Kazantzidis S., Mayer L., Mastropietro C., Diemand J., Stadel J., Moore B., 2004, *ApJ*, 608, 663
- Keeton C. R., Gaudi B. S., Petters A. O., 2003, *ApJ*, 598, 138
- King L. J., Browne I. W. A., Muxlow T. W. B., Narasimha D., Patnaik A. R., Porcas R. W., Wilkinson P. N., 1997, *MNRAS*, 289, 450
- Klypin A., Kravtsov A. V., Valenzuela O., Prada F., 1999, *ApJ*, 522, 82
- Kochanek C. S., Dalal N., 2004, *ApJ*, 610, 69
- Lacki B. C., Beacom J. F., 2010, *ApJ*, 720, L67
- Li F., Erickcek A. L., Law N. M., 2012, *Phys. Rev. D*, 86, 043519
- Lister M. L. et al., 2009, *AJ*, 137, 3718
- Macciò A. V., Miranda M., 2006, *MNRAS*, 368, 599
- Macciò A. V., Dutton A. A., van den Bosch F. C., 2008, *MNRAS*, 391, 1940
- Macciò A. V., Kang X., Fontanot F., Somerville R. S., Koposov, S., Monaco P., 2010, *MNRAS*, 402, 1995
- Maciejewski M., Vogelsberger M., White S. D. M., Springel V., 2011, *MNRAS*, 415, 2475
- Mack K. J., Ostriker J. P., Ricotti M., 2007, *ApJ*, 665, 1277
- Madau P., Rees M. J., 2001, *ApJ*, 551, L27
- Mao S., Schneider P., 1998, *MNRAS*, 295, 587

- Metcalf R. B., 2002, *ApJ*, 580, 696
- Metcalf R. B., Amara A., 2012, *MNRAS*, 419, 3414
- Metcalf R. B., Madau P., 2001, *ApJ*, 563, 9
- Micic M., Holley-Bockelmann K., Sigurdsson S., 2011, *MNRAS*, 414, 1127
- Moore B., Ghigna S., Governato F., Lake G., Quinn T., Stadel J., Tozzi P., 1999, *ApJ*, 524, L19
- Navarro J. F., Frenk C. S., White S. D. M., 1996, *ApJ*, 462, 563 (NFW)
- Navarro J. F. et al., 2010, *MNRAS*, 402, 21
- Noyola E., Gebhardt K., Kissler-Patig M., Lutzgendorf N., Jalali B., de Zeeuw P. T., Baumgardt H., 2010, *ApJ*, 719, L60
- Oguri M., 2007, *ApJ*, 660, 1
- Ohashi S., Chiba M., Inoue K. T., 2009, in Hagiwara Y., Fomalont E., Tsuboi M., Murata Y., eds, *ASP Conf. Ser. Vol. 402, Approaching Micro-Arcsecond Resolution with VSOP-2: Astrophysics and Technologies*. Astron. Soc. Pac., San Francisco, p. 290
- Pooley D., Rappaport S., Blackburne J. A., Schechter P. L., Wambsganss J., 2012, *ApJ*, 744, 111
- Ricotti M., Gould A., 2009, *ApJ*, 707, 979
- Ricotti M., Ostriker J. P., Mack K. J., 2008, *ApJ*, 680, 829
- Riehm T., Zackrisson E., Mörtzell E., Wiik K., 2009, *ApJ*, 700, 1552
- Ros E., Guirado J. C., Marcaide J. M., Pérez-Torres M. A., Falco E. E., Muñoz J. A., Alberdi A., Lara L., 2000, *A&A*, 362, 845
- Rusin D., Norbury M., Biggs A. D., Marlow D. R., Jackson N. J., Browne I. W. A., Wilkinson P. N., Myers S. T., 2002, *MNRAS*, 330, 205
- Rusin D., Kochanek C. S., Keeton C. R., 2003, *ApJ*, 595, 29
- Saito R., Yokoyama J., 2010, *Prog. Theor. Phys.*, 123, 867
- Sandick P., Diemand J., Freese K., Spolyar D., 2011, *J. Cosmol. Astropart. Phys.*, 01, 018
- Scott P., Siverthsson S., 2009, *Phys. Rev. Lett.*, 103, 1301
- Shandera S., Erickcek A., Scott P., Galarza J. Y., 2012, *J. Cosmol. Astropart. Phys.*, preprint (arXiv:1211.7361)
- Springel V. et al., 2008, *MNRAS*, 391, 1685
- Su M., Finkbeiner D. P., 2012, preprint (arXiv:1207.7060)
- Torniainen I. et al., 2008, *A&A*, 482, 483
- Totani T., 2010, *PASJ*, 62, L1
- Vale A., Ostriker J. P., 2006, *MNRAS*, 371, 1173
- van den Aarssen L. G., Bringmann T., Pfrommer C., 2012, *Phys. Rev. Lett.*, 109, 1301
- van Wassenhove S., Volonteri M., Walker M. G., Gair J. R., 2010, *MNRAS*, 408, 1139
- Vegetti S., Koopmans L. V. E., 2009a, *MNRAS*, 392, 945
- Vegetti S., Koopmans L. V. E., 2009b, *MNRAS*, 400, 1583
- Vegetti S., Czoske O., Koopmans L. V. E., 2010a, *MNRAS*, 407, 225
- Vegetti S., Koopmans L. V. E., Bolton A., Treu T., Gavazzi R., 2010b, *MNRAS*, 408, 1969
- Vegetti S., Lagattuta D. J., McKean J. P., Auger M. W., Fassnacht C. D., Koopmans L. V. E., 2012, *Nat*, 481, 341
- Vesperini E., McMillan S. L. W., D'Ercole A., D'Antona F., 2010, *ApJ*, 713, L41
- Wambsganss J., Paczynski B., 1992, *ApJ*, 397, L1
- Webb N. et al., 2012, *Sci*, 337, 554
- Wilkinson P. N. et al., 2001, *Phys. Rev. Lett.*, 86, 584
- Xu D. D. et al., 2009, *MNRAS*, 398, 1235
- Xu D. D., Mao S., Cooper A. P., Wang J., Gao L., Frenk C. S., Springel V., 2010, *MNRAS*, 408, 1721
- Xu D. D., Mao S., Cooper A. P., Gao L., Frenk C. S., Angulo R. E., Helly J., 2012, *MNRAS* 421, 2553
- Yang Y., Huang X., Chen X., Zong H., 2011a, *Phys. Rev. D*, 84, 43506
- Yang Y., Feng L., Huang X., Chen X., Lu T., Zong H., 2011b, *J. Cosmol. Astropart. Phys.*, 12, 020
- Yang Y., Yang G., Zong H., 2012, preprint (arXiv:1210.1409)
- Yonehara A., Umemura M., Susa H., 2003, *PASJ*, 55, 1059
- York T. et al., 2005, *MNRAS*, 361, 259
- Zackrisson E., Riehm T., 2010, *Adv. Astron.*, 478910, preprint (arXiv:0905.4075)
- Zackrisson E., Riehm T., Möller O., Wiik K., Nurmi P., 2008, *ApJ*, 684, 804
- Zechlin H.-S., Fernandes M. V., Elsässer D., Horns D., 2012, *A&A*, 538, 93
- Zhang D., 2011, *MNRAS*, 418, 1850

This paper has been typeset from a \LaTeX file prepared by the author.

Paper II

Probing cold dark matter subhalos with simulated ALMA observations of macrolensed sub-mm galaxies

Saghar Asadi,¹★ Erik Zackrisson,² Emily Freeland¹

¹*Department of Astronomy, Stockholm University, Oscar Klein Center, AlbaNova, Stockholm SE-106 91, Sweden*

²*Department of Physics and Astronomy, Uppsala University, Box 515, SE-751 20 Uppsala, Sweden*

Accepted XXX. Received YYY; in original form ZZZ

ABSTRACT

If the dark matter halos of galaxies contain large numbers of subhalos as predicted by the Λ CDM model, these subhalos are expected to appear in strong galaxy–galaxy lens systems as small-scale perturbations in individual images. We simulate observations of multiply-lensed sub-mm galaxies at $z \sim 2$ as a probe of the dark matter halo of a lens galaxy at $z \sim 0.5$. We present detection limits for dark substructures based on a visibility plane analysis of simulated ALMA data in bands 7, 8 and 9. This method benefits from the use of complex visibilities to put emphasis on different angular scales via the choice of the weighting scheme. We explore two effects: a local surface brightness deflection on angular scales similar to the Einstein radius and the astrometric shift of the image. This improves the sensitivity of our lens modeling to the mass of the lens perturber. We stress that this technique is more sensitive to detection of low-mass subhalos compared to other techniques which use image plane modeling. We demonstrate that pseudo-Jaffe subhalos can be detected with 99% confidence down to masses of $\approx 3 \times 10^7 M_\odot$ in ALMA band 7, $\approx 5 \times 10^7 M_\odot$ in band 8 and $\approx 8 \times 10^7 M_\odot$ in band 9. However, the mass and the shape parameter of Einasto subhalos remain highly degenerate.

Key words: techniques: interferometric – gravitational lensing: strong – galaxies: dwarf – radio continuum: galaxies – submillimetre: galaxies – dark matter

1 INTRODUCTION

Cosmological N-body simulations predict the existence of dark matter halos in the mass range from galaxy cluster halos ($\sim 10^{15} M_\odot$) down to the smallest halos corresponding to the cutoff in the primordial matter power spectrum. The high-mass end of the halo mass function can be tested through anisotropies in the cosmic microwave background radiation (e.g. Wright et al. 1992; Bennett et al. 2013; Planck Collaboration et al. 2014), and the low-mass end is highly dependent on the detailed properties of dark matter particles; particularly particle mass and decoupling velocity (e.g. Bertone, Hooper, & Silk 2005). The cutoff mass constraint varies widely from one particle candidate to another. WIMP models usually suggest a minimum halo mass as low as $\sim 10^{-11} M_\odot$ for light dark matter particles (e.g. Bringmann 2009; Cornell, Profumo, & Shepherd 2013).

Dark matter-only cosmological N-body simulations assume the gravitational interaction between WIMPs to be the dominant driving force of structure formation (see for instance Springel et al. 2008; Gao et al. 2012; Schaller et al.

2015, for projects Aquarius, Phoenix, and EAGLE, respectively). As a result, dark matter halos that host galaxies form in a hierarchical process during which small halos that are bound to the gravitational potential of a massive halo join the smooth matter content of the parent halo through tidal disruption. This gradual process takes up to several billion years to complete. During this hierarchical assembly, smaller halos tend to stay present within the parent halo in the form of a clumpy substructure on top of the smooth matter distribution. A generic prediction of dark matter-only simulations is that $\sim 10\%$ of the total halo mass of a galaxy at $z = 0$ is in the form of a clumpy structure bound to the smooth halo (Gao et al. 2008; Maciejewski et al. 2011). These subhalos of simulated galaxy-sized CDM halos are best-fitted by a mass function of the type:

$$\frac{dN}{dM} \propto M^{-\alpha}$$

with $\alpha \approx 1.9$ (Springel et al. 2008; Gao et al. 2008, 2012; Xu et al. 2012) at the low-mass end, resulting in simulated dark halos that greatly outnumber the dwarf satellites of Milky Way and Andromeda (see e.g. Klypin et al. 1999; Moore et al. 1999).

★ E-mail: saghar.asadi@astro.su.se (SA)

A recent challenge for Λ CDM at small-scales is the mismatch between the most massive subhalos at $z = 0$ in simulations and the most massive satellite galaxies in the local group, the so-called “too big to fail” problem (Boylan-Kolchin, Bullock, & Kaplinghat 2011, 2012). In the absence of full hydrodynamic cosmological simulations, adopting baryonic physics and feedback processes in simulations on galaxy/group scales seems to be able to regulate both the local group dwarf population with respect to that of dark matter halos and the correspondence between the most massive halos and satellites (e.g. Garrison-Kimmel et al. 2014; Sawala et al. 2014; Fry et al. 2015; Schaller et al. 2015). Adopting non-standard properties for dark matter particles also provides a competitive, and maybe complimentary, solution to both these discrepancies (e.g. Lovell et al. 2012; Vogelsberger, Zavala, & Loeb 2012; Wang et al. 2014).

Simulated dark matter halos generally fit to a universal 3D density profile increasing towards the center as $\rho \propto r^{-\alpha}$, $\alpha = 1$ (shallower than an isothermal sphere with $\alpha = 2$), while the logarithmic slope decreases at larger radii, i.e. $\alpha = 3$ for $r > r_s$ (Navarro, Frenk, & White 1996). Observationally, dwarf and low surface brightness galaxies show flat dark matter mass density profiles in the center, i.e. $\alpha = 0$ (e.g. Moore 1994; Zackrisson et al. 2006; Kuzio de Naray 2008; Oh et al. 2011; Kuzio de Naray & Spekkens 2011; de Blok 2010; Walker & Peñarrubia 2011; Amorisco & Evans 2012). Baryonic feedback processes may be responsible for the “cored” central density profiles in baryon-dominated regions (see e.g. Navarro, Eke, & Frenk 1996; de Blok et al. 2001; Maxwell, Wadsley, & Couchman 2015). However, dark matter-dominated halos seem to be following a nearly universal density profile which is much “cuspiest” in the center.

Gravitational lensing as a probe of dark halo substructures places constraints on the low-mass end of the dark matter halo mass function (for a review see Zackrisson & Riehm 2010) at $z > 0$. Even though the surface brightness is conserved in gravitational lensing, the angular size and integrated flux of the lensed object are magnified. This can be used as a tool for resolving high-redshift background objects such as sub-mm galaxies (Hezaveh et al. 2013).

The strong lensing effect requires a close alignment of the source, the lens, and the observer to result in multiple lensed images of the background source. The total mass content of the foreground lens, including both the underlying smooth dark matter halo and the substructure, is probed by studying locations and relative fluxes of these macroimages. Observations have attempted to constrain the contribution from dark matter substructure using two techniques: the statistical examination of flux ratio anomalies and compound lensing of single perturbers.

While simple, smooth models of lens galaxies are usually able to reproduce the positions of the macroimages, their observed flux ratios are more difficult to understand. These flux-ratio anomalies have been interpreted as evidence of substantial small-scale structure within the main lens (e.g. Chiba 2002; Keeton 2003; Kochanek & Dalal 2004; Cyr-Racine et al. 2015). They provide statistical constraints on the mass fraction of galactic halos in the form of substructure and possibly the mass function of the subhalos. Inferred values of the projected subhalo mass fraction vary between

$f_{\text{sub}} \approx 0.002$ (Xu et al. 2009) from flux ratio anomalies, to $f_{\text{sub}} \approx 0.006$ (Vegetti et al. 2014) based on gravitational detection of single high-mass subhalos. However, CDM substructure is unlikely to be the only cause of these flux ratio anomalies which implies that this fraction could be considered as an upper limit (see e.g. Xu et al. 2015, for investigating two classes of such contributions; interstellar propagation effects and the use of improper models for the main lens that are either too simple or unrealistic).

The compound lensing technique, on the other hand, is not only able to detect individual subhalos but also to constrain the mass and details of the internal density profile of the subhalo aligned as a perturber in the strong galaxy-galaxy lensing system and consequently different dark matter models. The inferred CDM fraction from strong lensing made by single perturbers indicates a higher fraction (mean projected substructure mass fraction $f = 0.0064$ to $f = 0.0076$ depending on the prior assumptions) of substructure contribution in the surface mass density of a galactic halo (Vegetti et al. 2012, 2014). While methods based on surface brightness perturbation are significantly less sensitive to low-mass halos, flux ratio anomalies are produced by the combination of both low- and high-mass subhalos and due to the exponential decrease of subhalo numbers with increasing mass, massive subhalo alignment becomes increasingly more rare. Therefore, flux ratio anomaly method probes subhalos with $M_{\text{sub}} \sim 10^5 M_{\odot}$, while direct lens perturbers accounted for in Vegetti et al. (2014) are much more massive $M_{\text{sub}} \sim 10^8 - 10^9 M_{\odot}$.

In the next section, we will discuss the two different groups of empirical halo density profiles. Section 3, elaborates on the details of our simulations, including the choices of sources and perturbers and the use of complex visibilities, in comparison to image plane modeling. Our results are presented in section 4, and finally section 5 discusses the results of this work in the context of the field as well as the limitations. A summary of the results can be found in section 6

2 DIFFERENT FORMS OF HALO SUBSTRUCTURE

The central slope of the density profiles of dark matter halos can be measured both from observational data and fits to halos in N-body simulations. In this regard, the single-parameter (cored) singular isothermal sphere (ellipsoid) profile provides an acceptable lens model for the mean dark matter halo of galaxies. On the other hand, the universal density profiles of field halos in CDM simulations can be reasonably well described by Navarro, Frenk, & White (1996, hereafter NFW) profile:

$$\rho(r) = \frac{\rho_s}{(r/r_s)(1+r/r_s)^2}$$

where r_s is the characteristic scale radius of the halo, i.e. the radius at which $\rho \propto 1/r^2$, and ρ_s is the density at $r = r_s$. An extra parameter called the *concentration parameter* c relates the scale density of the halo to its virial radius and is defined as $c \equiv r_s/r_{\text{vir}}$. The concentration parameter therefore, contains information about the formation and evolution of the halo and depends on the time of

the collapse of the halo as well as its virial mass. Given the hierarchical formation of halos, the low-mass halos were formed at higher redshift where the mean density of the Universe was higher and so was the inner density of collapsed halos. This results in a weak $c - M_{\text{vir}}$ correlation such that the concentration parameter decreases with increasing M_{vir} . Besides, low-mass subhalos gradually lose mass in tidal interaction with the parent halo which leads to a further increase of their c_{vir} over time (Bullock et al. 2001; Macciò, Dutton, & van den Bosch 2008).

Relaxing the central logarithmic slope $\gamma = \frac{d \ln(\rho/\rho_s)}{d \ln(r/r_s)}$ in the basic two-parameter form of NFW profile makes better fit to individual halos in CDM simulations. In this three-parameter form, the inner cusp slope becomes progressively shallower towards the center, eventually reaching inner slope of $\gamma \geq -1$. The generalized NFW profile (gNFW) is formulated as:

$$\rho(r) = \frac{\rho_s}{(r/r_s)^\gamma (1 + r/r_s)^{3-\gamma}}$$

where $\gamma = 1$ gives the traditional NFW profile and $\gamma = 2$ is equivalent to a singular isothermal sphere (SIS). Another option for a three-parameter profile is the Einasto profile, inspired by the two-dimensional Sersic surface brightness profile of elliptical galaxies. Both high-resolution measurements of central stellar and gas content of low surface brightness dwarf galaxies, and high-resolution CDM simulations, tend to indicate more consistency with a three-parameter density profile rather than the traditional NFW ones. There are various studies suggesting that simulated CDM halos are better described by a three-parameter model such as the Einasto profile than the standard NFW (e.g. Navarro et al. 2004; Gao et al. 2008; Di Cintio et al. 2014; Dutton & Macciò 2014). The extra parameter describing dark halo density profiles, α_{Ein} , gives the density profile more flexibility in shape, i.e. $\gamma(r) = -d \ln \rho / d \ln r$. The three-dimensional Einasto profile takes the form:

$$\ln \left(\frac{\rho(r)}{\rho_s} \right) = -b \left[\left(\frac{r}{r_s} \right)^{\frac{1}{n}} - 1 \right]$$

where the *Einasto index* $\alpha_{\text{Ein}} = \frac{1}{n}$, and therefore the logarithmic slope becomes $\gamma = -\frac{b}{n} \left(\frac{r}{r_s} \right)^{\frac{1}{n}}$. Best-fit density profiles to simulated dark matter halos of a variety of masses in the Aquarius project show inner slopes shallower than the original NFW (Navarro et al. 2010). These halos are not self-similar, i.e. Einasto index changes with halo mass. Navarro et al. (2004) find the Einasto index for halos in the mass range between dwarves and clusters to be 0.12–0.22, with an average value of 0.17. According to Hayashi & White (2008); Gao et al. (2008), α_{Ein} tends to increase with mass and redshift in halos of the Millennium simulation. From the gravitational lensing point of view, Einasto profiles are more demanding to work with as one cannot derive an analytical surface mass density as a function of α_{Ein} . Hence the lens equation needs to be solved numerically for each case.

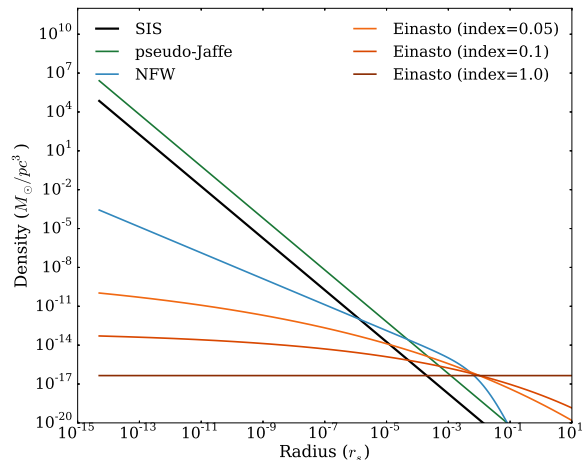


Figure 1. Four different inner density profiles of dark matter halos; Singular isothermal sphere (SIS) shown in black, the pseudo-Jaffe profile in green, the standard CDM halo profile suggested by NFW in blue, and the three-parameter Einasto profile with different Einasto indices in shades of brown. All profiles are normalized to the virial subhalo mass $M_{\text{vir}} = 10^8 M_\odot$, and the Bullock et al. (2001) recipe is adopted to set the concentration parameter c_{vir} at $z = 0.5$. A range of about two decades in Einasto indices show that investigating α_{Ein} in a range between $10^{-2} - 10^{-1}$ is in principle relevant in the context of gravitational lensing. Note must be taken that the Einasto index depends systematically on mass, meaning that the term “universal” density profile needs to be used having that in mind that density profiles of halos with various masses are not self-similar.

3 METHOD

The Einstein radii of lens perturbors with $\rho(r) \propto r^{-2}$ (SIS or pseudo-Jaffe profiles) and virial masses corresponding to the dark matter substructure mass range $M_{\text{vir}} < 10^{10} M_\odot$ is over an order of magnitude too small to be directly detectable even with milliarcsecond resolution (see Figure 1 in Riehm et al. 2008). However, as a result of the shear made by the lens perturber, corresponding surface brightness perturbations appear at a range of angular scales larger than R_E .

The lensing simulations we present here employ Glafic, a grid-based software which solves the gravitational lensing equation employing several lens and source models (Oguri, Inoue, & Minowa 2010). A high-resolution source surface brightness model based on generic properties of submm galaxies (see section 3.1) goes into the lensing code, where various lens systems – as discussed in section 4 – are tested for a single source model. The simulated image of the lensed SMG is then fed into the CASA simulator as the sky model where expected visibility measurements of ALMA are calculated based on observational settings as detailed in 3.2. The background cosmology throughout the work is a flat Λ CDM model where $\Omega_m = 0.27$, and $H_0 = 100h \text{ km s}^{-1} \text{ Mpc}^{-1}$ and $h = 0.7$.

The raw visibilities from CASA are then weighted, once to optimize the resulting angular resolution -in cost of sensitivity- and once for the most sensitivity, sacrificing the angular resolution. When comparing simulated observations with models, the χ^2 is simultaneously minimized for

the two weighting schemes. Therefore, the best-fit model is only achieved when the simulated data fits the model in both short- and long-spacings, i.e. large and small angular scales respectively. When the focus is on the subhalo mass resolution (section 4.1), our emphasis is on steep inner density profiles (singular isothermal spheres (SIS) and pseudo-Jaffe profiles). In cases where we focus on the inner density profiles of the substructure (section 4.2), the shallower density profile models (NFW and Einasto) are considered. This is due to the poor detection prospects for standard subhalos of the relevant mass range with this technique (see figure 4).

One interesting question to answer is, what is the minimum mass for a lens perturber (of any inner density profile) to be detectable from a smooth lens. This question addresses the mere presence of dark subhalos within the main halo. The mass detection limit for SIS and pseudo-Jaffe profiles gives a comparison between the results of this method and others. However, unlike these compact density profiles, CDM halo substructures are better represented by the three-parameter profiles, NFW, and Einasto. Without a handle on both mass and density profile of the detected subhalo, neither of the physical parameters related to the CDM model – subhalo mass function slope and the fraction of mass within a galaxy-sized halo in the form of dark substructures – are addressed. While detecting the gravitational lensing effect of a subhalo within the main halo is relatively straightforward, deriving the physical mass from gravitational lensing observations is not (see section 5 for a more detailed discussion). Therefore, in case of CDM subhalo density profiles, we investigate the degeneracy between the mass and the shape parameter α_{Ein} .

3.1 Strongly-lensed sources

There are a few criteria to fulfill when searching for strongly-lensed targets suitable for millilensing by halo substructures. One is the achievable angular resolution and the other the covered area in the lens plane probing the potential substructures of the lens. Optimizing the combination of the two leads to different combinations of source and observing frequency which are limited by the instrumental capabilities. A previous work by Zackrisson et al. (2013) investigates the prospects of halo substructure detection using synchrotron emission by blazars observable at high angular resolutions by various VLBI arrays at frequencies between 8.4 – 86 GHz. However, the synchrotron radiation from blazars is emitted within compact regions much smaller than a parsec, while a star-forming galaxy emits thermal dust continuum across a physical region a few orders of magnitude more extended. As concluded in Zackrisson et al. (2013), in addition to very high angular resolution observations for both standard CDM halos and compact alternative substructures, larger covering of the lens plane is needed to boost the probability of suitable lens-source alignment to sample even the massive end of the subhalo mass function. This work employs simulations of continuum emission from multiply-lensed sub-mm galaxies (SMGs) to investigate the prospects of detecting and constraining the inner density slope of dark halo substructures. Sub-millimeter galaxies have a redshift distribution which peaks at $z \approx 2$ (Wardlow et al. 2013) and typical flux densities of $S_{850} \geq 5$ mJy (Karim et al. 2013). The study of lensed SMGs with angular resolution of the order ~ 0.1 mas

can provide spatial resolutions of a few 100 pc in the source plane, at $z \sim 2$, which in turn corresponds to a spatial resolution of a few $\times 10$ pc in the lens plane at $z \sim 0.5$. This is sufficient to probe dwarf galaxies and dark substructure of the galactic halo. The percentage of SMGs expected to be strongly-lensed with an average magnification factor of $\mu \sim 9$ is 32–74% (for $S_{500\mu\text{m}} \geq 100$ mJy) and 15–40% (for $S_{500\mu\text{m}}$ between 80–100 mJy) (Wardlow et al. 2013).

Blain et al. (1999) compare the unlensed SMG number counts at 450 and 850 μm – roughly corresponding to ALMA band 9, and band 7, respectively. Although the observed points are scarce, the population model suggests more numerous sources of the same flux density at 850 μm , while those detected at 450 μm window are fewer but more luminous. In the context of strong (galaxy–galaxy) lensing, this implies better chances of suitable strong lensing alignments at lower frequency bands. This, beside the results presented in section 4 makes ALMA band 7 and 8 observations preferred over those of band 9 in the for the purpose of this work.

3.2 Lensing simulations

To simulate the effects of dark halo substructure on macrolensed SMGs, we use a numerical scheme similar to that developed by Metcalf & Madau (2001), and the illustration in figure 2. An extended source is assumed to be multiply-imaged by a foreground galaxy, and the lens equation is used to determine the lens plane positions of the corresponding macroimages. A lens perturber (substructure) is then placed along the line of sight to one of the macroimages. The deflection angles (with contributions both from the subhalo and the macrolens) are computed for every pixel within this region and converted into a numerical surface brightness map of the macroimage. These maps are initially generated with a very fine pixel scale, but are then run through CASA to create the expected visibilities achieved with ALMA in the most extended configuration. This extended configuration has a maximum baseline ≈ 16 km and provides an angular resolution between 7 – 10 mas depending on the observational frequency band (band 7: 275 – 370 GHz, band 8: 385 – 500 GHz, and band 9: 602 – 720 GHz).

Sizes of SMGs are between 4–8 kpc (Swinbank et al. 2008). We model the dust continuum emission with a single Gaussian component with FWHM ≈ 0.5 – 1.0 arcsec and an unlensed flux density of 5 mJy at $z = 2.0$. Additional surface brightness structure in the galaxy due to the distribution of star forming regions will increase the lensing effect. Given the relatively strong continuum emission from these sources the required integration time with the full array does not exceed 2 hours.

The lens model has 19 independent parameters for the source (7), main lens(7), and the lens perturber, aka. subhalo (5) as listed:

Source : Position relative to the center of the observed emission ($\Delta\alpha_s$ and $\Delta\delta_s$), the intrinsic flux density (F_s), the half-light radius (r_s), ellipticity (ϵ_s), position angle (ϕ_s), and the redshift (z_s).

Main lens The main lens is assumed to be a singular isothermal sphere, a commonly-used model for an early–

type galaxies (e.g. Rusin, Kochanek, & Keeton (2003); Keeton (2003); & Koopmans et al. (2006)). The mass of the main lens is set by the corresponding line-of-sight velocity dispersion (σ_l), position ($\Delta\alpha_l$ and $\Delta\delta_l$), ellipticity and position angle (ϵ_l , and ϕ_l), the core radius (r_l^c), and the redshift (z_l).

Lens perturber The inner density profile of the lens perturber, i.e. dark substructure, is parameterized in the lens model with the combination of a concentration parameter (c_{sub}), and the Einasto index (α_{Ein}). The two are additional parameters to any assumed lens. All perturbers are assumed spherically symmetric, i.e. ellipticity and position angle (ϵ_{sub} , and ϕ_{sub}) equal zero, and in the lens plane, i.e. $z_{\text{sub}} = z_l$. Even though no multi-plane lens modeling has been performed, the effect of line-of-sight contamination is briefly discussed in the discussion section (section 5).

Simulations presented in this paper are all based on a lens–source configuration that in the absence of substructure would give typical magnifications $\mu_1 \approx 10$ for at least one of the macroimages. This is consistent with typical magnification for observed SMGs (e.g. Wardlow et al. 2013). For each system, a lens configuration with $\mu \approx 10$ is chosen to ensure a macrolens magnification that is not unrealistically high. The substructure is placed to be projected in a radius of ~ 1 mas away from the image in the system with a magnification ~ 10 .

An overview of the model surface brightnesses are illustrated in the first two rows in figure 3. The contour lines on all subframes show the main lens model (without substructure) down to 10% of the maximum flux density and the color map on each frame indicates the effect of a substructure (with different inner density profile in the different subframes) on the surface brightness distribution of the lensed source. The following rows are CASA simulations imaged using *natural* and *uniform* weighting, respectively. By comparing the corresponding subfigures in each set one can spot the differences in lensing residuals due to various weighting schemes. One relevant feature seen already in the lensing models is the clear presence of a small-scale perturbation at the position of the substructure when the substructure is in the form of compact halos (SIS and pseudo-Jaffe). On the other hand, the Einasto ($\alpha_{\text{Ein}} = 0.05$) substructure shows the most significant large-scale perturbation among all other substructures, both in the lensing model and in the *normally*-weighted images, but much less significantly on the images made using uniform weighting scheme.

The color map is normalized by the peak flux density in the smooth lens model, and measures the difference in flux density of the smooth lens and the perturbed lens system. The flux residuals in ranges of $f_{\text{res}} \leq -0.1$ and $f_{\text{res}} \geq 0.1$, marking 10% of the peak are marked as significant. While most of the effects are concentrated around peaks of the macroimage, in stronger cases, the large scale differences are present at detectable levels. In case of compact lens perturbers, SIS and pseudo-Jaffe, clearly detectable small-scale effects are also present (strong blue spots on the upper right macroimage). In principle, this small-scale effect is present in all lensing case, but remains below the resolution limit for others.

3.3 Visibility modeling

In radio interferometry, the direct measured sky values are complex visibilities measured at various (u,v) distances. Each visibility point carries information about flux from all over the sky. As a result of the Fourier transformation, narrow features on the (u,v) plane transform into wide features on the image plane and vice-versa. Therefore, surface brightness maps (images) made of interferometry data are subject to various assumptions in the deconvolution step. The resulting images of the same visibility set can differ notably in featured structures. These differences depend on the prior knowledge of the user about the source, and the chosen weighting scheme. In other words, pixel-to-pixel errors on the image plane are correlated and affected by the choice of grid cells in the imaging process. Therefore, direct visibility modeling is favored over surface brightness map model comparison. In simple cases where the source could be reduced into simple analytical components, e.g. a point source, Gaussian profile, uniform disk, circular ring, etc., or a combination of them, the best fit visibility model could be found by surveying the parameter space of each component. If the flux density distribution of the source in the image plane is more complicated, however, initially a flux density distribution in the image plane is made and then the calculated visibilities of that is compared to observed values. This method requires calculating the visibilities of all investigated points in the parameter space, and fitting measured visibilities to those of the models, and therefore is more computationally involved than image plane modeling.

To account for lensing effects on both large and small angular scales, the commonly-used *natural* and *uniform* weighting schemes are used simultaneously to fit the visibilities. Even by changing the weighting scheme, in order to do a pixel-to-pixel comparison, the (u,v) plane cell size needs to remain unchanged. For fulfilling the criterion of Nyquist sampling, $\Delta x < \frac{1}{u_{\text{max}}}$, the minimum (u,v) grid sizes for band 7, 8, and 9 are ~ 0.006 , ~ 0.005 , and ~ 0.002 respectively. In all cases, an integration time of ≤ 6 s is adopted to avoid information loss in phases, given that the luminous ring is about an arcsecond away from the phase center.

(u,v) sampling tends to be denser near the origin of the (u,v) plane, giving a better signal to noise ratio for short-spacing measurements. Normal beam convolution corresponds to a sampling/weighting function in the (u,v) plane that is usually depending on the radial distance from the origin on the (u,v) plane. Therefore, giving all datapoints the same weight (as in the *natural* weighting scheme), leaves the relative contribution of data to the sampling function. With the emphasis on short-spacings, the thermal rms noise level of the resulting map gets minimized, as the synthesized beam gets broader. This means that the small-scale structure of the source gets washed out by beam convolution and is an undesirable effect for a composite source. The alternatives, for preserving most of the structure in the source, at the cost of sensitivity, is to either set a minimum (u,v) limit, or downweight the datasets close to the origin on the (u,v) plane. The other commonly-used weighting scheme, known as *uniform* weighting is simply designed to weight visibilities at various (u,v) distances inversely proportional to their abundance. The detail of weighting in this scheme

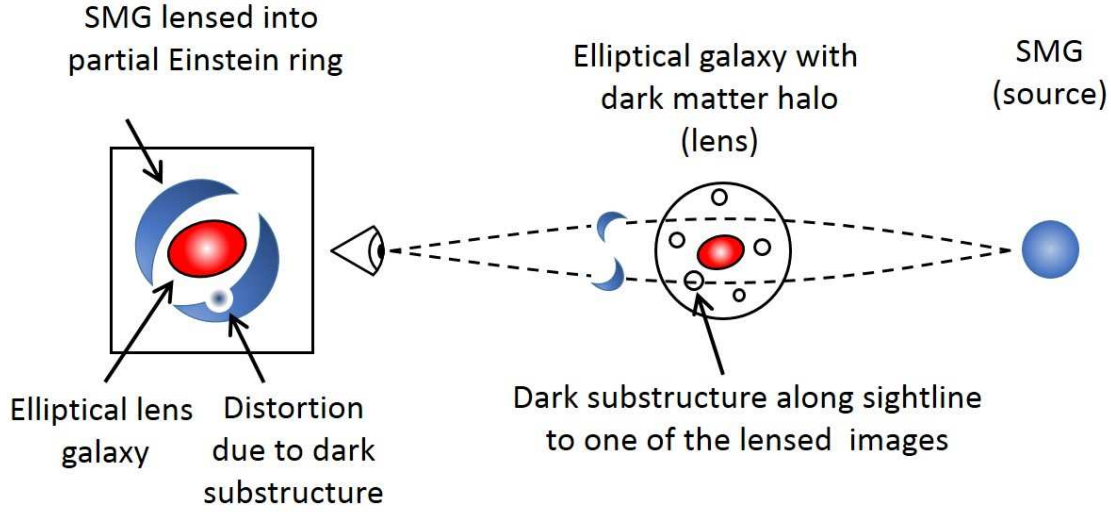


Figure 2. A schematic view of the spacial setup of the lens system. The source (sub-mm galaxy at $z \approx 2$) is multiply-imaged by the main lens. If the dark matter halo of the lens galaxy is populated with substructures, a subhalo along the line of sight towards one of the macroimages causes a secondary lensing effect. Given a strong-enough secondary lensing due to the subhalo, this distortion will only affect one of the macroimages, while the others remain intact, unlike any source structure that replicates in all macroimages.

depends on gridding of the (u, v) plane, where each data point is weighted according to

$$w_k = \frac{1}{N_s(k)}$$

where $N_s(k)$ is the number of data points within a symmetric region (cell) around the k^{th} data point on the (u, v) plane. The visibility plane is usually gridded into regularly-spaced square cells to ease the use of FFT algorithms. However, since data points are not regularly-spaced in the visibility plane, an interpolation operation is required.

The same weighting recipes as in CASA `clean` task are applied to simulated visibilities on the visibility plane. *Natural* weighting scheme which simply weights visibilities inversely proportional to the variance of their distribution. Therefore, short spacings in the (u, v) plane, with closer samplings, are weighted more than longer baselines which results in higher dynamic range in the modeled image at the cost of a coarser angular resolution. In other words, the dirty beam has larger FWHM, but less prominent side lobes. Using natural weighting scheme, therefore, places a conservative assumption on the angular resolutions discussed in this work. *Uniform* weighting scheme, on the other hand, increases the contribution from long-spacings and therefore results in a dirty beam with narrower FWHM, i.e. higher angular resolution, at the cost of increasing the resulting rms noise on the image plane. The narrower beam, therefore, can pick up small-scale structures that are smeared out by the beam in the naturally weighted image/visibility.

To find the effect of the projected subhalo, the smooth lens model is subtracted from the measurement set. The smooth lens model is assumed well-constrained. Therefore,

the remaining emission is due to the presence of a perturber in the lens. Any difference in the magnification map of an individual perturber with respect to another, will result in a different visibility residual making the two lens perturbers distinguishable.

Simulated ALMA visibilities are made using CASA software and the atmospheric thermal noise available in CASA through setting `thermalnoise="tsys-atm"` in `simobserve` is used as the noise estimate. Initially samples are drawn from the substructure parameter domain as inputs to the lensing software. The corresponding surface brightness then is sent into CASA to calculate complex visibilities. In each case a substructure of a random mass is projected within an area of 1 mas radius away from the image. The parameter space for the projected substructure covers the mass range of $M_{\text{sub}} = 3 \times 10^5 - 3 \times 10^{11} M_\odot$ and the Einasto index of $\alpha_{\text{Ein}} = 0.05 - 0.4$, as well as fixed instances of other density profiles; SIS, pseudo-Jaffe, NFW and truncated NFW. The best-fit model to the visibilities of each instance is then derived by minimizing the χ^2 of the visibilities of the simulated data set with the model visibility simultaneously for the two weighting scheme. Therefore, the best-fit model is chosen by minimizing

$$\chi^2 = \chi^2_{\text{uniform}} + \chi^2_{\text{natural}} \quad (1)$$

Where the χ^2 for each weighting scheme is calculated using

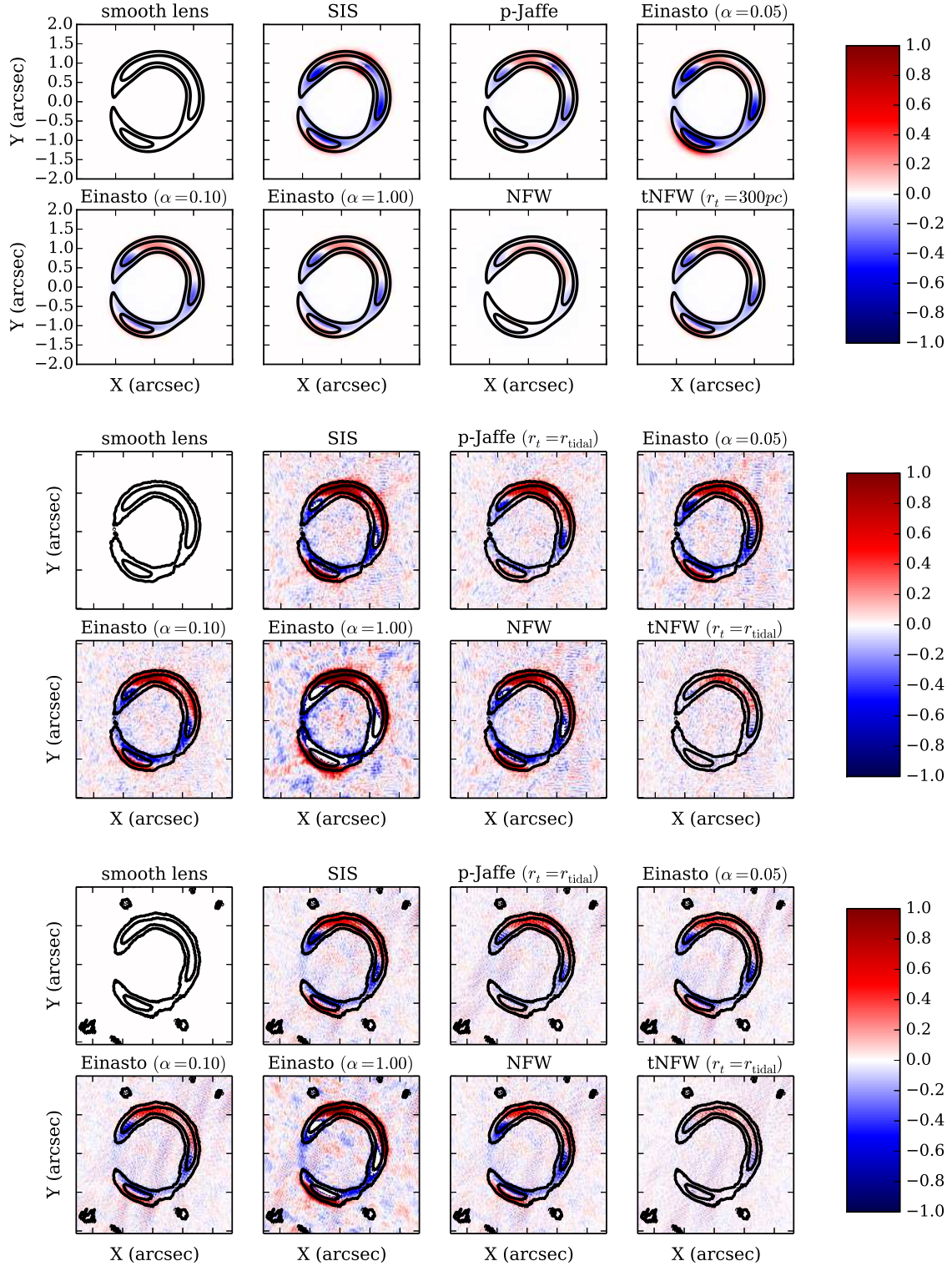


Figure 3. Upper left frame shows a sample smooth lens system in a flux density range down to 10% of the peak. The contour plots of the following frames show the smooth system as a frame of reference for comparison while the colored maps are indicative of the residual surface brightness as a result of the presence of halo substructure compared to the smooth lens model.

the function below.

$$\begin{aligned}\chi_{\text{Real}}^2 &= \sum_{u,v} \frac{[\text{Re}(V_{\text{smooth}}(u,v)) - \text{Re}(V_{\text{pert.}}(u,v))]^2}{\sigma_{\text{Real}}^2 + \sigma_{\text{Imag.}}^2} \\ \chi_{\text{Imag.}}^2 &= \sum_{u,v} \frac{[\text{Im}(V_{\text{smooth}}(u,v)) - \text{Im}(V_{\text{pert.}}(u,v))]^2}{\sigma_{\text{Real}}^2 + \sigma_{\text{Imag.}}^2} \\ \chi^2 &= \chi_{\text{Real}}^2 + \chi_{\text{Imag.}}^2.\end{aligned}\quad (2)$$

σ is the uncertainty in each visibility measurement.

Given the number of simulated data points for each set ($N_{\text{vis}} \sim 10^5 - 10^6$), the fitting process is expensive. Therefore, the explored grid is chosen to be as coarse as $\Delta\alpha_{\text{Ein}} = 0.1$ where the parameter for dark matter subhalos is weakly constrained by previous attempts and a strong degeneracy with mass is expected. The finer grid along the Einasto index is used for the next step as no significant best-fit model was found for instances with $\alpha_{\text{Ein}} > 0.4$. The final domain of investigation of the Einasto index is $\alpha_{\text{Ein}} : [0.05, 0.40]$ with a factor of 2 increase in the parameter resolution, i.e. $\Delta\alpha_{\text{Ein}} = 0.05$.

4 RESULTS

In order to constrain the mass and inner density profile of a lens perturber (subhalo), we first assume a fixed density profile for the subhalo and investigate the detection probabilities with respect to a smooth (unperturbed) lens model by varying the mass of the perturber. The results of this part, presented in figure 4, demonstrate the comparison of the compact density profiles (SIS and pseudo-Jaffe) with the standard subhalos (NFW and tNFW) as well as the difference between field ($R_{\text{trunc}} = R_{\text{virial}}$) halos and substructures ($R_{\text{trunc}} = R_{\text{tidal}}$) of the same mass.

4.1 Mass detection limit for fixed density profiles

Cuspy, two-parameter, density profiles such as SIS and pseudo-Jaffe are not well-supported by either observational fits to central density profiles of dwarf galaxies (see e.g. Flores & Primack 1994; Moore 1994; Strigari et al. 2006; Walker et al. 2009; Boylan-Kolchin, Bullock, & Kaplinghat 2011; Amorisco, Agnello, & Evans 2013; Collins et al. 2014), or simulated subhalos, which are, as discussed in section 2 best described by the Einasto profile with the shape parameter α_{Ein} as the fitting parameter. However, to follow the common practice (see e.g. Metcalf & Madau 2001; Metcalf 2002; Vegetti et al. 2010, 2012; Hezaveh et al. 2013) in gravitational lens modeling to fit SIS or pseudo-Jaffe to the lens substructure, we here report the mass detection limit given by our method for these density profiles as well. Figure 4 illustrates the detection significance of SIS perturbors of various M_{vir} (solid lines) compared to that of standard NFW substructures (dashed lines) as well as the tidally-truncated profiles of the two groups (pseudo-Jaffe and tNFW) with tidal radii calculated according to

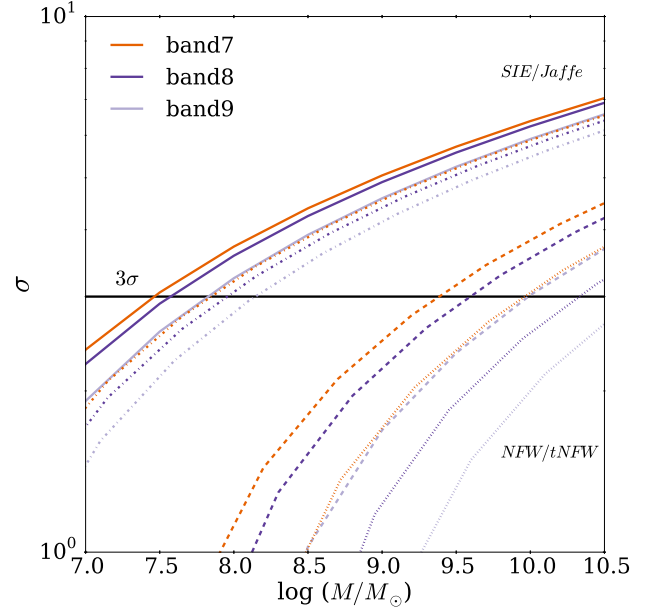


Figure 4. Comparison between the detection significance of SIS (solid lines), pseudo-Jaffe (dotted dashed lines), NFW (dashed lines), and tNFW perturbors (dotted lines) with respect to a smooth lens system. The x-axis is the detection threshold in terms of substructure mass and the y-axis depicts the significance of the statistical test preferring a model with a lens perturber of the corresponding mass to the system with the main lens only for ALMA band 7 (orange), band 8 (blue) and band 9 (purple). The results shown in this figure use the combination of *naturally*- and *uniformly*-weighted visibilities for each frequency band.

(Tormen, Diaferio, & Syer 1998) and in agreement with Springel et al. (2008) as below:

$$r_t = (M_{\text{sub}} / ([2 - \frac{d \ln M}{d \ln r}] M(< r)))^{1/3} r \quad (3)$$

where $M(< r)$ is the host halo mass within radius r .

The illustrated detection significance is derived from modeling simulated ALMA observations in shown bands, and illustrates the substructure mass limit at which the perturbed model gives a significantly better fit to the simulated visibilities than the smooth lens model. Setting the significance level at a 3σ detection of the substructure in the system, the smallest detectable SIS subhalo mass varies between $3 \times 10^7 M_{\odot}$ for band 7 to $5 \times 10^7 M_{\odot}$ for band 8, and $8 \times 10^7 M_{\odot}$ for band 9. The same mass detection result is shown for standard NFW substructures (dashed lines in Figure 4). The much higher mass detection limits (more than 2 subhalo mass decades) for NFW halos compared to that of SIS profiles, place the detected NFW subhalos barely in the mass range relevant for galaxy subhalos, i.e. $M_{\text{vir}} \sim 10^5 - 10^{10} M_{\odot}$.

Subhalo profiles with shallower central density slopes, even when contain masses as high as $10^{11} M_{\odot}$, add only large-scale perturbation to the main lens, i.e. astrometric shifts. Lensing effects of these subhalos therefore are more pronounced in *naturally*-weighted images. In other words, what

is needed is mostly increased sensitivity of observational data, rather than angular resolution. The local (pixel-by-pixel comparison) surface brightness perturbation for these halos (when $M \leq 10^{10} M_\odot$) does not exceed more than 1 in 100 compared to the smooth model. Even though the accumulated surface brightness perturbation between a smooth and a perturbed model reaches 0.1 of the original, it remains degenerate with the external shear. Therefore, these density profiles are only reconstructible when the external shear of the lens system is known.

In the absence of any detectable local perturbation made by subhalo profiles, and consistent with the analysis above, the original NFW halos (gNFW) are more efficient in producing astrometric shifts compared to the smooth lens model than the more physically-sound tidally-truncated subhalos (tNFW) as the latter lacks the extended tail in the density profile of former halos which is the key to the astrometric shifts.

When it comes to the more compact halos (SIS and pseudo-jaffe), the flux perturbation is more concentrated on small-scale effects; making the detectability more dependable on the angular resolution of the observational data rather than the sensitivity. If the subhalo happens to be projected close to one of the point lens images, sensitivity limit plays no role in the detectability of the subhalo. At the same time, because of the dominance of the local effects, the detectability limits depend more on the exact position of the subhalo with respect to the macroimage, as well as the local flux gradient of the image. Therefore, in the absence of other highly-magnified macroimages, the subhalo flux perturbation becomes indistinguishable from the potential structure of the source. In comparing the detectability limits for the SIS and the pseudo-jaffe profiles, the same analysis as in the case of original vs. tidally-truncated NFW works, such that the SIS subhalo gives rise to more astrometric shift than a pseudo-jaffe profile of the same mass due to the more extended tail of the density profile. The local effects of the two density profiles are, however, identical and because the detectability mass limits are lower for these halos, the astrometric shifts made by SIS halos are below the sensitivity limit of the [simulated] observations.

4.2 Mass–concentration degeneracy

The second part of our study concerns breaking the degeneracy between the mass and the concentration parameter of the perturber. In this part, a parameter space covering a range of subhalo masses between $10^5 M_\odot$ and $10^{11} M_\odot$ and the shape parameter α_{Ein} is searched for the best-fit model to simulated data and we are comparing the detectability of 3-parameter substructures with different shape parameters α_{Ein} .

Since the detection mass limit of the NFW substructures is on the massive side for galactic subhalos when both the density profile of the subhalo and the virial mass are set as fitting parameters, in this section we are comparing lens systems with Einasto perturbors of same masses but various shape parameters with each other. In other words, the mere presence of a lens perturber in the system is assumed and the flux density perturbations due to the differences in the shape parameter of the Einasto perturber is sought. The line width in figure 5 shows the significance with which the

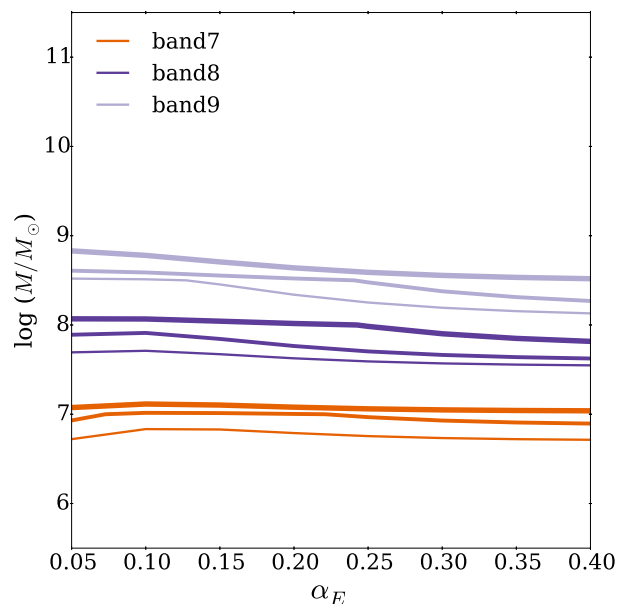


Figure 5. Comparing detection significance for Einasto profiles within a range of masses and Einasto indices. Different line colors are representative of the results given simulated observations with 3 different frequency bands of ALMA. Line widths correspond to the detection significance of the model with the given M_{Einasto} and α_{Ein} with respect to that of a smooth lens model.

Einasto profile is distinguishable from the SIS of the same mass. However, the lensing signal of the substructure is so weakly depending on the shape parameter that the mass and shape parameter of the Einasto profile remains degenerate within 5 decades of subhalo mass.

5 DISCUSSION

5.1 Substructure mass estimation

In this section we argue that comparison between the mass within the Einstein radius of the lens, derived directly from solving the lensing equation, and the physical mass of the lens, i.e. the tidal subhalo mass as discussed in N-body simulations, strongly depends on the assumptions about both the density profile and truncation radius of the halo.

Conventionally, simulated subhalo mass is presented as M_{tidal} , while the dwarf galaxy total/integrated mass is described within the central 300 pc as M_{300} . When discussing the detection limit of dark subhalos via gravitational lensing in the context of galaxy formation, it is crucial to make sure that the subhalo mass definitions assumed in lens models and N-body simulations are properly converted. This issue can be reduced to two different interpretations of the truncation radius of the halo, which becomes especially important when it comes to low-mass halos where detailed lensing signals are strongly affected by inner density slope and concentration (Zackrisson et al. 2008).

Einstein radius is defined as the radius within which, the mean surface mass density of the lens is equal to the

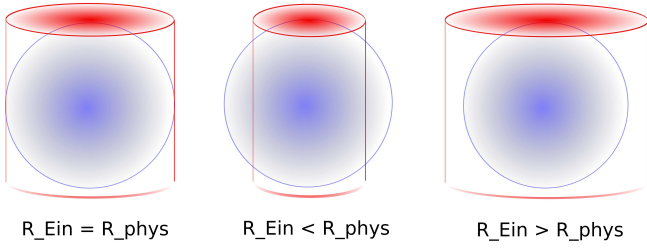


Figure 6. This simplified illustration shows how deriving the 3D mass of a spherical halo based on the mass measured in gravitational lensing (projected mass) could vary depending on the assumed physical radius of the halo.

critical surface mass density of the Universe at the redshift of the lens. Consequently, the Einstein mass is defined as the mass within the Einstein radius of the lens,

$$M_{\text{Ein}} = \Sigma_{\text{crit}} \pi R_{\text{Ein}}^2$$

In a strong lens system, the Einstein radius is a direct measure of the Einstein ring, arc or image separation. However, in lens systems such as the compound systems discussed in this paper, the direct measurement of the size of the Einstein radius using image separation is limited by the angular resolution. Besides, the projected mass contributing to the surface mass density of the lens corresponds to a combination of mass components including the main lens, the lens perturber (substructure) and an external shear accounting for the remaining mass components on the lens plane or along the line of sight.

Figure 6 illustrates how the measured M_{Ein} depends on the mass concentration within the lens as well as its physical truncation radius. In other words, the degeneracy between the Einstein mass of an observed lens and its physical 3D mass is only breakable if all fitting parameters of the model halo (M_{trunc} , R_{trunc} , M_{Ein} and R_{Ein}) are known. The illustration in figure 7 shows that when $R_{\text{Ein}} < R_{\text{phys}}$ (the case for virial halo of all the covered mass range), M_{Ein} derived from gravitational lensing only contains part of the physical mass content of the lens. Therefore, in order to derive the 3D mass content of the lens, one needs to assume a 3D density profile as well as a truncation radius, within which the actual mass content of the lens is meaningful.

While in cases where $R_{\text{Ein}} < R_{\text{trunc}}$ (the case for M_{300}), the mass distribution beyond R_{Ein} only affects the macro-resolution, i.e. the positions of multiple images which are beyond the resolution limit for low-mass subhalos.

Therefore, in order to derive the 3D mass of the lens the truncation radius R_{trunc} , total mass within R_{trunc} , and the mass distribution within the lens are to be fitted simultaneously.

The results presented in section 4 deal with three dimensional substructure 3D tidal masses $\sim 10^8 M_{\odot}$. The corresponding mass enclosed within the Einstein radius of each halo can be seen in figure 7 indicating that using the full ALMA with 10 km maximum baseline and about 10 times better spatial resolution than discussed in Hezaveh et al. (2013) enhances the mass sensitivity by more than an order of magnitude.

5.2 Current state of dark matter substructure as lens perturbers

The state of detecting dark substructure in strong lenses depends on the desired alignment, as well as the angular resolution. The trade-off between the source size and observational resolution results in the variety of instruments available for hunting dark subhalos.

Vegetti et al. (2010, 2012), using the Hubble space telescope and the Keck telescope, report the detection of two dark substructures of $M_{\text{Ein}} = 3.5 \times 10^9 M_{\odot}$ and $M_{\text{Ein}} = 1.9 \times 10^8 M_{\odot}$ in two strong lens systems SDSS J0946+1006 and JVAS B1938+666. They derive the gravitational potential of the lens and the *local* residual of the potential of the perturbed system compared to that of a smooth lens model, to constrain the projected mass of the perturber. According to the authors, the masses of substructures detected in these systems correspond to $M_{300}^{\text{p-Jaffe}} = 3.0 \times 10^8 M_{\odot}$ and $M_{300}^{\text{SIS}} = 3.3 \times 10^7 M_{\odot}$ for the more massive substructure and $M_{300}^{\text{p-Jaffe}} = 1.1 \times 10^8 M_{\odot}$ and $M_{300}^{\text{SIS}} = 6.1 \times 10^6 M_{\odot}$ for the low-mass one. However, as discussed in 5.1, in order to reproduce the deprojection one requires the physical truncation mass assumed for the deprojection as well as the Einstein mass and radius.

More recently Birrer, Amara, & Refregier (2015) presented a more generic method using Monte Carlo algorithms to solve simultaneously for substructures in the lens and source plane. They reconstruct the surface brightness by finding the global minimum of the χ^2 and achieve a lens substructure resolution of $\sim 10^8 M_{\odot}$ within the HST data.

A more similar method to the one presented in this paper is what suggested by Hezaveh et al. (2013) to detect dark subhalos in compound lens systems using ALMA. The method uses spatially resolved spectroscopy of high excitation (CO) lines tracing cores of star-forming regions in lens systems of different alignments when a dusty star forming galaxy at $z = 2$ is lensed by a foreground galaxy halo at $z = 0.5$ containing dark halo substructures using a total of 1 hr integration time with band 7 ALMA cycle 1 (maximum baseline = 1.1 km). The detection mass limit for single subhalos in their simulations is reported to be $M_{\text{Ein}} > 10^8 M_{\odot}$, translating to $M_{\text{vir}}^{\text{SIS}} = 3 \times 10^{10} M_{\odot}$ for a pseudo-Jaffe subhalo with, $\rho(r) \propto r^{-2}$ inner profile (Figure 7). It is worth mentioning that the standard dark matter density profiles are not considered in any of the works above making it difficult to derive the link between observations and theory.

Our method presented in section 3, improves this detection limit by about an order of magnitude. Looking at where the quality of fit for SIS and pseudo-Jaffe model comparison in the visibility plane cross the 3σ line in figure 4, shows our mass detection limit between $M_{\text{vir}} \approx 3 \times 10^7 M_{\odot}$ and $M_{\text{vir}} \approx 10^8 M_{\odot}$ (depending on the observational frequency band), translating to $M_{\text{Ein}} \approx 10^5 M_{\odot}$, although by assuming the full ALMA with an improved angular resolution by a factor of ~ 4 compared to that of cycle 1. The main difference of our method is using direct visibility measurements rather than the surface brightness, and combining two extreme weighting schemes. This combination allows for more sensitivity on arcsecond angular scales where more subtle surface brightness changes are due to the astrometric shift and more angular resolution around the macro images where

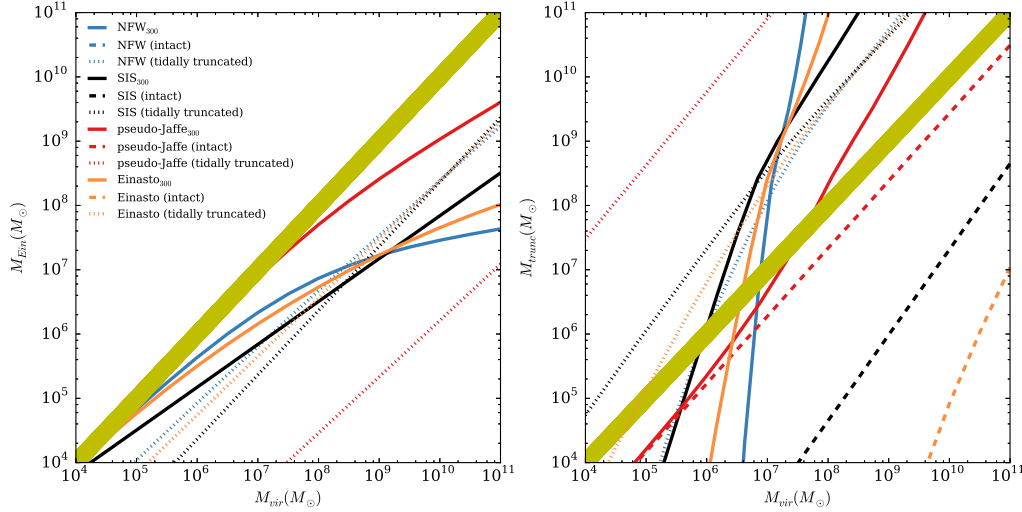


Figure 7. The importance of consistent mass conversion in comparing masses derived from lens models and N-body simulations and the effect of accounting for tidal stripping effects in outer regions of subhalos as opposed to field halos. **Left:** Translation between the virial mass and the truncated mass of halos at $z = 0.5$, for different inner density profiles. The thick yellow line has a slope of one and is therefore where all intact halos overlap. **Right:** Translation between the truncated mass and the mass within the Einstein radius of halos at $z = 0.5$, assuming $R_{\text{trunc}} = R_{\text{Ein}}$. Deviation of the mass within the half-light radius ($r_{\text{trunc}} = 300$ pc) from the virial mass is clearly visible for halos with $M_{\text{vir}} > \sim 10^6 M_{\odot}$ with NFW and Einasto inner density profiles while the difference tends to grow monotonously for halos with steeper logarithmic slopes, i.e. SIS and pseudo-Jaffe. One needs to keep in mind that halos with $M_{\text{vir}} \gtrsim 10^9 M_{\odot}$ can no longer be considered in the context of galactic substructure and consequently dwarf galaxies. The right panel shows how the mass measured within the Einstein radius deviates from the actual halo mass within the truncation radius (the virial radius for intact halos). The first immediate result is the group of dotted lines (indicating intact halos) in the lower right corner of the plot, implying large deviation of the deprojected mass within the Einstein radius from the subhalo mass within the virial radius. The red line, corresponding to pseudo-Jaffe profile shows the least deviation, while the NFW inner profile gives rise to a total Einstein mass of smaller than $10^4 M_{\odot}$ for subhalos with $M_{\text{vir}} \leq 10^{11} M_{\odot}$ consistent with expectations by comparing the central density slopes in figure 1.

there is a local magnification perturbation by the lens perturber.

5.3 Dark halos vs. luminous dwarf galaxies of the MW

Abundance matching models suggest the star formation efficiency of halos with $M_{200} < 10^{10} M_{\odot}$ to be smaller than 1% (Ferrero et al. 2012). This implies that only a small fraction of dark matter halos, of the same mass range as dwarf satellites, can inhabit luminous galaxies. On the other hand, the dark matter halo mass function at any given redshift is clearly predictable from the Λ CDM model (this substructure abundance, if normalized to the virial mass of the host, is independent of the host halo mass). However, observing dwarf galaxies becomes progressively more challenging as the redshift increases.

Another aspect of the comparison between the mass function of dark matter halos and the luminosity function of dwarf galaxies of the corresponding mass is the cut-off mass below which star formation inside a halo is quenched. Strigari et al. (2008) reports a common dynamical mass scale of $M_{300} \sim 10^7 M_{\odot}$ for a sample of SDSS dwarf satellites around the Milky Way covering a luminosity range of about four orders of magnitude. This can either imply a mass limit for dark matter halos and consequently dark matter particle mass, or for the efficiency of galaxy formation. The former issue could potentially be resolved by investigating the pres-

ence of dark matter substructures of the similar mass range, i.e. M_{Ein} between a few times $10^6 M_{\odot}$ to $\sim 10^9 M_{\odot}$ (see the right panel of figure 7).

Given a large enough sample of strong lens systems, both abundance and mass threshold of dark matter halos could be constrained. However, as discussed in section 5.1, the reliable mass translation plays a crucial role in using gravitational lensing techniques.

From a sample of 11 lensed galaxies from the SDSS at $z \approx 0.2$, 10 null detections and one luminous dwarf galaxy as the lens perturber, in combination with a previous dark subhalo detection, Vegetti et al. (2014) infer the value for projected substructure mass fraction within the host halo in the range of $0.006 < f_{\text{CDM}} < 0.007$, consistent with the value inferred from flux-ratio anomalies (Dalal & Kochanek 2002), at $z \approx 0.6$, but in tension with flux-ratio anomaly analysis of substructure mass between $4 \times 10^6 M_{\odot}$ and $4 \times 10^9 M_{\odot}$ by Xu et al. (2012) where they find $f_{\text{CDM}} \approx 0.0046$. While the corresponding slope of substructure mass function by Vegetti et al. (2014), i.e. $1.90 < \alpha < 2.93$, seems to be consistent with CDM predictions, the projected mass fraction is considerably higher than that predicted by the standard CDM model ($\alpha = 1.9$ and $< f_{\text{sub}} > \sim 0.2\%$). However, the tension could be an artifact of the mass truncation issue discussed above (see figure 6). Truncated pseudo Jaffe (and even NFW) halos in the substructure mass range lie in the interesting category of $R_{\text{Ein}} < R_{\text{phys}}$, i.e. a mass deprojection leading to $M_{\text{Ein}}/M_{\text{phys}} > 1$. Therefore, different assumptions

about the physical halo could alter the derived values of f_{sub} and α . In this case, the detected halos have lower physical masses than the mass derived from their Einstein radii, resulting in a steeper inferred mass function than the actual substructure mass function. While ignoring the deprojection issue, the tension either indicates the presence of a large population of subhalos at lower redshifts contaminating the line of sight towards the lens, or other types of dark overdensities in the halo, introducing a new challenge to the standard CDM model.

5.4 low-redshift line-of-sight contamination and external shear vs. central density profile

One often-neglected correction in strong lens modeling is if the lensed image is subject to more than a single lens at a single redshift. The probability of multi-plane lensing strongly depends, among other things, on the redshift of the source. Wambsganss, Bode, & Ostriker (2004) find that in 95% of the cluster lens systems with $z_s = 1$, the secondary lens effect is negligible. While this fraction decreases steeply to 68% for systems with $z_s = 3.8$. Whether the line-of-sight contamination effects occur within the strong or weak lensing regime, precise modeling of a multi-plane lens system is impossible, because of the large number of unknown parameters. A statistical approach is, however, possible to take within the context of the background cosmology. One aspect of this correction is assuming a cosmic shear effect in addition to the simple lens model. Schneider (2014) discusses the significance of lens perturbations in intermediate redshifts on cluster lens systems, in contrast to galaxy-scale lens systems where the alignment of multiple lens planes at different redshifts is improbable, although not impossible (e.g. Chae et al. 2001; Gavazzi et al. 2008). While within the region where strong lensing occurs, accounting for the main lens gives a good approximation of the lens model, other massive objects along, or close to, the line of sight add a lensing effect that could be as strong as a few percents of that of the strong lens region. However, galaxy-galaxy lens systems with more than one deflector along the line of sight are less probable than a cluster lens system of the same redshift combination.

Therefore, results of the small-scale strong lensing effects discussed in this paper are not likely to be due to line-of-sight contamination. In an unlikely case where the substructure lensing is due to a secondary lens at a redshift different than the primary lens, this gives an estimate of the systematic error on the subhalo mass fraction and mass function derived from a statistically-meaningful sample of such detections.

6 SUMMARY

We use simulations of strong galaxy-galaxy lensing systems with ALMA band 7, 8, and 9 in search of completely dark or high mass-to-light ratio subhalos through small-scale flux density perturbations in a single lensed image. We aim for lens perturbations of $M_{\text{sub}} = 10^5 - 10^{10} M_{\odot}$ in a Milky Way-sized halo at $z \sim 0.5$, the relevant mass range for dark subhalos. The lensed source, i.e. the sub-mm galaxy, is at $z \sim 2.0$, a typical redshift for lensed SMGs. The analysis (comparison between the smooth and perturbed lens model) is done on

simulated complex visibilities that are weighted differently so put emphasis on different angular scales of the flux density of the source.

We show that given a single perturber within the lens system is aligned with one of the images with $\mu \approx 10$, and the presence of at least one more magnified image in the system, 1) SIS perturbations more massive than $M_{\text{vir}} \approx 3 \times 10^7 M_{\odot}$, $M_{\text{vir}} \approx 5 \times 10^7 M_{\odot}$ and $M_{\text{vir}} \approx 8 \times 10^7 M_{\odot}$ will be detectable with 2hr observations using ALMA band 7, band 8, and band 9, respectively. More realistic CDM density profiles (NFW and Einasto), however, are only detectable when they are more massive than a few times $10^9 M_{\odot}$, placing them outside the interesting mass range of dark matter substructure. 2) While observations of this kind could in principle distinguish between a compact, singular isothermal, perturber and a halo with a shallower central density profile, as described by NFW or Einasto, this method cannot break the degeneracy between the mass and the shape parameter of the perturber.

ACKNOWLEDGEMENTS

E.Z. acknowledges funding from the Swedish Research Council (project number 2011-5349) and the Wenner-Gren foundations.

REFERENCES

- Amorisco N. C., Agnello A., Evans N. W., 2013, MNRAS, 429, L89
- Amorisco N. C., Evans N. W., 2012, MNRAS, 419, 184
- Bennett C. L., et al., 2013, ApJS, 208, 20
- Bertone G., Hooper D., Silk J., 2005, PhR, 405, 279
- Birrer S., Amara A., Refregier A., 2015, arXiv, arXiv:1504.07629
- Blain A. W., Smail I., Ivison R. J., Kneib J.-P., 1999, ASPC, 193, 425
- Boylan-Kolchin M., Bullock J. S., Kaplinghat M., 2012, MNRAS, 422, 1203
- Boylan-Kolchin M., Bullock J. S., Kaplinghat M., 2011, MNRAS, 415, L40
- Bringmann T., 2009, NJPh, 11, 105027
- Brooks A. M., Kuhlen M., Zolotov A., Hooper D., 2013, ApJ, 765, 22
- Bullock J. S., Dekel A., Kolatt T. S., Kravtsov A. V., Klypin A. A., Porciani C., Primack J. R., 2001, ApJ, 555, 240
- Chae K.-H., Turnshek D. A., Schulte-Ladbeck R. E., Rao S. M., Lupie O. L., 2001, ApJ, 561, 653
- Chiba M., 2002, ApJ, 565, 17
- Collins M. L. M., et al., 2014, ApJ, 783, 7
- Cornell J. M., Profumo S., Shepherd W., 2013, PhRvD, 88, 015027
- Cyr-Racine F.-Y., Moustakas L. A., Keeton C. R., Sigurdson K., Gilman D. A., 2015, arXiv, arXiv:1506.01724
- Dalal N., Kochanek C. S., 2002, ApJ, 572, 25
- de Blok W. J. G., 2010, AdAst, 2010, 789293
- de Blok W. J. G., McGaugh S. S., Bosma A., Rubin V. C., 2001, ApJ, 552, L23
- Del Popolo A., Lima J. A. S., Fabris J. C., Rodrigues D. C., 2014, JCAP, 4, 021
- Di Cintio A., Brook C. B., Macciò A. V., Stinson G. S., Knebe A., Dutton A. A., Wadsley J., 2014, MNRAS, 437, 415
- Dutton A. A., Macciò A. V., 2014, MNRAS, 441, 3359
- Ferrero I., Abadi M. G., Navarro J. F., Sales L. V., Gurovich S., 2012, MNRAS, 425, 2817
- Flores R. A., Primack J. R., 1994, ApJ, 427, L1

- Fry A. B., et al., 2015, MNRAS, 452, 1468
- Gao L., Navarro J. F., Frenk C. S., Jenkins A., Springel V., White S. D. M., 2012, MNRAS, 425, 2169
- Gao L., Navarro J. F., Cole S., Frenk C. S., White S. D. M., Springel V., Jenkins A., Neto A. F., 2008, MNRAS, 387, 536
- Garrison-Kimmel S., Horiuchi S., Abazajian K. N., Bullock J. S., Kaplinghat M., 2014, MNRAS, 444, 961
- Gavazzi R., Treu T., Koopmans L. V. E., Bolton A. S., Moustakas L. A., Burles S., Marshall P. J., 2008, ApJ, 677, 1046
- Hayashi E., White S. D. M., 2008, MNRAS, 388, 2
- Hezaveh Y. D., et al., 2013, ApJ, 767, 132
- Karim A., et al., 2013, MNRAS, 432, 2
- Keeton C. R., 2003, ApJ, 584, 664
- Klypin A., Kravtsov A. V., Valenzuela O., Prada F., 1999, ApJ, 522, 82
- Kochanek C. S., Dalal N., 2004, ApJ, 610, 39
- Koopmans L. V. E., Treu T., Bolton A. S., Burles S., Moustakas L. A., 2006, ApJ, 649, 599
- Kuzio de Naray R., 2008, ASPC, 396, 445
- Kuzio de Naray R., Spekkens K., 2011, ApJ, 741, L29
- Lovell M. R., et al., 2012, MNRAS, 420, 2318
- Macciò A. V., Dutton A. A., van den Bosch F. C., 2008, MNRAS, 391, 1940
- Maciejewski M., Vogelsberger M., White S. D. M., Springel V., 2011, MNRAS, 415, 2475
- Maxwell A. J., Wadsley J., Couchman H. M. P., 2015, ApJ, 806, 229
- Metcalf R. B., 2002, ApJ, 580, 696
- Metcalf R. B., Madau P., 2001, ApJ, 563, 9
- Metcalf R. B., Zhao H., 2002, ApJ, 567, L5
- Moore B., 1994, Natur, 370, 629
- Moore B., Ghigna S., Governato F., Lake G., Quinn T., Stadel J., Tozzi P., 1999, ApJ, 524, L19
- Navarro J. F., et al., 2004, MNRAS, 349, 1039
- Navarro J. F., Eke V. R., Frenk C. S., 1996, MNRAS, 283, L72
- Navarro J. F., Frenk C. S., White S. D. M., 1996, ApJ, 462, 563
- Navarro J. F., et al., 2010, MNRAS, 402, 21
- Oguri S., Inoue Y., Minowa M., 2010, NIMPA, 622, 588
- Oh S.-H., Brook C., Governato F., Brinks E., Mayer L., de Blok W. J. G., Brooks A., Walter F., 2011, AJ, 142, 24
- Peñarrubia J., Pontzen A., Walker M. G., Koposov S. E., 2012, ApJ, 759, L42
- Planck Collaboration, et al., 2014, A&A, 571, A17
- Riehm T., Zackrisson E., Möller O., Mörtzell E., Wiik K., 2008, JPhCS, 131, 012045
- Rusin D., Kochanek C. S., 2005, ApJ, 623, 666
- Rusin D., Kochanek C. S., Keeton C. R., 2003, ApJ, 595, 29
- Sawala T., et al., 2014, arXiv, arXiv:1406.6362
- Schaller M., et al., 2015, MNRAS, 451, 1247
- Schneider P., 2014, arXiv, arXiv:1409.0015
- Springel V., et al., 2008, MNRAS, 391, 1685
- Strigari L. E., Bullock J. S., Kaplinghat M., Kravtsov A. V., Gnedin O. Y., Abazajian K., Klypin A. A., 2006, ApJ, 652, 306
- Strigari L. E., Bullock J. S., Kaplinghat M., Simon J. D., Geha M., Willman B., Walker M. G., 2008, Natur, 454, 1096
- Swinbank A. M., et al., 2008, MNRAS, 391, 420
- Tormen G., Diaferio A., Syer D., 1998, MNRAS, 299, 728
- Vegetti S., Koopmans L. V. E., Auger M. W., Treu T., Bolton A. S., 2014, MNRAS, 442, 2017
- Vegetti S., Koopmans L. V. E., Bolton A., Treu T., Gavazzi R., 2010, MNRAS, 408, 1969
- Vegetti S., Lagattuta D. J., McKean J. P., Auger M. W., Fassnacht C. D., Koopmans L. V. E., 2012, Natur, 481, 341
- Vogelsberger M., Zavala J., Loeb A., 2012, MNRAS, 423, 3740
- Walker M. G., Mateo M., Olszewski E. W., Peñarrubia J., Wyn Evans N., Gilmore G., 2009, ApJ, 704, 1274
- Walker M. G., Peñarrubia J., 2011, ApJ, 742, 20
- Wambsganss J., Bode P., Ostriker J. P., 2004, ApJ, 606, L93
- Wang B., Justham S., Liu Z.-W., Zhang J.-J., Liu D.-D., Han Z., 2014, MNRAS, 445, 2340
- Wardlow J. L., et al., 2013, ApJ, 762, 59
- Wright E. L., et al., 1992, ApJ, 396, L13
- Xu D. D., Mao S., Cooper A. P., Gao L., Frenk C. S., Angulo R. E., Helly J., 2012, MNRAS, 421, 2553
- Xu D. D., et al., 2009, MNRAS, 398, 1235
- Xu D., Sluse, D., Gao, L., et al. 2015, MNRAS, 447, 3189
- Zackrisson E., Bergvall N., Marquart T., Östlin G., 2006, A&A, 452, 857
- Zackrisson E., Riehm T., Möller O., Wiik K., Nurmi P., 2008, ApJ, 684, 804
- Zackrisson E., et al., 2013, MNRAS, 431, 2172
- Zackrisson E., Riehm T., 2010, AdAst, 2010, 478910
- Zhu Q., Marinacci F., Maji M., Li Y., Springel V., Hernquist L., 2015, arXiv, arXiv:1506.05537

This paper has been typeset from a \LaTeX file prepared by the author.

